

POLITECNICO DI TORINO

MECHANICAL ENGINEERING



Master degree thesis

Design of lattice structures for de-icing systems integrated in aeronautic airfoils

Supervisors:

Prof. Giorgio De Pasquale

Prof. Paolo Maggiore

Carlo Giovanni Ferro

Author:

Alberto Tagliaferri

Summary

Nomenclature	I
Summary of figures	IV
Summary of tables	VIII
Abstract	IX
Introduction	X
1. The danger of ice on aircrafts	1
1.1. Anti-icing and de-icing systems	5
1.1.1. <i>Chemical solutions</i>	6
1.1.2. <i>Systems based on thermal energy</i>	7
1.1.3. <i>Mechanical systems</i>	8
1.1.4. <i>Systems based on ultrasonic waves</i>	10
1.2. The case of the wind turbines	11
1.3. Innovative design with AM integrated functional parts	15
2. Analytical model	18
2.1. Bcc-z cell type	19
2.2. Bcc cell type	24
2.3. Bcp-z cell type	26
2.4. Bcp cell type	28
2.5. Analytical model's validation	30

3. Specimens	33
3.1. Specimens design	33
3.2. Specimens fabrication	36
3.3. Dimensional validation	40
4. Experimental validation	43
4.1. Results	44
5. Numerical modeling	53
5.1. Linear numerical model	53
5.1.1. <i>Linear numerical vs experimental results</i>	55
5.2. Bi-linear numerical model	57
5.2.1. <i>Sensitivity's analysis</i>	58
5.2.2. <i>Calibration of the model</i>	64
5.2.3. <i>Bi-linear numerical vs experimental results</i>	67
6. Energetic analysis	76
Conclusions	79
References	81

Nomenclature

AM	Additive Manufacturing
SLM	Selective Laser Melting
FEM	Finite Elements Method
Bcc	Body-centered cubic
Bcc-z	Body-centered cubic with four vertical struts along the edges
Bcp	Body-centered parallelepipedal
Bcp-z	Body-centered parallelepipedal with four vertical struts along the edges
SMA	Shape Memory Alloy
SPEED	Sonic Pulse Electro-Expulsive De-icer
EIDI	Electro Impulsive De-Icing
EESS	Electro Expulsive Separation System
EMEDS	Electro-Mechanical Expulsion De-icing System
UGW	Ultrasonic Guided Waves
AV	Aste Verticali (bcc-z)
NA	Nessun' Asta (bcc)
CAD	Computer-Aided Design
wt-%	Weight percent
WEDM	Wire Electrical Discharge Machining
E	Young's modulus of the material
ν	Poisson ratio of the material
σ_y	Yield stress of the material
H	Strength coefficient of the material
\mathcal{E}	Total deformation energy of a specimen along z axis (load direction) until the first tension peak
σ	Apparent tension in the lattice along z axis (load direction)
ε	Deformation of the lattice along z axis (load direction)

ε_{peak}	Deformation of the lattice along z axis (load direction) corresponding to the first tension peak
V	External volume of the lattice
ℓ	Size of the cell along z axis (load direction)
d	Diameter of the strut
D	Calibrated diameter of the strut
u_l	Longitudinal displacement of a strut's extreme
u_t	Transversal displacement of a strut's extreme
u_z	Displacement of a strut's extreme along z axis
γ	Angle between a diagonal strut and z axis (load direction)
L	General length of a beam
A	Section of a beam
N	Normal reaction of a beam
Q	Shear reaction of a beam
\emptyset	Shear coefficient (Timoshenko)
I	Area moment of inertia of a beam
P	Hypothetical load along z axis on a node belonging to the upper plane of the lattice
S_o	Force reaction along z axis (load direction) coming from an oblique beam of a bcc cell
S_v	Force reaction along z axis (load direction) coming from a vertical beam of a bcc cell
S'_o	Stiffness contribution along z axis (load direction) coming from an oblique beam of a bcc cell
S'_v	Stiffness contribution along z axis (load direction) coming from a vertical beam of a bcc cell
V_o	Force reaction along z axis (load direction) coming from an oblique beam of a bcc- z cell
V_v	Force reaction along z axis (load direction) coming from a vertical beam of a bcc- z cell
V'_o	Stiffness contribution along z axis (load direction) coming from an oblique beam of a bcc- z cell
V'_v	Stiffness contribution along z axis (load direction) coming from a vertical beam of a bcc- z cell

k_i	Stiffness along z axis (load direction) of a loaded node belonging to the upper plane of the lattice with connectivity equal to " i "
N_i	Number of loaded nodes with connectivity equal to " i " belonging to the upper plane of the lattice
X	Size of the lattice along x axis (perpendicular to the load)
Y	Size of the lattice along y axis (perpendicular to the load)
Z	Size of the lattice along z axis (load direction)
n_x	Number of cells composing the lattice along x axis (perpendicular to the load)
n_y	Number of cells composing the lattice along y axis (perpendicular to the load)
$N_{layer/2}$	Number of semi-layers of cells composing the lattice along z axis (load direction)
$k_{layer/2}$	Stiffness of a semi-layer of cells composing the lattice along z axis (load direction)
k_{sample}	Stiffness of the lattice along z axis (load direction)
E_{sample}	Apparent Young's modulus of the lattice along z axis (load direction)
ℓ_{xz}	Size of a parallelepipedal cell along x axis and y axis (perpendicular to the load)
ℓ_z	Size of a parallelepipedal cell along z axis (load direction)

Summary of figures

Figure		Page
1.1	<i>Scheme of the Pitot tube</i>	2
1.2	<i>Pitot tube under the wing of a light aircraft</i>	2
1.3	<i>Precipitation icing</i>	3
1.4	<i>Comparison between glaze and rime ice</i>	4
1.5	<i>Frost over the wing of a light aircraft</i>	4
1.6	<i>Scheme of the hot air de-icing system</i>	7
1.7	<i>Scheme of the SPEED</i>	8
1.8	<i>Scheme of the EESS</i>	9
1.9	<i>Scheme of the pneumatic boot de-icing system</i>	9
1.10	<i>Scheme of the EMEDS</i>	10
1.11	<i>Scheme of the UGW</i>	10
1.12	<i>Ice on a wind turbine's wing</i>	12
1.13	<i>Anemometer</i>	12
1.14	<i>Manual de-icing of a wind turbine</i>	14
1.15	<i>Scheme of the structural components inside the wing leading edge</i>	15
1.16	<i>Scheme of the de-icing system patented by Politecnico di Torino</i>	16
1.17	<i>Draft of the sandwich panel</i>	16
1.18	<i>Draft of the sandwich panel (lateral view)</i>	17
2.1	<i>Loaded node with connectivity equal to 2 belonging to the upper plane of a lattice composed by bcc-z cells</i>	19
2.2	<i>Vertical beam's displacement and reaction</i>	20
2.3	<i>Oblique beam's displacement and reaction</i>	20
2.4	<i>Types of the loaded nodes belonging to the upper plane of a lattice composed by bcc-z cells</i>	23

2.5	<i>Loaded node with connectivity equal to 1 belonging to the upper plane of a lattice composed by bcc cells</i>	24
2.6	<i>Types of the loaded nodes belonging to the upper plane of a lattice composed by bcc cells</i>	25
2.7	<i>Loaded node with connectivity equal to 2 belonging to the upper plane of a lattice composed by bcp-z cells</i>	26
2.8	<i>Types of the loaded nodes belonging to the upper plane of a lattice composed by bcp-z cells</i>	28
2.9	<i>Loaded node with connectivity equal to 1 belonging to the upper plane of a lattice composed by bcp cells</i>	29
2.10	<i>Types of the loaded nodes belonging to the upper plane of a lattice composed by bcp cells</i>	30
2.11	<i>1D numerical model (undeformed and deformed structure) used to check the analytical model on a lattice composed by bcp-z cells</i>	31
3.1	<i>CAD geometries of a bcc cell (left) and a bcc-z cell (right)</i>	34
3.2	<i>CAD geometries of 4_1_AV</i>	35
3.3	<i>CAD geometries of 5_1.2_NA</i>	36
3.4	<i>EOS M270 Dual Mode Version</i>	36
3.5	<i>Scheme of the SLM process</i>	37
3.6	<i>Bcc-z specimens</i>	39
3.7	<i>Bcc specimens</i>	39
3.8	<i>Optical microscope Leica DMI 5000M</i>	41
3.9	<i>Compressed 5_1_NA sample with detailed views of the nodes</i>	41
4.1	<i>Zwick-Roell Z050</i>	43
4.2	<i>Setup principle for a compression test device</i>	44
4.3	<i>Experimental results for 4_1_AV samples</i>	45
4.4	<i>Experimental results for 4_1.2_AV samples</i>	45
4.5	<i>Experimental results for 5_1_AV samples</i>	46
4.6	<i>Experimental results for 5_1.2_AV samples</i>	46
4.7	<i>Experimental results for 4_1_NA samples</i>	47
4.8	<i>Experimental results for 4_1.2_ NA samples</i>	47
4.9	<i>Experimental results for 5_1_ NA samples</i>	48
4.10	<i>Experimental results for 5_1.2_ NA samples</i>	48
4.11	<i>Failure modality seen by two directions for a 4_1_AV sample</i>	49

4.12	<i>Failure modality for a 4_1.2_AV sample</i>	50
4.13	<i>Failure modality for three bcc samples (4_1_NA, 5_1_NA and 5_1.2_NA)</i>	50
5.1	<i>Numerical model of 4_1.2_AV samples with detailed view of the mesh</i>	54
5.2	<i>Numerical model of 4_1.2_NA samples with detailed view of the mesh</i>	55
5.3	<i>Relative errors in stiffness between linear numerical and experimental results</i>	56
5.4	<i>Tension exceeding the yield stress just under 4000 N of compressive load in the linear numerical model of 4_1.2_NA samples</i>	57
5.5	<i>Stress-strain curves of the material (perfectly plastic) obtained by varying E</i>	59
5.6	<i>Stress-strain curves of the material (perfectly plastic) obtained by varying σ_y</i>	59
5.7	<i>Differences between the results of the bi-linear numerical model with the nominal parameters and with the diameter of the struts increased or decreased by 10%</i>	60
5.8	<i>Differences between the results of the bi-linear numerical model with the nominal parameters and with the Young's modulus increased or decreased by 10%</i>	61
5.9	<i>Differences between the results of the bi-linear numerical model with the nominal parameters and with the yield stress increased or decreased by 10%</i>	61
5.10	<i>Experimental results in comparison to the bi-linear numerical response obtained with nominal and lowered parameters</i>	63
5.11	<i>Influence of the strength coefficient H</i>	64
5.12	<i>Calibrated geometry of the struts</i>	65
5.13	<i>Calibrated numerical model of 4_1.2_AV samples with detailed view of the mesh</i>	66
5.14	<i>Calibrated numerical model of 4_1.2_NA samples with detailed view of the mesh</i>	67
5.15	<i>Comparison between experimental and calibrated bi-linear numerical model's results of 4_1_AV samples</i>	68
5.16	<i>Comparison between experimental and calibrated bi-linear numerical model's results of 4_1.2_AV samples</i>	68

5.17	<i>Comparison between experimental and calibrated bi-linear numerical model's results of 5_1_AV samples</i>	69
5.18	<i>Comparison between experimental and calibrated bi-linear numerical model's results of 5_1.2_AV samples</i>	69
5.19	<i>Comparison between experimental and calibrated bi-linear numerical model's results of 4_1_NA samples</i>	70
5.20	<i>Comparison between experimental and calibrated bi-linear numerical model's results of 4_1.2_NA samples</i>	70
5.21	<i>Comparison between experimental and calibrated bi-linear numerical model's results of 5_1_NA samples</i>	71
5.22	<i>Comparison between experimental and calibrated bi-linear numerical model's results of 5_1.2_NA samples</i>	71
5.23	<i>Displacements [mm] and Von Mises tension [MPa] obtained with the calibrated bi-linear numerical model for 4_1_AV samples</i>	72
5.24	<i>Displacements [mm] and Von Mises tension [MPa] obtained with the calibrated bi-linear numerical model for 4_1.2_AV samples</i>	72
5.25	<i>Displacements [mm] and Von Mises tension [MPa] obtained with the calibrated bi-linear numerical model for 5_1_AV samples</i>	73
5.26	<i>Displacements [mm] and Von Mises tension [MPa] obtained with the calibrated bi-linear numerical model for 5_1.2_AV samples</i>	73
5.27	<i>Displacements [mm] and Von Mises tension [MPa] obtained with the calibrated bi-linear numerical model for 4_1_NA samples</i>	74
5.28	<i>Displacements [mm] and Von Mises tension [MPa] obtained with the calibrated bi-linear numerical model for 4_1.2_NA samples</i>	74
5.29	<i>Displacements [mm] and Von Mises tension [MPa] obtained with the calibrated bi-linear numerical model for 5_1_NA samples</i>	75
5.30	<i>Displacements [mm] and Von Mises tension [MPa] obtained with the calibrated bi-linear numerical model for 5_1.2_NA samples</i>	75
6.1	<i>Comparison between experimental and numerical deformation energy until the first tension peak in the load direction</i>	78

Summary of tables

Table		Page
1.1	<i>Areas subjected to ice formation with relative problems and anti-icing/de-icing system's type</i>	6
2.1	<i>Comparison between analytical and numerical stiffnesses</i>	32
3.1	<i>Specimens' geometrical and size nominal characteristics</i>	35
3.2	<i>Chemical, physical and mechanical properties of EOS Aluminum AlSi10Mg powder</i>	38
3.3	<i>Production parameters of the samples</i>	38
3.4	<i>Specimens' sizes</i>	40
3.5	<i>Comparison between real and nominal diameters</i>	42
4.1	<i>Experimental results</i>	52
5.1	<i>Mesh characteristics for the numerical model</i>	53
6.1	<i>Comparison between experimental and numerical deformation energies</i>	77

Abstract

The aeronautical sector needs to optimize the weight of its structures without losing their functions. Nowadays, with the expansion of the additive manufacturing technologies, it is possible to satisfy the most extreme requirements of the lightweight design. This is often done thanks to lattice structures.

In this thesis, a real application is described. It is a de-icing system for aircrafts constituted by a sandwich panel with a lattice core and patented by Politecnico di Torino [1].

This thesis is focused on the structural behavior of the reticular frame under a static compression load. A general analytical method, which neglects the edge effects and is based on beam's theory, is exposed. Its target is to evaluate quickly the stiffness by uniaxial compression of four types of lattice when the struts are slender enough, the number of cells is relatively high in the two spatial directions perpendicular to the load and as low as possible in the load direction.

A series of experimental tests is performed over some significant samples with two kinds of topology. A three-dimensional FEM analysis is carried out to fit experimental and numerical results in terms of stiffness and deformation energy.

Fatigue, thermal and impact analyses could be discussed in future studies. Moreover, new geometries and materials could be tested.

Introduction

The aim of this thesis is to establish a method to study the structural behavior of lattice structures loaded by compression. These are sometimes called biomimetic structures because of their great similarity with natural frames, such as those inside bones, corals and wood. They represent the bulk materials' structural optimization to which nature is arrived after millions of years of evolution. They find large application on aeronautical field, where the minimization of the weight is vital, thanks to the recent optimization of metal micro-fusion techniques. In fact, new additive manufacturing technologies allow the creation of non-stochastic foams, which were practicably unfeasible until a few years ago [2].

In this work, the first chapter describes anti-icing and de-icing methods currently used on aircrafts and wind turbines [3-11]. During the last years, a great attention is paid by recent regulations over these techniques because ice is still today the cause of many fatal crashes.

A new technology patented by Politecnico di Torino is presented too. It is simply a sandwich panel, whose core is a trabecular frame, directly integrated in the primary structure. The outer skin constitutes the aerodynamic profile of the aircraft's fixed wing, while the internal skin integrates the tubes for the hot air coming from the compressor [12-14]. Thanks to some slits, the hot air passes from the tubes to the lattice core, where it is free to circulate. The lattice's struts represent a preferential path for the heat, having a larger thermal conductivity in respect to air. This aspect increases greatly the efficiency

of the de-icing system. In fact, nowadays, technologies that use thermal energy decrease too much the performance of the engine, increasing the fuel consumption. The role of the core is not only thermal, but also structural: it must support the weight of the whole system and some occasional impacts (birds-strike). These requirements must be met respecting the guide lines of the lightweight design. For this reason, lattice frames are preferred to bulk materials (they give a better weight/stiffness ratio ensuring even higher absorbed deformation energy).

The whole system is produced in a unique piece by additive manufacturing, avoiding additional weight due to fixing systems (welding, rivets, joints and gluing) and the relative maintenance time and costs. The production technique used is SLM (Selective Laser Melting) which allows to obtain near-net-shaped components. The materials chosen are aluminum alloys or titanium alloys, since low density, high thermal conductivity, mechanical properties and corrosion resistance must be guaranteed.

Demonstrated the importance of the core, it becomes necessary to discover its optimal geometry for the afore-mentioned application (structurally and thermally).

In the second chapter a general analytical method, which neglects the edge effects and is based on beam's theory, is exposed. Its target is to evaluate quickly the stiffness by uniaxial compression of four types of lattice (bcc-z, bcc, bcp-z and bcp) when the struts are slender enough, the number of cells is relatively high in the two spatial directions perpendicular to the load and as low as possible in the load direction. This method has the advantage of being modular and parametrical: it is independent from the number of cells and gives the possibility to control easily the effect of each factor. It could be useful for any applications which respect its applicability's limits.

Previous thesis' works have performed some calculations and experimental tests over some significant samples [15, 16]. As described in the third chapter of this thesis, some specimens with parametrical characteristics have been projected and created by SLM technology. The material chosen is AlSi10Mg. Each of the eight samples is characterized by one of the two possible topologies (bcc and bcc-z), one of the two possible values of strut size (1 mm or 1.2 mm) and one of the two possible values of cell size (4 mm or 5 mm).

In the fourth chapter, the whole experimental procedure is presented. Even results reached by previous works [15, 16] are reported. The responses have been deeply analyzed to characterize all the considered specimens in terms of stiffness, apparent yield stress and apparent maximum stress.

In the fifth chapter, a three-dimensional numerical model obtained by a commercial FEM software (Optistruct by Altair) is elaborated to predict the experimental stiffness. Since with linear methods no satisfactory results have been obtained, a quasi-static non-linear approach and a calibration of the model have been necessary. The geometrical calibration has been performed thanks to a pre-existing microscopic analysis [14], which has revealed the real size of the struts. It is remarkable that the same calibration is repeatable for all the specimens. This calibrated numerical model should be efficient to simulate the whole component too.

In the sixth chapter the energetic analysis is carried out comparing experimental and numerical outcomes.

As future developments other studies could be interesting, such as the fatigue and the impact analysis. Even thermal tests are needed (currently other theses are involved in this topic). Moreover, new topologies and materials could be analyzed.

All these passages are necessary to design the entire system in its optimal version, before creating and testing it.

Chapter 1

The danger of ice on aircrafts

The ice is a very important danger for aircrafts, being cause of some famous catastrophic events, such as the crashes of the Air France Flight 447 in 2007 (228 victims) and of the Aero Caribbean Flight 883 in 2010 (68 victims). Often, this kind of tragedies is imputable to the deactivation of some sensors, such as the Pitot tube, a probe that indicates the velocity of the aircraft. In fact, this instrument can be partially or totally closed by the ice accretion, as well as by insects.

The Pitot tube is composed by two chambers linked to the external environment in two different ways. A chamber has its orifice's axis perpendicular to the air flow (it will have only the static pressure inside it); while the other chamber has its orifice's axis parallel to the air flow (it will have not only the static pressure inside it, but also the dynamic one). A pressure transducer measures the difference in pressure between the two chambers. The greater is this difference, the greater is the aircraft's speed. A sketch of this instrument is reported in Fig. 1.1, while Fig. 1.2 shows its application on aircrafts.

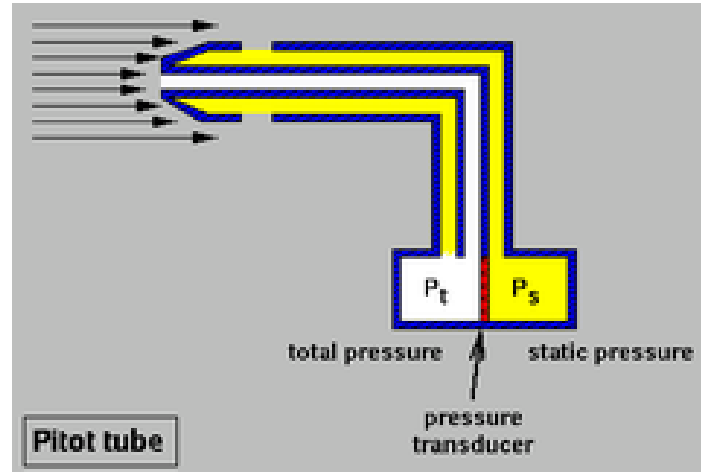


Figure 1.1. Scheme of the Pitot tube [17]



Figure 1.2. Pitot tube under the wing of a light aircraft [18]

Obviously, ice does not damage only probes and sensors, but can also alter the aerodynamic profile of the wings or decrease the visibility of the pilots nicking the glasses. It is vital to check the condition of the plane during the pre-flight very carefully.

Ice can nucleate during the flight, as well as when the airplane is on the ground. Its formation on a surface depends on many factors, such as weather conditions (temperature, relative humidity, presence of snow or rain) and material of the surface. Weather conditions can change very quickly, especially during the take-off, making the ice nucleation difficult to be predicted.

In general, there are three categories of ice: *precipitation icing*, *in-cloud icing* and *frost* [5]. Each type is characterized by physical properties, formation and accretion modalities.

Rain and snow can freeze on the surface that they hit causing the so-called precipitation icing (Fig. 1.3). This happens when the surface has a temperature below 0°C. The lower is the temperature when the contact occurs, the higher will be the adhesion strength between ice and surface. In the most extreme cases, even stalactites could form.



Figure 1.3. *Precipitation icing* [19]

When the range temperature is between -20°C and -35°C, supercooled droplets appear in clouds. If these, after hitting the surface, lose quickly their thermal energy and there is a low water content in air, rime forms. If the droplets were small, the rime is soft; while if the droplets are bigger and the air has a higher water content, the rime is hard. This last one is not so hard as the glaze, that forms if the thermal energy of the droplets is removed slowly, so that some droplets do not solidify, remaining as liquid water. Fig. 1.4 represents the physical appearance of these two kinds of ice.

If the trapped air's amount is very low, glaze is classified as "clear ice", difficult to be removed and detected because of its great transparency. This typology of ice could

form even at the ground. For example, when an aircraft, after flying in cold environments, lands with a big amount of residual fuel (its tanks have a stabilized temperature at values lower than 0°C , because of their large thermal capacity), the humidity present in the new warmer environment condensates on the surfaces of the tanks, causing the clear ice.

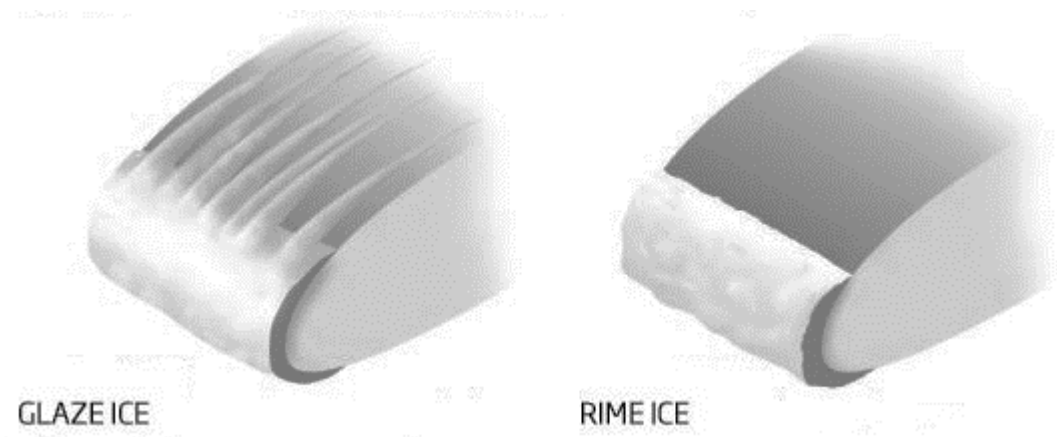


Figure 1.4. Comparison between glaze and rime ice [20]

Frost is characterized by a strong adhesion and is frequent during low winds. It is caused by the water vapor that solidifies directly on a cool surface. Fig. 1.5 shows an example of this type of ice.



Figure 1.5. Frost over the wing of a light aircraft [21]

1.1. Anti-icing and de-icing systems

Each area of an aircraft has a system to prevent the ice formation and to eliminate it. The mist on the glasses must be avoided too. There is a multitude of technologies to do this. The anti-icing system, which involves the use of water-repellent and antifreeze fluids, prevents the ice formation; while the de-icing system removes it.

Obviously, only the correct combination of all the systems allows to obtain the desired results without wastes in energy and time.

Table 1.1 summarizes the critical areas where ice could form with the relative problems and anti-icing/de-icing system's type.

Table 1.1. Areas subjected to ice formation with relative problems and anti-icing/de-icing system's type

Area where ice can form	Problem caused by the presence of ice	Anti-icing/de-icing system's type
Leading edges of the wings, slats, flaps and sensors	<ul style="list-style-type: none"> • Sensors' deactivation • Decreased drivability caused by aerodynamic profile's changes, unbalances, vibrations (added mass shifts the natural frequencies) • Motor blades' damages caused by detached ice's pieces • Increasing drag and so increasing fuel consumption 	<ul style="list-style-type: none"> • Hot air • Electrical resistances • Water-repellent and antifreeze fluids • Mechanical systems • Shape memory alloys • Ultrasonic waves systems • Graphite foils heated up electrically
Turbines' inlet	<ul style="list-style-type: none"> • Air mass flow rate's decrease • Motor blades' damages caused by detached ice's pieces 	<ul style="list-style-type: none"> • Hot air • Electrical resistances
Water drainage outlet	<ul style="list-style-type: none"> • Partial or total closure 	<ul style="list-style-type: none"> • Electrical resistances
Glasses	<ul style="list-style-type: none"> • Sight's limitation for the pilots 	<ul style="list-style-type: none"> • Water-repellent and antifreeze fluids • Electrical resistances • Transparent layers of conductive oxide inside the glasses' structure
General surfaces	<ul style="list-style-type: none"> • Decreased drivability caused by aerodynamic profile's changes, unbalances, vibrations (added mass shifts the natural frequencies) • Motor blades' damages caused by detached ice's pieces • Increasing drag and so increasing fuel consumption 	<ul style="list-style-type: none"> • Hot air • Electrical resistances • Water-repellent fluid and antifreeze fluids

1.1.1. Chemical solutions

Chemical solutions can be adopted as anti-icing systems. Antifreeze and water-repellent fluids based on ethylene glycol or propylene glycol are often spread on glasses, leading edges of the wings and general surfaces of the airplane. Ethylene and propylene glycols are harmful for the environment: they require a drainage system. Moreover, these fluids can not remain on the surfaces for a long period [4].

1.1.2. Systems based on thermal energy

Often the thermal energy is used in de-icing systems. This is obtained by hot air, taken from the pneumatic system (Fig. 1.6), or by joule effect thanks to electrical resistances. Some hangars use the infrared radiation to remove the ice. A special solution is adopted to remove the mist on the glasses: these have transparent layers of conductive oxide that produce heat once they are crossed by electricity [4].

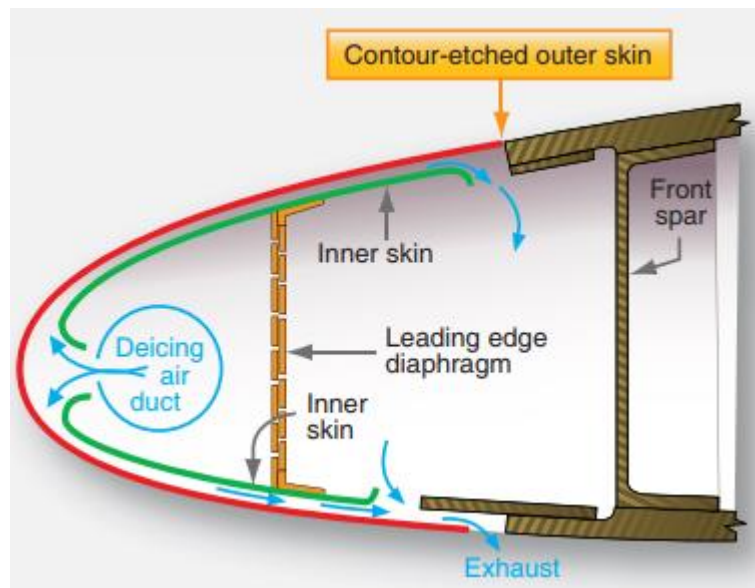


Figure 1.6. Scheme of the hot air de-icing system [3]

Sometimes particular materials are used. It is the case of the shape memory alloys (SMAs) and the graphite foils, very easy to be heated up and cooled down. In aeronautical applications, a SMA sheet, often a Ni-Ti alloy, is placed on the leading edge of the wing: it removes the formed ice by changing its own shape thanks to a martensitic phase transformation when a certain amount of thermal energy is delivered to the material [4].

1.1.3. Mechanical systems

There are also mechanical de-icing systems, whose category is very wide. The main technologies are SPEED, EIDI, EESS, pneumatic boot and EMEDS [10].

The Sonic Pulse Electro-Expulsive De-icer (SPEED), that is an evolution of the Electro-Impulsive De-Icing (EIDI), has some electromagnetic actuators (spiral coils) placed behind the leading edge. When these are crossed by electricity, an electromagnetic field is created, the spiral coils expand applying impulsive forces directly to the aircraft skin and the ice is removed. Fig. 1.7 represents a sketch of this system.

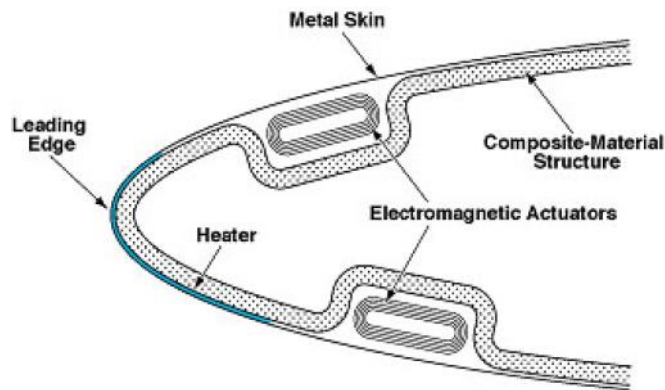


Figure 1.7. Scheme of the SPEED [10]

Another low-power system is depicted in Fig. 1.8. It is the Electro-Expulsive Separation System (EESS). A boot made of an elastomeric material is linked directly to airframe surfaces, perfectly adherent to them. Inside it there are two layers of conductors. When these are crossed by electricity, a magnetic field separate them of a few millimeters but instantaneously. So, the boot increases its size breaking the ice. This method requires a small amount of energy and is composed by an external component, easy to be removed for maintenance, that does not fatigue the aircraft structure. However, the maintenance should be quite frequent to avoid aerodynamic issues.

A more traditional system is the pneumatic boot, almost equal to EESS. In this case the elastomeric material is inflated by compressed air (Fig. 1.9). After the de-icing operation, vacuum is applied to make the boot perfectly adherent to the surfaces again.

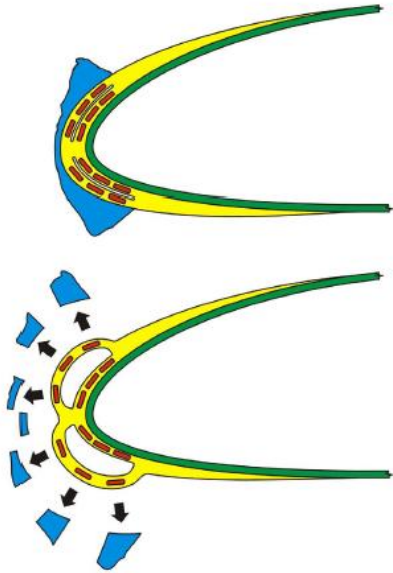


Figure 1.8. Scheme of the EESS [10]

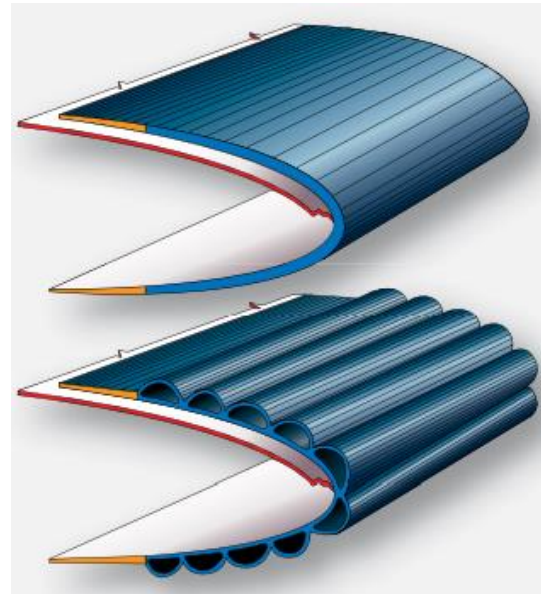


Figure 1.9. Scheme of the pneumatic boot de-icing system [3]

Electro-Mechanical Expulsion De-icing System (EMEDS) is very similar to SPEED. Some electrical impulses are delivered to the actuators to change their shape rapidly and harmonically. These actuators are linked to the erosion shield of the wing making it vibrate at a very high frequency. EMEDS is schematized in Fig. 1.10.

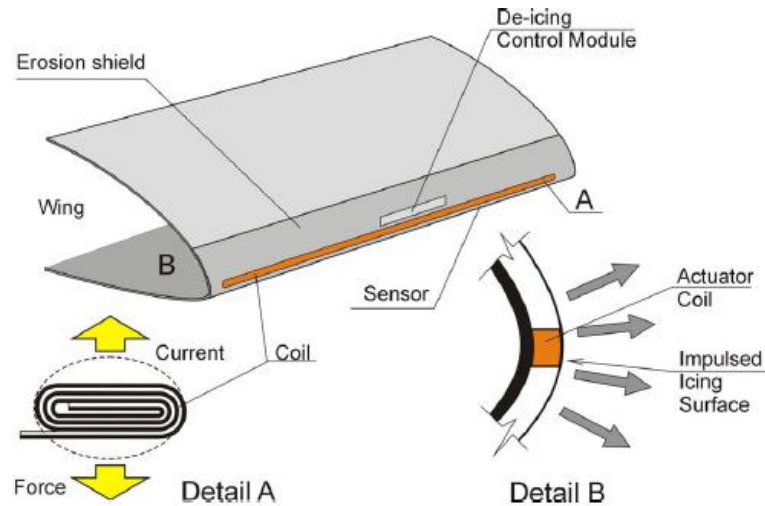


Figure 1.10. Scheme of the EMEDS [10]

Finally, manual scraping performed by the aeronautical maintenance engineers must be considered as a mechanical system.

1.1.4. Systems based on ultrasonic waves

Even technologies based on ultrasonic waves exist as de-icing systems. In Ultrasonic Guided Waves (UGW), piezoelectric excitation patches generate ultrasonic waves that propagate at low frequency inside the material causing vibrations (Fig. 1.11). This method gives high energy efficiency in respect to thermal systems and has low manufacturing and maintenance costs [10].

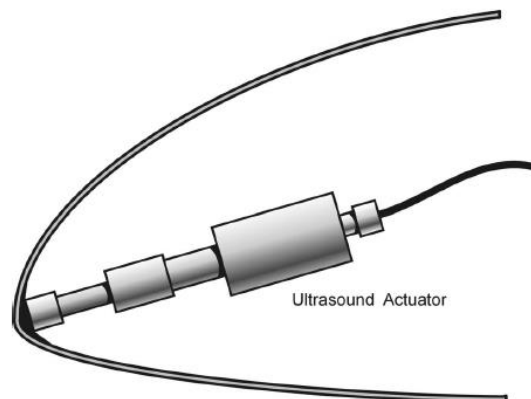


Figure 1.11. Scheme of the UGW [10]

1.2. The case of the wind turbines

As shown in Fig. 1.12, even the wind turbines suffer the problems coming from the ice formation, especially in the regions where, even occasionally, the temperatures fall under 0°C [5].

The power that they could produce is proportional to air density. So cold regions are very interesting for this application. Moreover, higher altitudes are appreciated for wind turbines' plants, since they ensure greater wind speeds. However, low temperatures and wind stimulate the ice nucleation and its accretion. Ice can decrease the performance of a wind turbine (it alters the aerodynamic profile of the blades), its durability (the increased mass caused by the ice accretion increases the loads and the unbalance causing vibrations) and the safety of people and buildings close to the plant. In extreme cases, even the full stop of the turbine can occur.

Unfortunately, ice is very difficult to be detected automatically, even because there are many different areas of the wind turbines that suffer this issue. Some of them could have a lot of ice, others not. Even the type of ice is various. In general rime occurs on the leading edge; while glaze far away from it, over the largest areas of the blade, since, in this case, water does not freeze instantaneously after the impact with the leading edge.

Ice accretion estimation can be done thanks to direct measurements, indirect measurements or numerical models (empirical or statistical). These last ones are based on temperature, cloud height, humidity, wind speed and direction, precipitation, topography, solar radiation, wing size, shape and material. Direct measurements detect changes of physical properties (mass, electrical or thermal conductivity, reflection). Indirect methods consider weather conditions, vibrations, noise or a reduction in power production. Among this kind of technology, the most promising is the double or triple anemometer (one or two are heated up). If the one that is not heated up decreases its

rotational speed, it means that it is covered by ice [4]. Fig. 1.13 represents a commercial example of a cup anemometer.



Figure 1.12. Ice on a wind turbine's wing [22]



Figure 1.13. Anemometer [23]

Sometimes, besides these instruments, also relative humidity or dew point detectors are used to perceive clouds and identify icing for temperatures below 0 °C. Video monitoring is an alternative way for the detecting of clouds, but it has yet to be automated and, during winter, visibility is often compromised. Noise sensors are not so appreciated because of signal's contaminations coming from the environment. The comparison between normal and actual power production is used just as a check: the differences may be explained by other factors than icing, such as air density variations, technical problems or increasing erosion of the blades' surfaces due to the impact with insects or dust [4].

Most of the anti-icing/ de-icing technologies applied to the aerospace industry can be transferred to wind turbines.

Anti-icing systems used for wind turbines are:

- special coating (silicon-epoxy based resins and polymers reinforced with nanometer-scale particles that increase also the erosion resistance and have limited costs);
- black paint (not effective during winter and in places where solar intensity is not sufficient);
- chemicals products (not very used because they can not stay on the blades' surface for a long time);
- clean air layer system.

This last technology consists in a flow of clean air, which can be heated up, coming from some small holes by the leading edge. It pushes away most of water droplets in the surrounding air, melting also the few ones which strike the surface.

While the de-icing systems are:

- flexible blades (not effective if the ice layer is thin, because it could be not so brittle to be cracked);
- electrical resistances;
- graphite foils;
- infrared radiation (it ensures low power-consumption but high investment cost);
- ultrasonic guided waves (UGW);
- hot air.

In the case of hot air technique, a closed circuit decreases the energy requirements (in an open cycle air needs to be heated up). Using waste heat from the turbine itself, efficiency can be improved. However, since blowers are placed by the root of each blade, its tip, that represents the most critical area, could not receive sufficient heat flux [4].

Sometimes a manual intervention is necessary not only to eliminate the ice, but also to clean the windmill blades from dust and insects. This is done thanks to helicopters that can spread hot pressurized water onto the blades (Fig. 1.14).



Figure 1.14. Manual de-icing of a wind turbine [24]

An innovative solution for wind turbines combines two technologies: low frequency vibrations and UGW [7]. A shaker makes the blades vibrate by torsion and bending modes at low frequencies close to the natural frequencies of the blades to induce the maximum amount of energy into them. This method is more effective in the areas near to the hub and less efficient at the leading edges. On the contrary, the more recent UGW is better for the leading edges, which are the most important surfaces for a wind turbine. Combining these two techniques, the whole blade is ensured to be de-iced.

To avoid damages in the structure, it is very important to set the frequency of the shakers correctly. In fact, a frequency too much close to the natural frequency of the blade could cause its failure. It is also vital to localize the shakers in the optimal positions, ensuring that they provide harmonic forces with the best direction. Even the piezoelectric patches must work with the ideal frequency and be positioned in such a

way to facilitate the waves' propagation. For these reasons, it becomes necessary a modal and a fatigue analysis of the entire assembly.

Another innovative technique, not yet fully developed, consists in a system which faces the blades into the sun to increase their temperature. Obviously, it is useful only in cold regions but with sufficient solar intensity [7].

1.3. Innovative design with AM integrated functional parts

The most critical part of an aircraft is the wing leading edge, since it must contain the anti-icing and de-icing systems and, at the same time, support aerodynamic loads and birds-strike. Both requirements (structural and thermal) must be met respecting the relative regulations and the lightweight design's requirements. Nowadays, the leading edge is made by different components (external skin, stringers, ribs, internal passageways and feeding tubes). Bolts, rivets, gluing and welding are employed to assemble all these components together, adding significant weight to the aircraft [12, 13]. In Fig. 1.15 a sketch is reported.

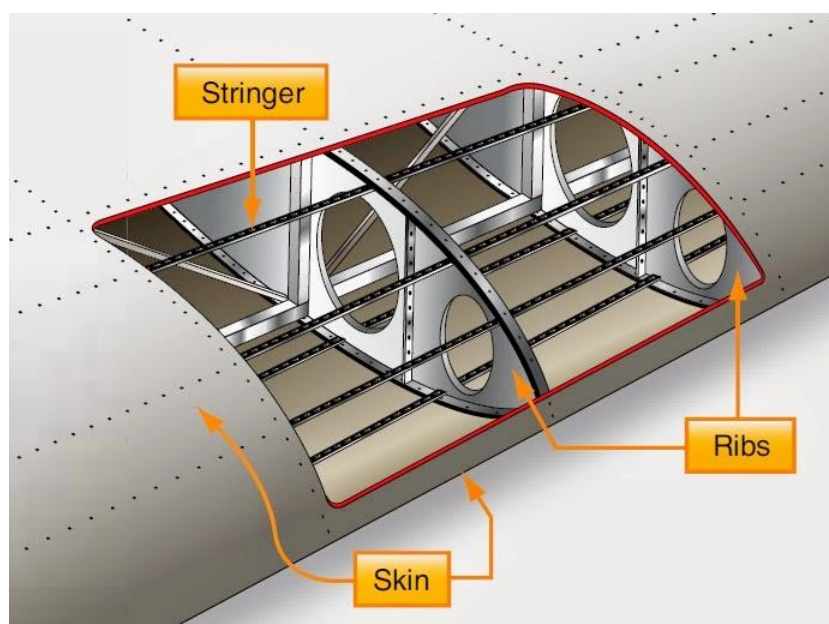


Figure 1.15. Scheme of the structural components inside the wing leading edge [3]

A novel de-icing system has been patented by Politecnico di Torino [1]. It uses something similar at a sandwich panel, directly integrated in the primary structure (Fig. 1.16).

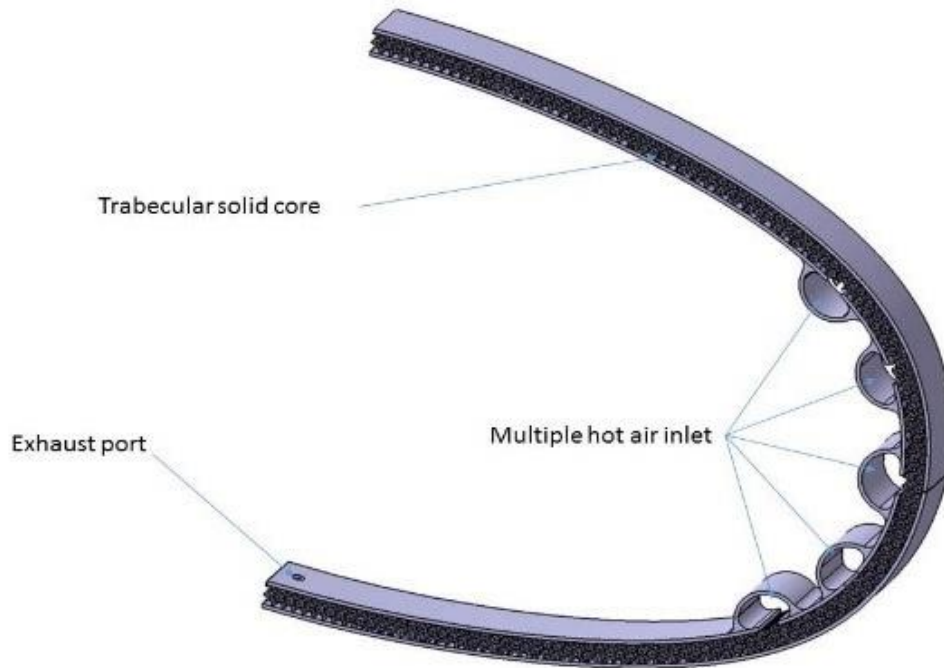


Figure 1.16. Scheme of the de-icing system patented by Politecnico di Torino [1]

As schematized in Figs. 1.17 and 1.18, it is composed by outer skin, inner skin and lattice core. The external skin is the aerodynamic surface, while the internal skin integrates the tubes for the hot air coming from the compressor. The hot air passes from the tubes to the lattice core through some slits and reaches the outer skin. The trabecular frame ensures a great heat transmission efficiency thanks to the high surface-volume ratio of its elements.

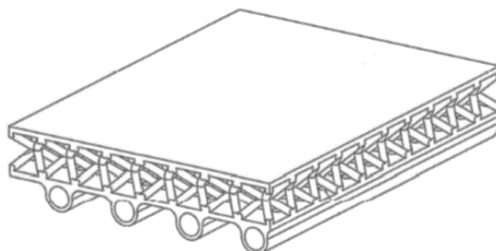


Figure 1.17. Draft of the sandwich panel [1]

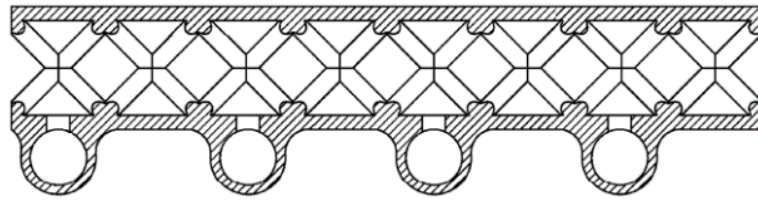


Figure 1.18. Draft of the sandwich panel (lateral view) [1]

The whole structure is manufactured in a single-piece by Selective Laser Melting (SLM). AM technologies are the only way to obtain a non-stochastic foam with controlled porosity avoiding any fixing system and, by consequence, drastically decreasing maintenance costs and times. Aluminum alloys, such as AlSiMg10, have low density, excellent mechanical properties, corrosion resistance and thermal conductivity. Titanium alloys can be used too.

Obviously, this new system could be applied also to wind turbines: the lowered weight of the wings allows to strongly decrease the inertial forces increasing the fatigue life of the entire structure.

Chapter 2

Analytical model

The aim of this part of the work is to obtain a general analytical method to evaluate the stiffness by uniaxial compression of a lattice structure, knowing its material, geometry and topology. The target is to strongly decrease the design time requested by a numerical approach. Lattices composed by bcc-z (body-centered cubic with added beams along z axis), bcc, bcp-z (body-centered parallelepipedal with added beams along z axis) and bcp cells will be analyzed.

It is possible to express the stiffness of a trabecular structure through its material's Young's modulus and geometrical parameters equalizing a kinematical load and the reaction to it [25]. The kinematical load, which is assumed to be small to preserve the linear behavior of the material, is applied on the upper plane of the lattice. The theory used is the beam's theory for not slender beams (shear effect is considered). Another applicability's limit is the number of cells along the two spatial directions perpendicular to the compressive load. This should be quite large (indicatively at least 100^2), because this analytical model neglects the edge's effects. In fact, the lattice is hypothesized to be nondeformable perpendicularly to the load. On the contrary, the number of cells which compose the lattice in the load direction, should be as low as possible (indicatively equal or less than 5). This limit is imposed by the constraints which are added along this direction by the analytical model in respect to the reality.

2.1 Bcc-z cell type

The target is to get the stiffness by uniaxial compression of a general lattice formed by bcc-z cells. To do this, the upper plane of the sample, i.e. the one containing the loaded nodes, must be considered. Each loaded node will answer with a certain reaction, depending on its connectivity. A node with connectivity equal to 2 (it is the case of the node located by one of the four vertexes of the top plane of the lattice) is connected to a vertical beam and to an oblique beam (Fig. 2.1). A strong hypothesis is the one relative to the constraints, that will make the analytical model to much stiff in comparison to the reality. In fact, this portion of cell is considered as fully constrained at its basis. Moreover, the only free degree of freedom is the vertical displacement of the upper node.

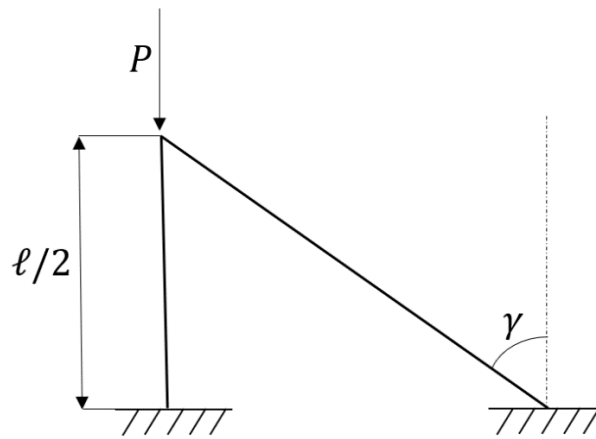


Figure 2.1. Loaded node with connectivity equal to 2 belonging to the upper plane of a lattice composed by bcc-z cells

Considering the two beams as energetically decoupled, i.e. as two independent cantilever beams, one works only by compression, the other by bending too. Figs. 2.2 and 2.3 show the displacements and the reactions of the decoupled beams.

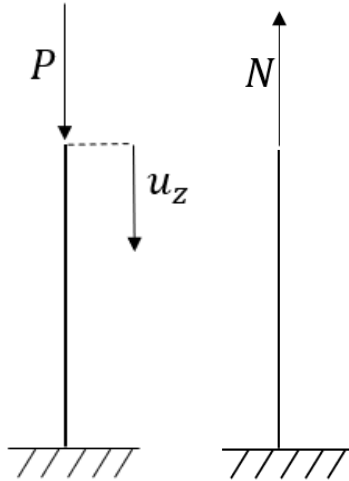


Figure 2.2. Vertical beam's displacement and reaction

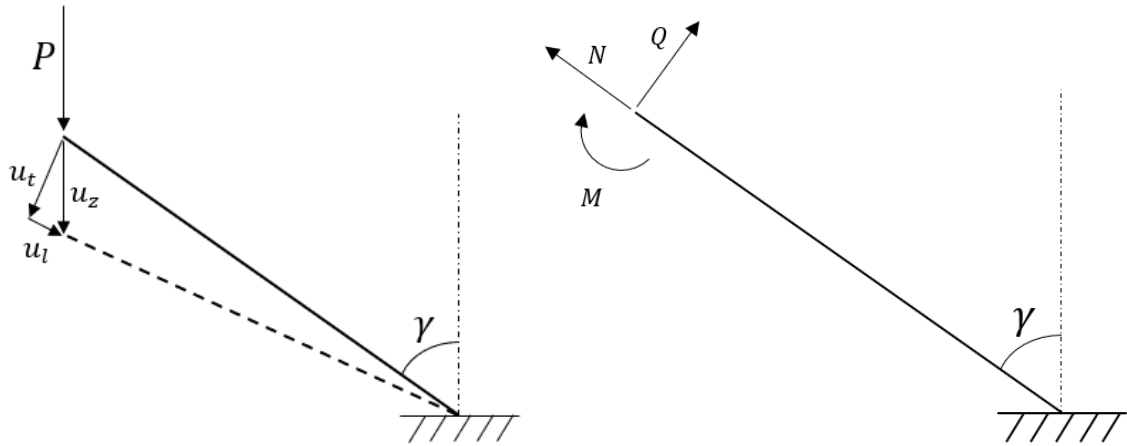


Figure 2.3. Oblique beam's displacement and reaction

Using trigonometry's rules, the vertical displacement u_z can be expressed as a function of the transversal one u_t or as a function of the longitudinal one u_l :

$$u_z = u_t / \sin\gamma \quad (2.1)$$

$$u_z = u_l / \cos\gamma \quad (2.2)$$

Where the angle γ , for a bcc-z cell, is equal to:

$$\gamma = \arctg(\sqrt{2}) = 54.74^\circ \quad (2.3)$$

In general, given L, A, E (respectively length, section of the beam and elastic modulus of the material), the normal reaction N of a cantilever beam is equal to:

$$N = \frac{EA}{L}u_t \quad (2.4)$$

While the shear reaction Q of a cantilever beam, considering the shear effect of Timoshenko \emptyset , is:

$$Q = \frac{12EI}{L^3(1 + \emptyset)}u_t \quad (2.5)$$

As written before, the vertical components of these two kinds of reaction must be equal to the external load P . Given ℓ as the dimension of the single cubic cell and substituting Eq. (2.1, 2.2) in Eq. (2.4, 2.5), it results:

$$\begin{aligned} P &= (N\cos\gamma + Q\sin\gamma) + N = \\ &= \frac{EA}{(\ell/2)}u_z\cos^3\gamma + \frac{12EI}{(\ell/2)^3(1 + \emptyset)}u_z\sin^2\gamma\cos^3\gamma + \frac{EA}{(\ell/2)}u_z = \\ &= \frac{2EA}{\ell}u_z\cos^3\gamma + \frac{96EI}{\ell^3(1 + \emptyset)}u_z\sin^2\gamma\cos^3\gamma + \frac{2EA}{\ell}u_z = \\ &= S_o + S_v \end{aligned} \quad (2.6)$$

Where:

$$S_o = \frac{2EA}{\ell}u_z\cos^3\gamma + \frac{96EI}{\ell^3(1 + \emptyset)}u_z\sin^2\gamma\cos^3\gamma \quad (2.7)$$

$$S_v = \frac{2EA}{\ell}u_z \quad (2.8)$$

S_o represents the reaction coming from the oblique beam; while S_v the one coming from the vertical beam.

The stiffness is the ratio between force and displacement. For a node with connectivity equal to 2, the stiffness k_2 is:

$$k_2 = \frac{P}{u_z} = \frac{2E}{\ell} \left[A(\cos^3\gamma + 1) + \frac{48I}{\ell^2(1 + \emptyset)}\sin^2\gamma\cos^3\gamma \right] = \frac{S_o + S_v}{u_z} = S'_o + S'_v \quad (2.9)$$

Where S'_o and S'_v are the stiffness contributions coming from the oblique beam and the vertical one respectively.

Now, to get the stiffness of the entire lattice, we will focus on all the nodes belonging to the upper plane of the lattice. In the case of bcc-z cells, they can have connectivity equal to 2, 3 or 5. To get the stiffnesses of the nodes with connectivity equal to 3 or 5, it is necessary to consider Eq. (2.9) and multiply S'_o by 2 or 4 respectively, because the oblique beams linked to these nodes are two or four (not only one, as for the nodes with connectivity equal to 2):

$$k_3 = 2S'_o + S'_v \quad (2.10)$$

$$k_5 = 4S'_o + S'_v \quad (2.11)$$

Referring to Fig. 2.4, it is possible to get the number of each type of node. Four nodes with connectivity equal to 2 are always present:

$$N_2 = 4 \quad (2.12)$$

The number of nodes with connectivity equal to 3 and 5 are respectively:

$$N_3 = 2\left(\frac{X}{\ell} - 1\right) + 2\left(\frac{Y}{\ell} - 1\right) = 2(n_x - 1 + n_y - 1) = 2(n_x + n_y - 2) \quad (2.13)$$

$$N_5 = \left(\frac{X}{\ell} - 1\right)\left(\frac{Y}{\ell} - 1\right) = (n_x - 1)(n_y - 1) \quad (2.14)$$

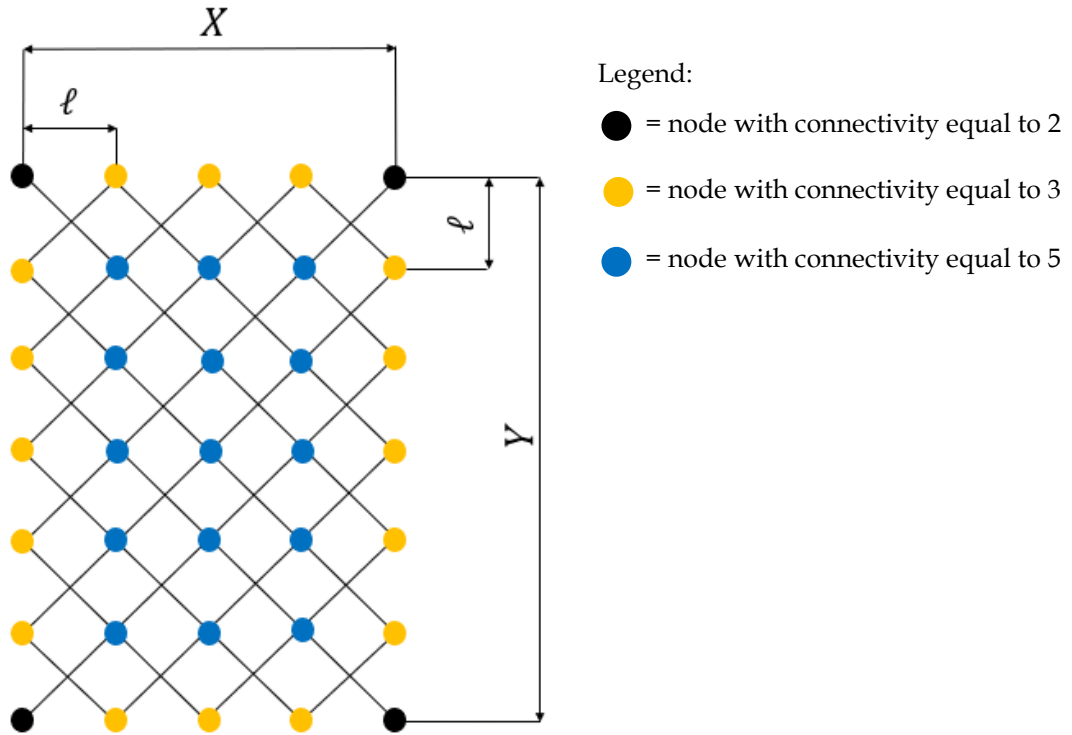


Figure 2.4. Types of the loaded nodes belonging to the upper plane of a lattice composed by bcc-z cells

Now, using the parallel springs formula, the stiffness of one half layer of cells $k_{layer/2}$ is equal to:

$$k_{layer/2} = N_2 k_2 + N_3 k_3 + N_5 k_5 \quad (2.15)$$

The stiffness of the whole specimen k_{sample} is computable using the series springs formula and knowing the number of semi-layers of cells $N_{layer/2}$ along the load direction:

$$k_{sample} = \frac{k_{layer/2}}{N_{layer/2}} \quad (2.16)$$

To calculate the apparent Young's modulus of the entire specimen E_{sample} , its three sizes in the space X , Y and Z must be known:

$$E_{sample} = \frac{k_{sample}Z}{XY} \quad (2.17)$$

2.2 Bcc cell type

For a lattice composed by bcc cells, the procedure is always the same. In this case there is not the reaction coming from the vertical beams ($S'_v = 0$). In fact, the loaded nodes can have connectivity equal to 1, 2 or 4. Fig. 2.5 reports the sketch of a node with connectivity equal to 1 belonging to the upper plane of the lattice.

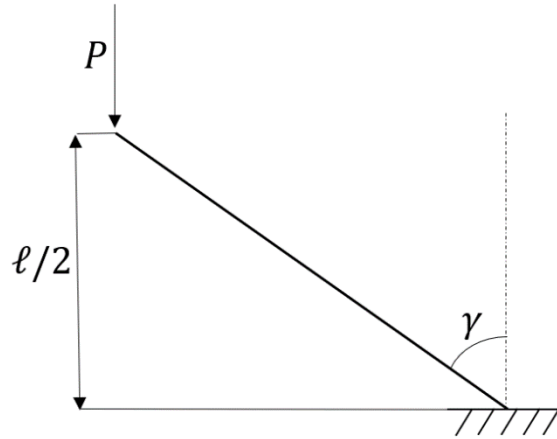


Figure 2.5. Loaded node with connectivity equal to 1 belonging to the upper plane of a lattice composed by bcc cells

Referring to Fig. 2.6, the number of the nodes with connectivity equal to 1, 2 and 4 can be calculated as follows:

$$N_1 = 4 \text{ (always)} \quad (2.18)$$

$$N_2 = 2\left(\frac{X}{\ell} - 1\right) + 2\left(\frac{Y}{\ell} - 1\right) = 2(n_x - 1 + n_y - 1) = 2(n_x + n_y - 2) \quad (2.19)$$

$$N_4 = \left(\frac{X}{\ell} - 1\right)\left(\frac{Y}{\ell} - 1\right) = (n_x - 1)(n_y - 1) \quad (2.20)$$

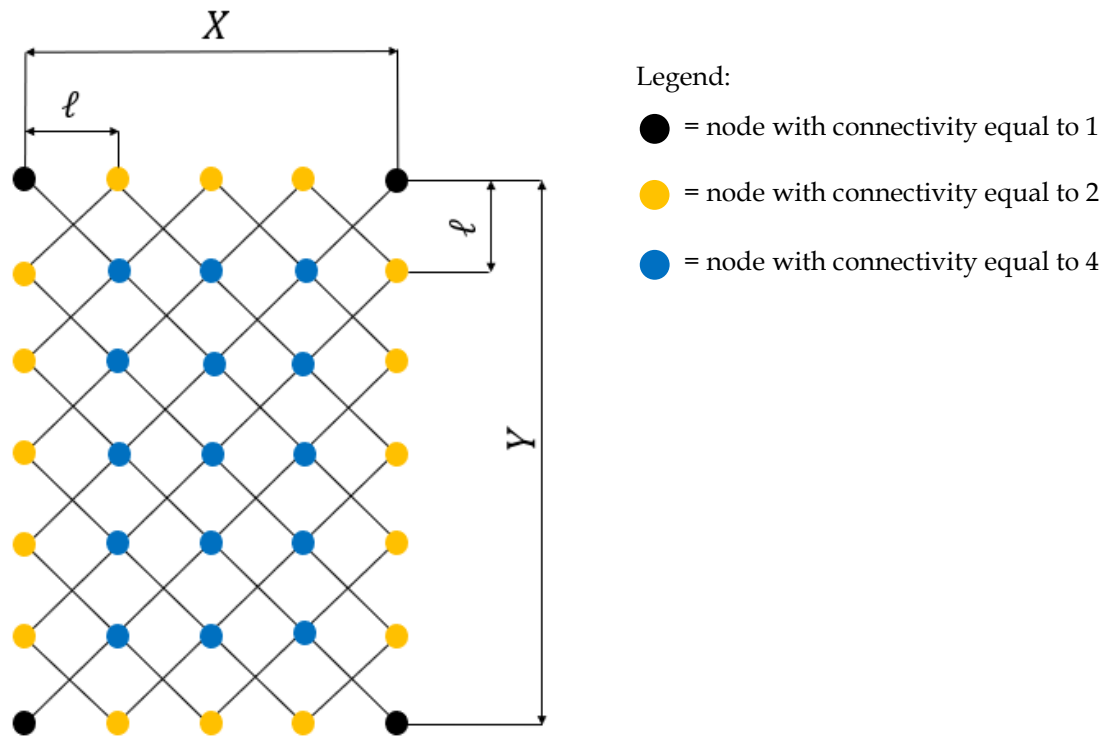


Figure 2.6. Types of the loaded nodes belonging to the upper plane of a lattice composed by bcc cells

The associated stiffnesses are:

$$k_1 = S'_0 \quad (2.21)$$

$$k_2 = 2S'_0 \quad (2.22)$$

$$k_4 = 4S'_0 \quad (2.23)$$

The stiffness of one half layer of cells $k_{layer/2}$ is equal to:

$$k_{layer/2} = N_1 k_1 + N_2 k_2 + N_4 k_4 \quad (2.24)$$

Using Eq. (2.16, 2.17), it is possible to get the stiffness and the apparent elastic modulus of the whole specimen.

2.3 Bcp-z cell type

The discussion is extended to a lattice with bcp-z cells. These will have height equal to ℓ_z and a squared basis with ℓ_{xy} as edge.

Now the sketch depicted in Fig. 2.7 represents the new geometry of a node with connectivity equal to 2.

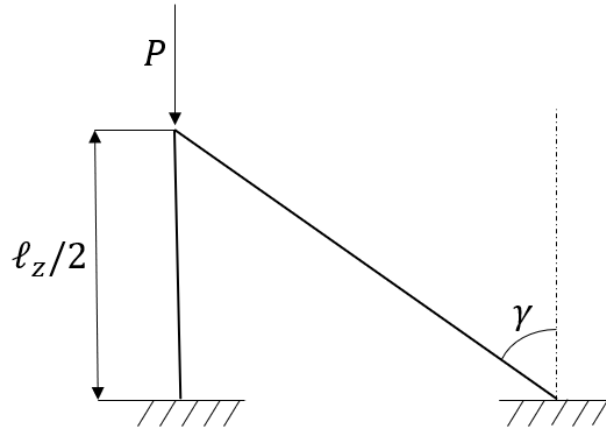


Figure 2.7. Loaded node with connectivity equal to 2 belonging to the upper plane of a lattice composed by bcp-z cells

The angle γ , for a bcp-z cell, depends on the cell's geometry and can be computed as:

$$\gamma = \arctg\left(\frac{\sqrt{2}\ell_{xz}}{\ell_z}\right) \quad (2.25)$$

Referring to Figs. 2.2 and 2.3, the Eq. (2.6) can be written as:

$$\begin{aligned} P &= (N\cos\gamma + Q\sin\gamma) + N = \\ &= \frac{EA}{(\ell_z/2)} u_z \cos^3\gamma + \frac{12EI}{(\ell_z/2)^3(1+\emptyset)} u_z \sin^2\gamma \cos^3\gamma + \frac{EA}{(\ell_z/2)} u_z = \\ &= V_o + V_v \end{aligned} \quad (2.26)$$

Where now:

$$V_o = \frac{EA}{(\ell_z/2)} u_z \cos^3 \gamma + \frac{12EI}{(\ell_z/2)^3 (1 + \phi)} u_z \sin^2 \gamma \cos^3 \gamma \quad (2.27)$$

$$V_v = \frac{EA}{(\ell_z/2)} u_z \quad (2.28)$$

By consequence, adapting Eq. (2.9):

$$k_2 = \frac{P}{u_z} = \frac{2E}{\ell_z} \left[A(\cos^3 \gamma + 1) + \frac{48I}{\ell_z^2 (1 + \phi)} \sin^2 \gamma \cos^3 \gamma \right] = \frac{V_o + V_v}{u_z} = V'_o + V'_v \quad (2.29)$$

The stiffnesses of the nodes with connectivity equal to 3 and 5 are:

$$k_3 = 2V'_o + V'_v \quad (2.30)$$

$$k_5 = 4V'_o + V'_v \quad (2.31)$$

Referring to Fig. 2.8, the number of nodes with connectivity equal to 2 is evaluable thanks to Eq. (2.12); while the number of the other nodes are calculable as:

$$N_3 = 2 \left(\frac{X}{\ell_{xy}} - 1 \right) + 2 \left(\frac{Y}{\ell_{xy}} - 1 \right) = 2(n_x - 1 + n_y - 1) = 2(n_x + n_y - 2) \quad (2.32)$$

$$N_5 = \left(\frac{A}{\ell_{xy}} - 1 \right) \left(\frac{B}{\ell_{xy}} - 1 \right) = (n_x - 1)(n_y - 1) \quad (2.33)$$

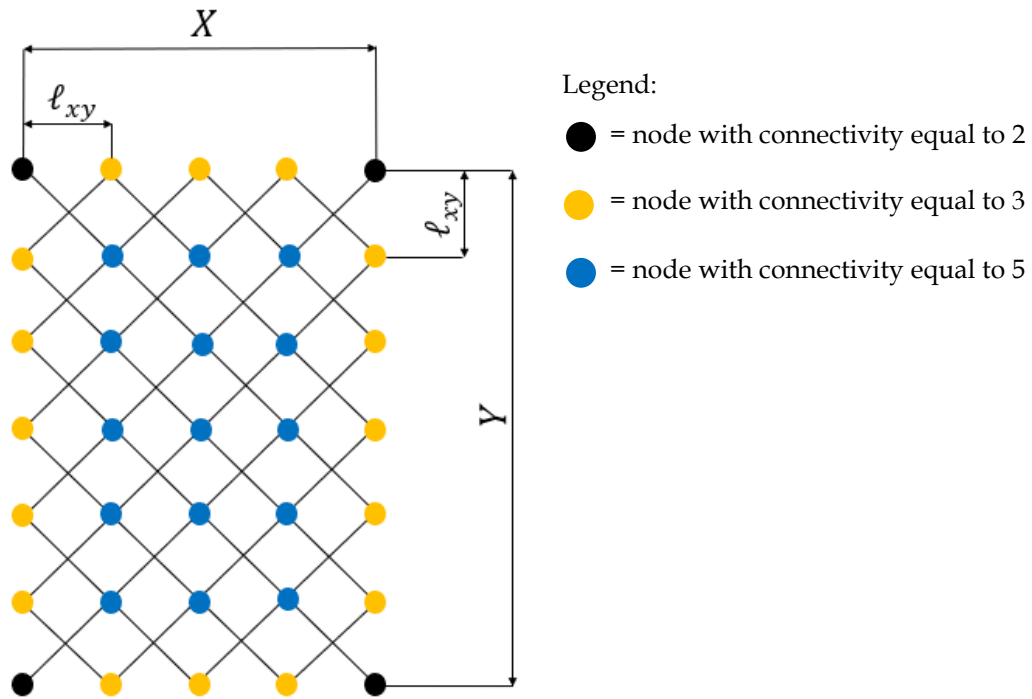


Figure 2.8. Types of the loaded nodes belonging to the upper plane of a lattice composed by bcp-z cells

As before, the stiffness and the apparent Young's modulus of the specimen is gettable from Eq. (2.15-2.17).

2.4 Bcp cell type

The same procedure is applied for a lattice with bcp cells. In this case there is not the answer coming from the vertical beams ($V'_v = 0$) and the loaded nodes can have connectivity equal to 1, 2 or 4. Fig. 2.9 reports the sketch of a loaded node with connectivity equal to 1.

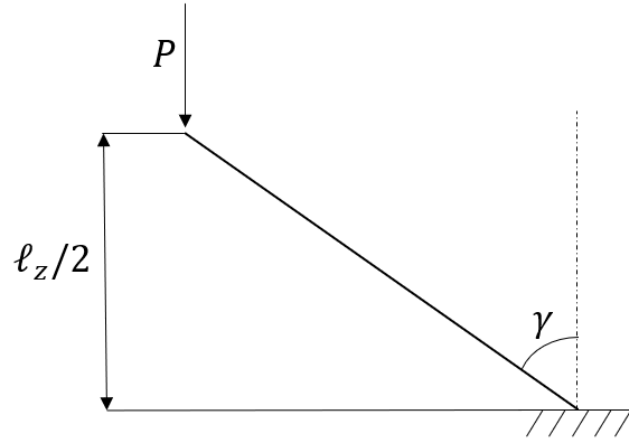


Figure 2.9. Loaded node with connectivity equal to 1 belonging to the upper plane of a lattice composed by bcp cells

Adapting Eq. (2.29-2.31), it is possible to evaluate the stiffnesses of the three kinds of loaded nodes:

$$k_1 = V'_0 \quad (2.34)$$

$$k_2 = 2V'_0 \quad (2.35)$$

$$k_4 = 4V'_0 \quad (2.36)$$

Referring to Fig. 2.10, Eq. (2.18) gives the number of loaded nodes with connectivity equal to 1; while the number of nodes that have connectivity equal to 2 and 4 are computable as follows:

$$N_2 = 2 \left(\frac{X}{\ell_{xy}} - 1 \right) + 2 \left(\frac{Y}{\ell_{xy}} - 1 \right) = 2(n_x - 1 + n_y - 1) = 2(n_x + n_y - 2) \quad (2.37)$$

$$N_4 = \left(\frac{X}{\ell_{xz}} - 1 \right) \left(\frac{Y}{\ell_{xz}} - 1 \right) = (n_x - 1)(n_y - 1) \quad (2.38)$$

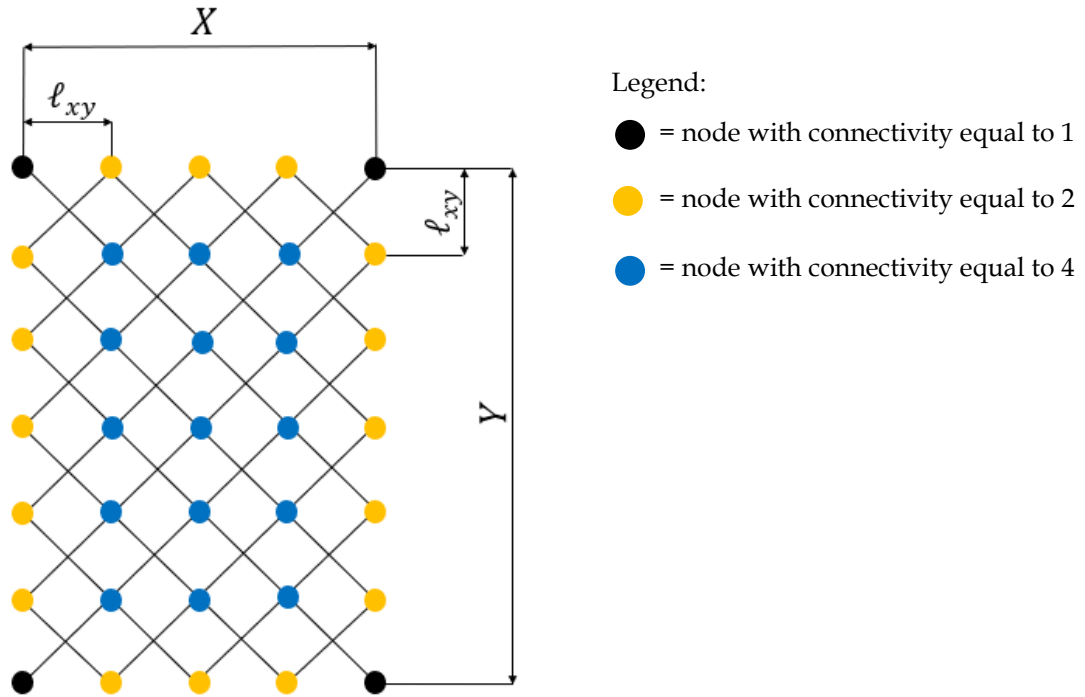


Figure 2.10. Types of the loaded nodes belonging to the upper plane of a lattice composed by bcp cells

The stiffness and the apparent Young's modulus of the specimen are computable using Eq. (2.16, 2.17, 2.24).

2.5 Analytical model's validation

The analytical model has been checked comparing its results with the ones obtained from a FEM simulator (Mechanical APDL by Ansys). A linear static analysis has been performed over the four types of lattice. Imposing a displacement and evaluating the reaction of the structure, the stiffness has been calculated.

The slenderness of the shortest beams of the reticular structure, i.e. the oblique beams, is imposed equal to 10 (minimum threshold for the Timoshenko's theory). The element chosen is beam4 (1D element with six degrees of freedom on each node) which

considers the shear effect. The mesh size has turned out to be irrelevant. The following parameters have been used:

- $E = 60000$ MPa
- $\nu = 0.33$
- $d = 1$ mm
- $n_x = 8$
- $n_y = 7$
- $n_z = 5$
- $\ell = 11.547$ mm in the case of cubic cells
- $\ell = 10.583$ mm and $\ell_{xy} = 12$ mm in the case of parallelepipedal cells

The constraints reflect the hypothesis of the analytical model: the only free degree of freedom is the vertical displacement (Fig. 2.11 shows one of the four cases).

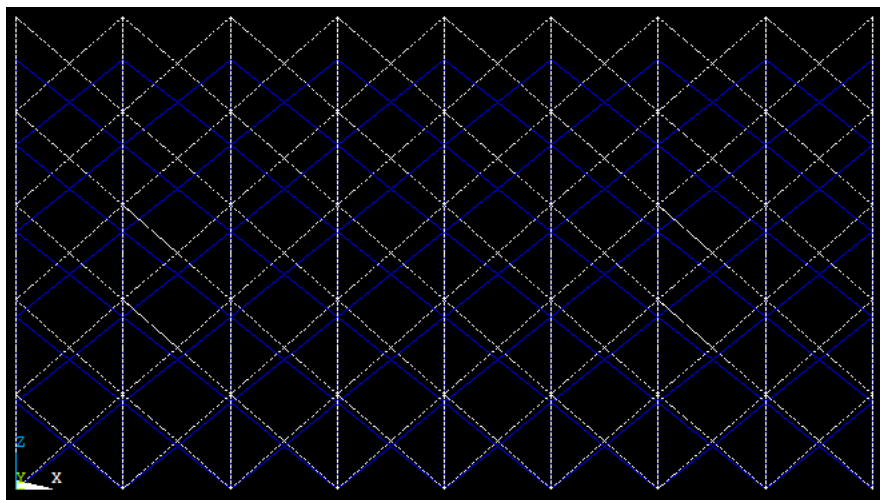


Figure 2.11. 1D numerical model (undeformed and deformed structure) used to check the analytical model on a lattice composed by bcp-z cells

The results fit very well with the ones proposed by the analytical model, as shown in Table 2.1. For this reason, the analytical model is validated.

Table 2.1. Comparison between analytical and numerical stiffnesses

Lattice type	Analytical stiffness [N/mm]	Numerical stiffness [N/mm]	Relative error [%]
Bcc-z	94469	94433	+0.038
Bcc	35702	35696	+0.017
Bcp-z	94231	94199	+0.034
Bcp	30114	30111	+0.010

Chapter 3

Specimens

Some significant samples with parametrical characteristics have been projected to evaluate experimentally their behavior under a compression load. The aim is to characterize them in terms of stiffness, apparent yield stress and apparent maximum stress to have an idea of the influence of the parameters. This is necessary to design the entire de-icing system patented by Politecnico di Torino in its optimal version. Obviously other studies must be performed too, such as thermal, fatigue and impact analyses.

3.1. Specimens design

The material chosen is AlSi10Mg. There are three factors that characterize a single specimen. Each factor has two possible options. The factors are:

- cell type;
- cell size;
- strut size.

The two cell types are bcc and bcc-z (Fig. 3.1).

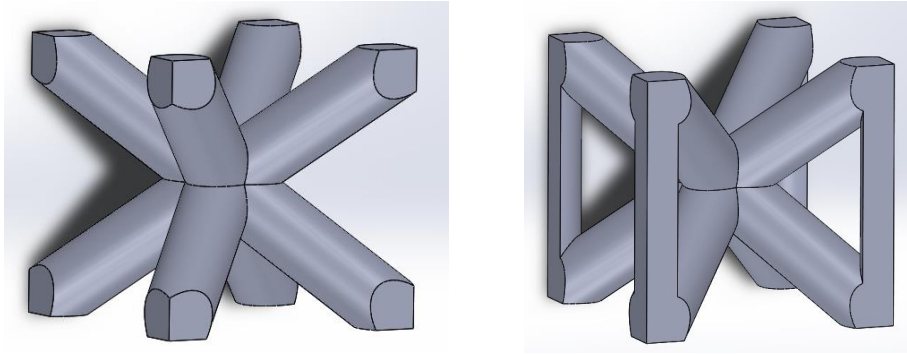


Figure 3.1. CAD geometries of a bcc cell (left) and a bcc-z cell (right)

The cell size can be equal to 4 mm or 5 mm, while the diameter of the struts can assume values equal to 1 mm or 1.2 mm. Not slender struts have been chosen because AM technologies can not build too much slender beams with enough geometrical and size accuracy. Moreover, there are also structural requirements that must be met: the wing loading, i.e. the weight supported by the wings of an aircraft, can be 70 Kg/m² (it is the case of the Piper), but also 730 Kg/m² (as it is for Boeing 747).

The samples are prismatic, with the height about twice the basis' side and always equal to 40 mm to respect the order of magnitude of the real component. Table 3.1 collects all the data for each specimen. The name of each sample reports the cell size and the strut size (both expressed in mm) followed by the cell type: AV (from the Italian "Aste Verticali") indicates the bcc-z type, while NA ("Nessun' Asta") the bcc one.

Table 3.1. Specimens' geometrical and size nominal characteristics

Sample	Cell type	Cell size [mm]	Strut size [mm]	Specimen dimensions [mm ³]
4_1_AV	bcc-z	4	1	21x21x40
4_1.2_AV	bcc-z	4	1.2	21x21x40
5_1_AV	bcc-z	5	1	21x21x40
5_1.2_AV	bcc-z	5	1.2	21x21x40
4_1_NA	bcc	4	1	20x20x40
4_1.2_NA	bcc	4	1.2	20x20x40
5_1_NA	bcc	5	1	20x20x40
5_1.2_NA	bcc	5	1.2	20x20x40

As example, two specimens' CAD geometries are depicted in Figs. 3.2 and 3.3.

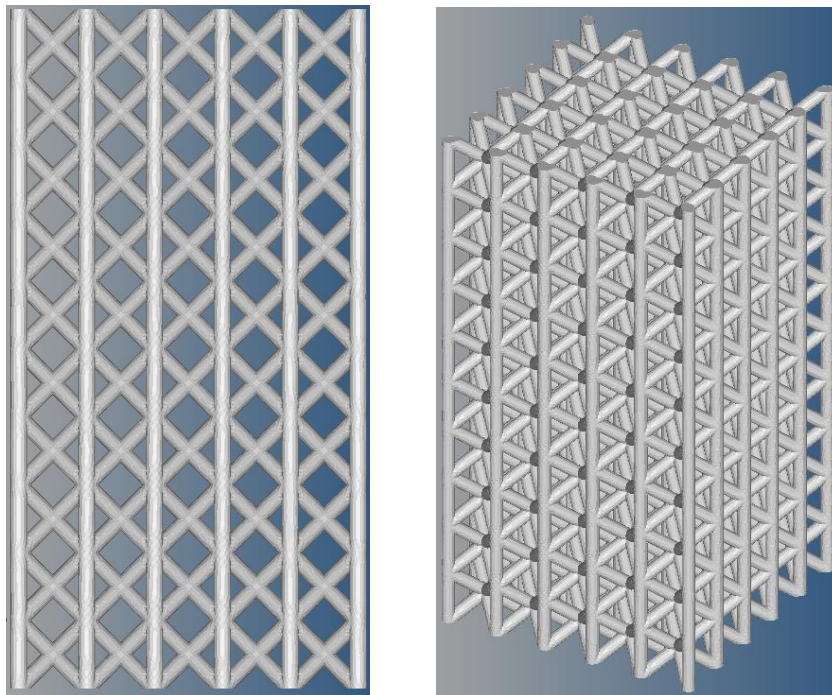


Figure 3.2. CAD geometries of 4_1_AV

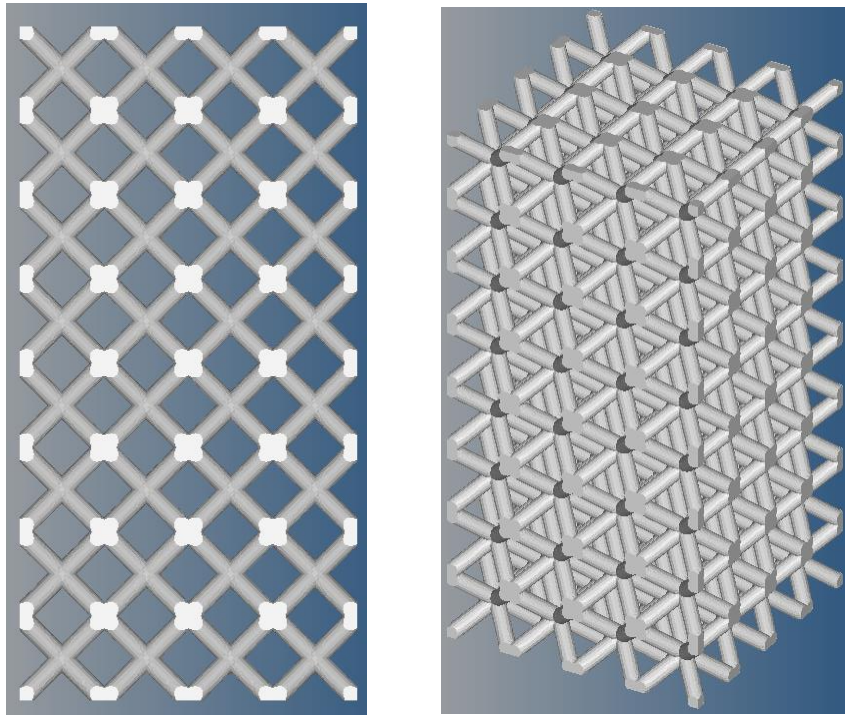


Figure 3.3. CAD geometries of 5_1.2_NA

3.2. Specimens fabrication

The specimens have been produced by Selective Laser Melting technology (SLM), using an EOS machine (M270 Dual Mode Version, showed in Fig. 3.4).



Figure 3.4. EOS M270 Dual Mode Version [26]

This technique allows the creation of near-net-shaped components. The input data for the machine is just a CAD file in the "stl" file format, that represents the geometry of the piece that must be built. Even orientation and position on the substrate must be specified by the operator. The substrate is necessary to keep the part in its initial position. The entire process must be performed with absence of oxygen because metallic powder can oxidize suddenly (the surface/volume ratio is very high) causing fire and/or explosions. For this reason, an inert atmosphere must be ensured using argon or nitrogen and only specialized operators can work by these machines.

Each sample is built layer by layer. The growth direction of the specimens during their production is their highest size dimension, the same of the compressive load that will destroy them. After a layer of powder is spread on the substrate by a roller, the laser melts some powder in such a way to draw the horizontal section of the part. This powder solidifies instantaneously, fixing itself on the substrate. When the section is finished, another layer is spread on the previous one and the process restarts.

Fig. 3.5 shows a sketch of the process.

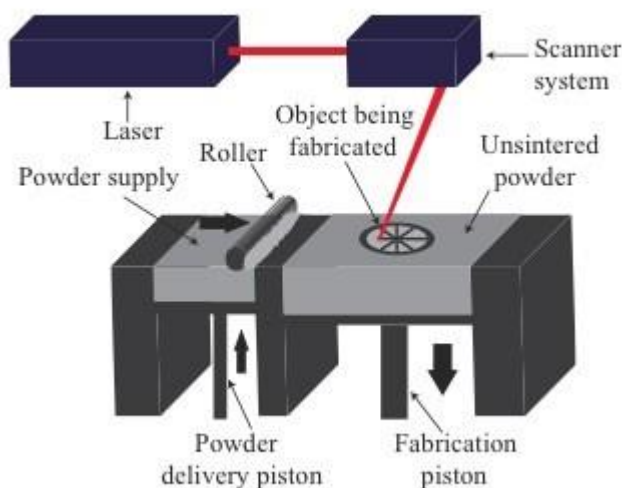


Figure 3.5. Scheme of the SLM process [27]

The powder used is EOS Aluminum AlSi10Mg: Table 3.2 shows its chemical and physical properties contained in the material data sheet [26]; while the parameters for the specimens' production are listed in Table 3.3.

Table 3.2. Chemical, physical and mechanical properties of EOS Aluminum AlSi10Mg powder

Al	balance
Si	9.0 - 11.0 wt-%
Fe	≤ 0.55 wt-%
Cu	≤ 0.05 wt-%
Mn	≤ 0.45 wt-%
Mg	0.2 - 0.45 wt-%
Ni	≤ 0.05 wt-%
Zn	≤ 0.10 wt-%
Pb	≤ 0.05 wt-%
Sn	≤ 0.05 wt-%
Ti	≤ 0.15 wt-%
Relative density approx.	99.85 %
Density	2.67 g/cm ³
Modulus of elasticity in vertical direction	60±10 GPa
Yield strength (R _{p0,2}) in vertical direction	230±15 MPa
Typical achievable part accuracy	100 μm
Smallest wall thickness approx.	0.3 - 0.4 mm
Surface roughness, as built, cleaned	Ra = 6 - 10 μm; Rz = 30 - 40 μm

Table 3.3. Production parameters of the samples

Spot size	Scanning speed	Powder layer thickness	Laser power	Heat treatment
100 μm	800 mm/s	30 μm	195 W	in air for 2h at 300°C for stress relieving

After the creation, a cleaning must be done to remove the powder particles trapped inside the lattice. This is achieved by special shakers. Then the samples must be separated from the substrate through a Wire Electrical Discharge Machining (WEDM). Before doing this operation, a thermal treatment is needed to eliminate the residual stresses: they can be so high to break the components or to deform them.

Figs. 3.6 and 3.7 report the photos of the samples.

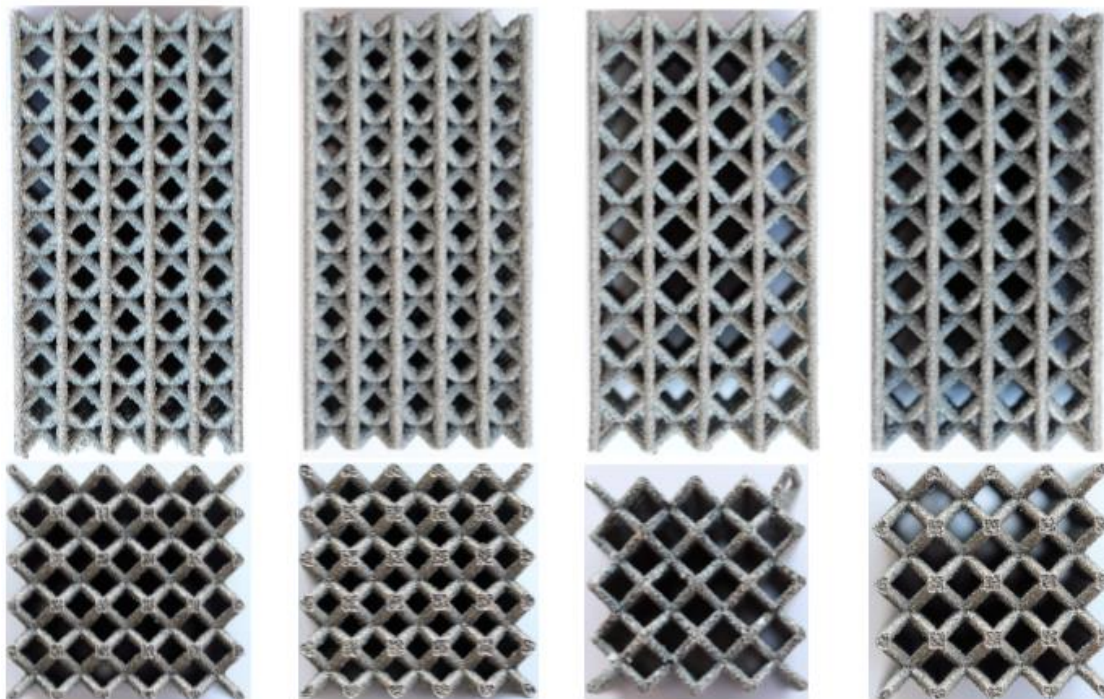


Figure 3.6. Bcc-z specimens [15, 16]

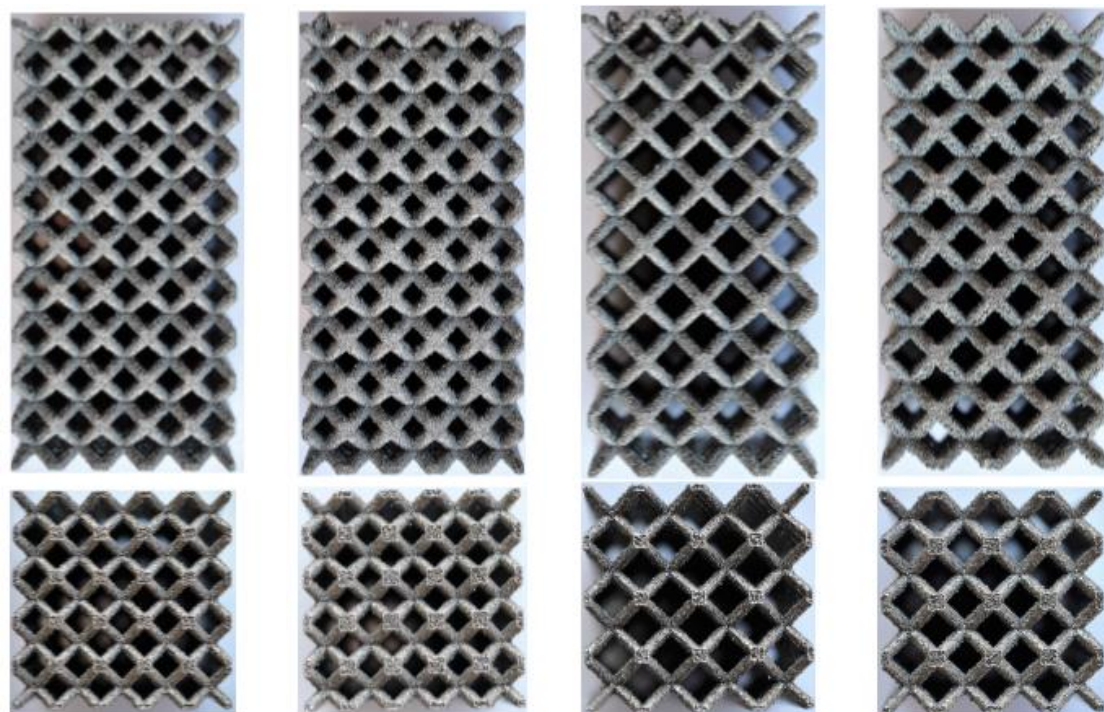


Figure 3.7. Bcc specimens [15, 16]

3.3. Dimensional validation

The three sizes in the space of the samples have been measured using a Vernier gauge (Suki International). In Table 3.4 the results of these measures are reported.

Table 3.4. Specimens' sizes

Sample	Height [mm]	Depth [mm]	Width [mm]
4_1_AV	40.30	21.10	21.15
4_1.2_AV	40.45	21.30	21.35
5_1_AV	40.25	21.20	21.30
5_1.2_AV	40.65	21.30	21.30
4_1_NA	40.50	20.25	20.25
4_1.2_NA	40.50	20.25	20.30
5_1_NA	40.30	20.25	20.30
5_1.2_NA	40.45	20.25	20.30

There is a relatively high discordance between nominal and real measures. This is due prevalently to size and geometrical errors coming from the process. Even the cutting operation (performed through WEDM) that is needed to separate the specimen from the substrate, causes some irregularities. Other less influential factors are the uncertainty of the measurements' procedure and of the instrument itself.

However, these divergences will be not considered for the computation of the mechanical properties, since their error contribution is negligible. Only size errors in the diameter of the beams will be taken in account for the numerical model's calibration, as it will be explained in paragraph 5.2.2. In fact, an optical analysis of the samples has revealed the real geometrical and size characteristics of the struts [14]. An optical microscope Leica DMI 5000M (Fig. 3.8) has been used.



Figure 3.8. Optical microscope Leica DMI 5000M [28]

As shown in Fig. 3.9, the struts have a high rugosity and a lot of imperfections and defects that determine a great lack of material. Especially the nodes of the lattice, that are the most significant points of the entire geometry since here the fractures nucleate, appear strongly deformed.

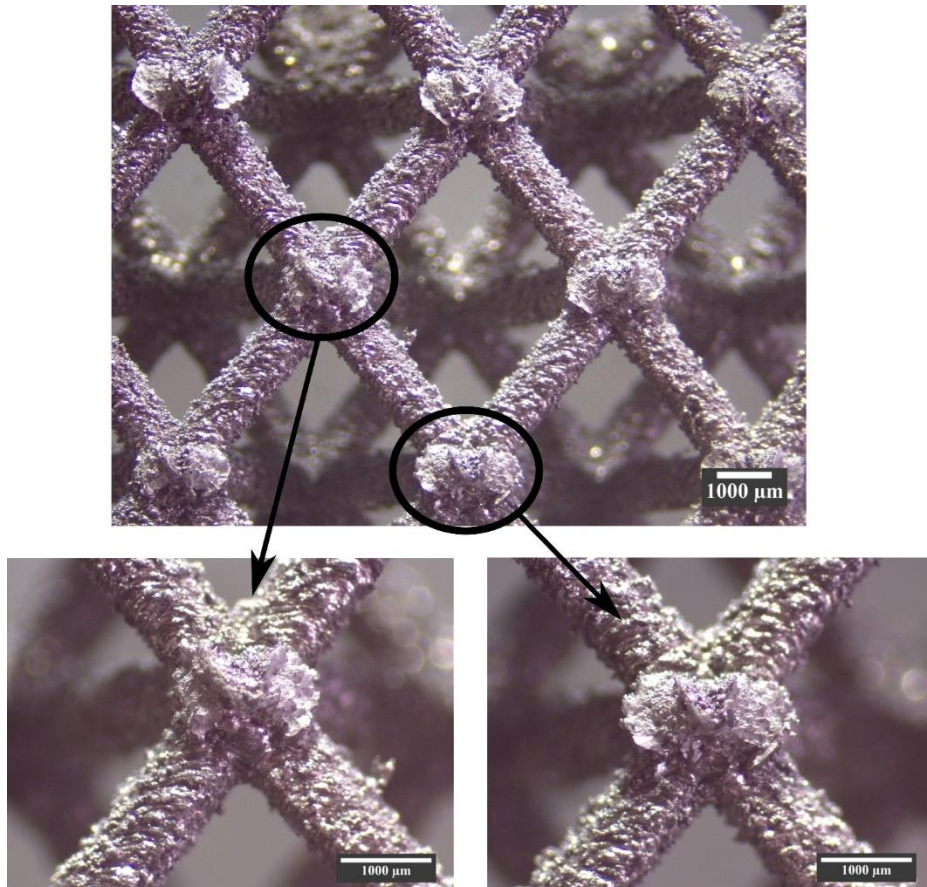


Figure 3.9. Compressed 5_1_NA sample with detailed views of the nodes [14]

Table 3.5 shows the real diameters, expressed as an average over many measurements. For bcc-z specimens, only vertical beams have been measured at different positions along the vertical axis [14]. It can be noticed that the real diameters are always lower than the nominal ones.

This can be explained thinking on how the vertical struts are produced. In fact, since the melted layer is in direct contact with the melted section of the previous layer, no other granules are melted into the structure. The resulting diameter is smaller because of the merging of the powder particles.

On the other hand, bcc specimens, for which the standard deviation is higher, have only oblique beams. In this case, the real measure is higher than the nominal one. This happens because, during the production, the melted powder is partly in contact with some portions of the non-melted previous layer, that are welded into the structure [14]. However, since this added material gives no structural contribution, but only a higher surface roughness, it will be not considered in the numerical model's calibration (paragraph 5.2.2). Contrariwise, the diameters of all the beams will be decreased along their axis and, with a major extent, by their extremes thanks to chamfers.

Table 3.5. Comparison between real and nominal diameters

Specimen	Nominal Diameter [mm]	Real Diameter [mm]	Standard deviation [mm]	Relative error between nominal and real diameter [%]
4_1_AV	1	0.960	0.045	-4%
4_1.2_AV	1.2	1.165	0.049	-2.9%
5_1_AV	1	0.959	0.060	-4.1%
5_1.2_AV	1.2	1.173	0.052	-2.2%
4_1_NA	1	1.124	0.065	+12.4%
4_1.2_NA	1.2	1.286	0.056	+7.2%
5_1_NA	1	1.072	0.063	+7.2%
5_1.2_NA	1.2	1.304	0.079	+8.7%

Chapter 4

Experimental validation

A Zwick-Roell Z050 (Fig. 4.1), whose cell load capacity is 50 kN, has been used for the compression tests.



Figure 4.1. Zwick-Roell Z050 [29]

The scheme depicted in Fig. 4.2 represents the setup of the machinery.

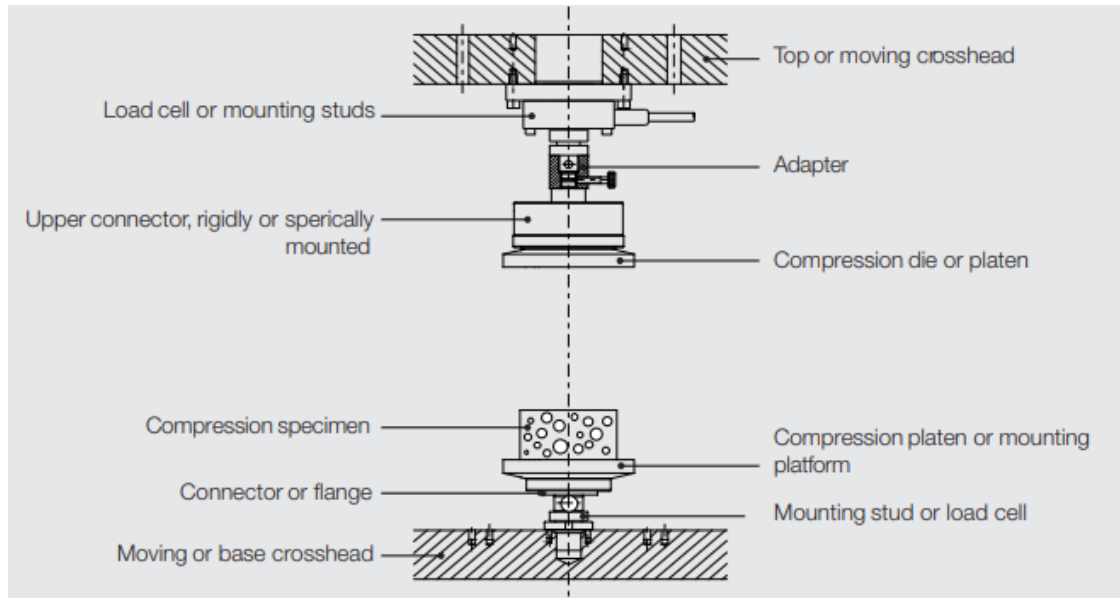


Figure 4.2. Setup principle for a compression test device [17]

All the tests have been filmed to better understand the physics of the problem. Each sample has been compressed along its highest dimension. Great attention has been paid to put them frontally in respect to the camera and in the center of the fixed platen to avoid asymmetries of the load. Moreover, before each test, an accurate cleaning of the fixed platen, refraining from scratching it, was performed to remove the waste of the previous broken sample.

The tests are static, because they have been performed with a low constant deformation velocity (1 mm/min). A preload equal to 1 kN has been necessary to stabilize the answer of the sample.

Depending on the cell type, different failures modalities have been observed.

4.1. Results

The results of the experimental tests performed on the cubic cell type lattices are reported in Figs. 4.3-4.10. There are two curves for each kind of specimen: one has been

taken from previous thesis' works [15, 16].

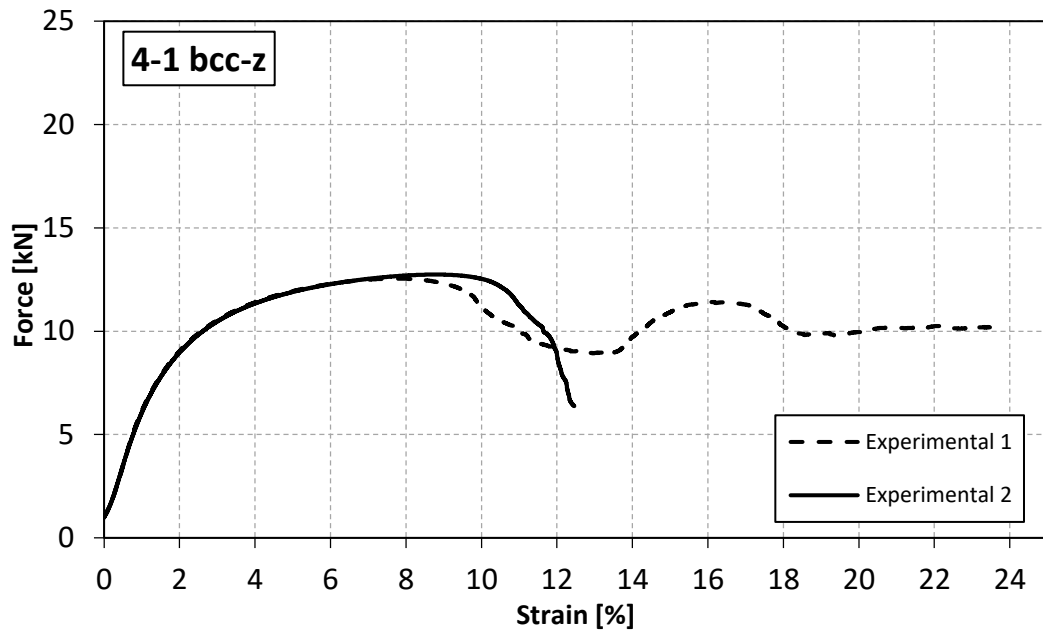


Figure 4.3. Experimental results for 4_1_AV samples

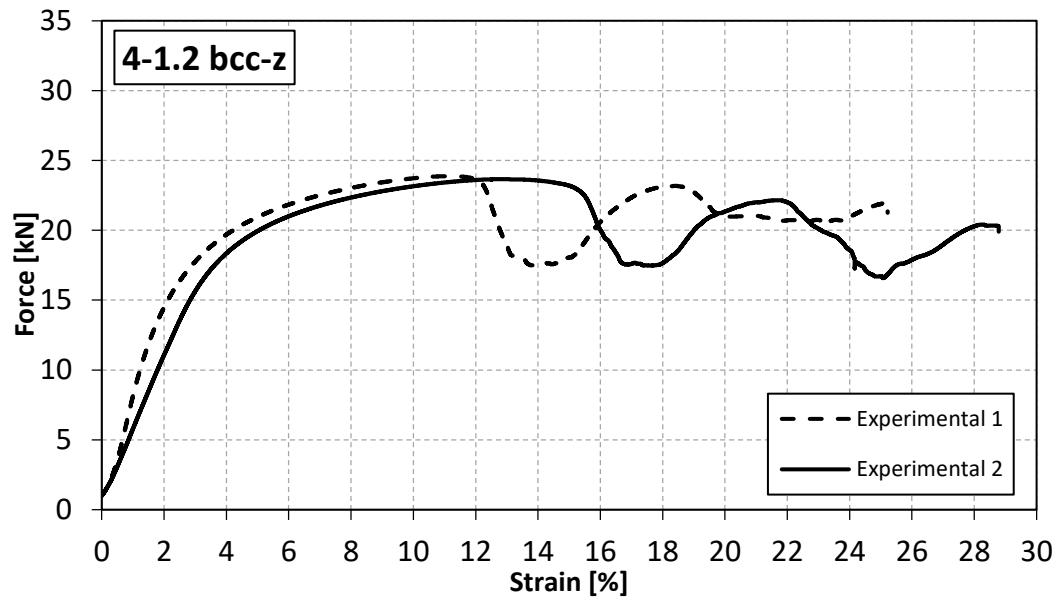


Figure 4.4. Experimental results for 4_1.2_AV samples

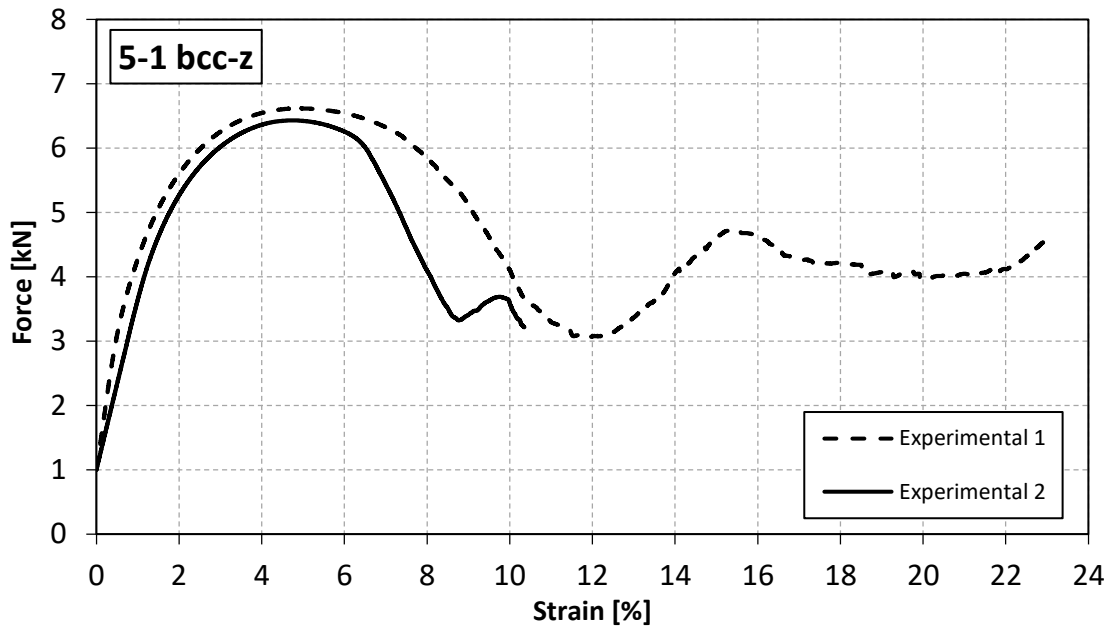


Figure 4.5. Experimental results for 5_1_AV samples

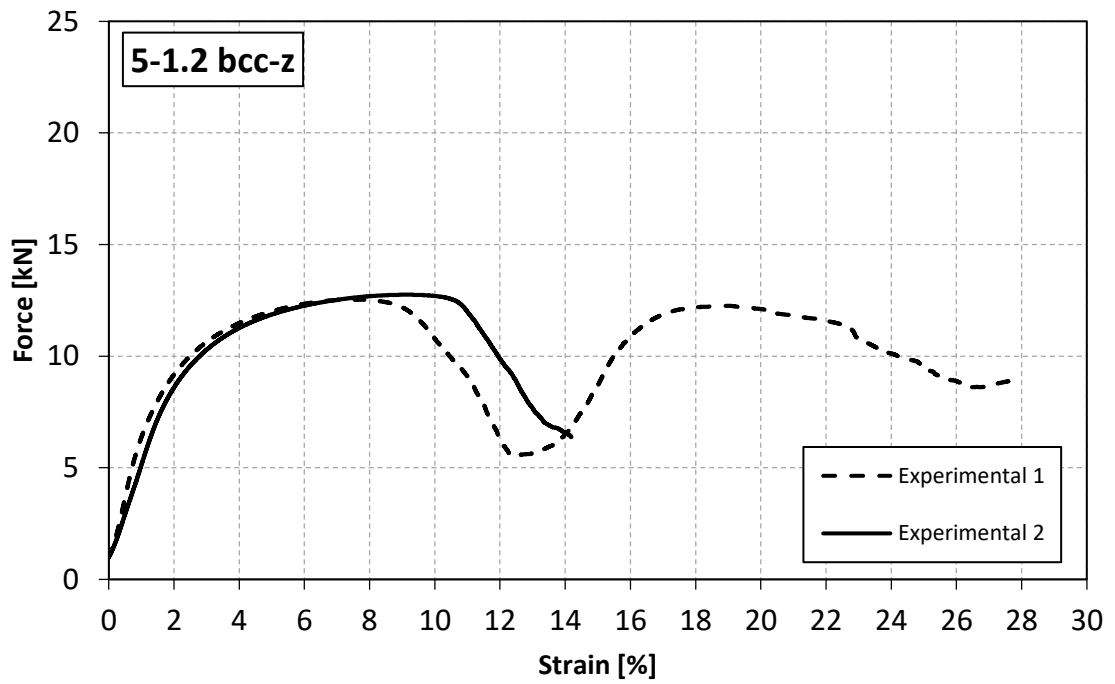


Figure 4.6. Experimental results for 5_1.2_AV samples

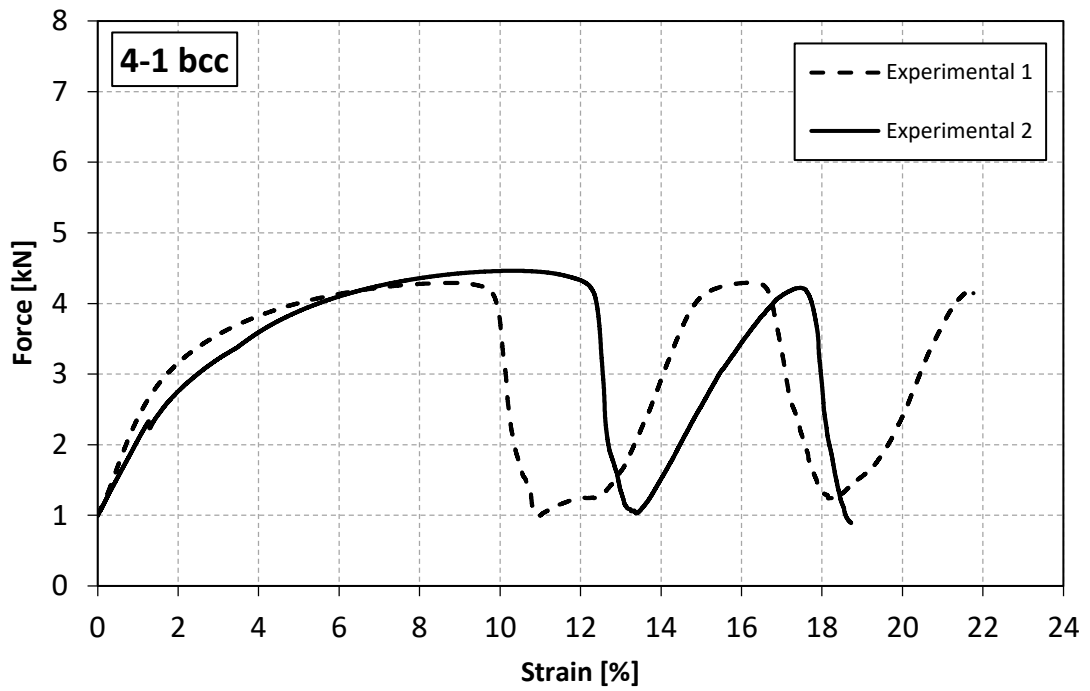


Figure 4.7. Experimental results for 4_1_NA samples

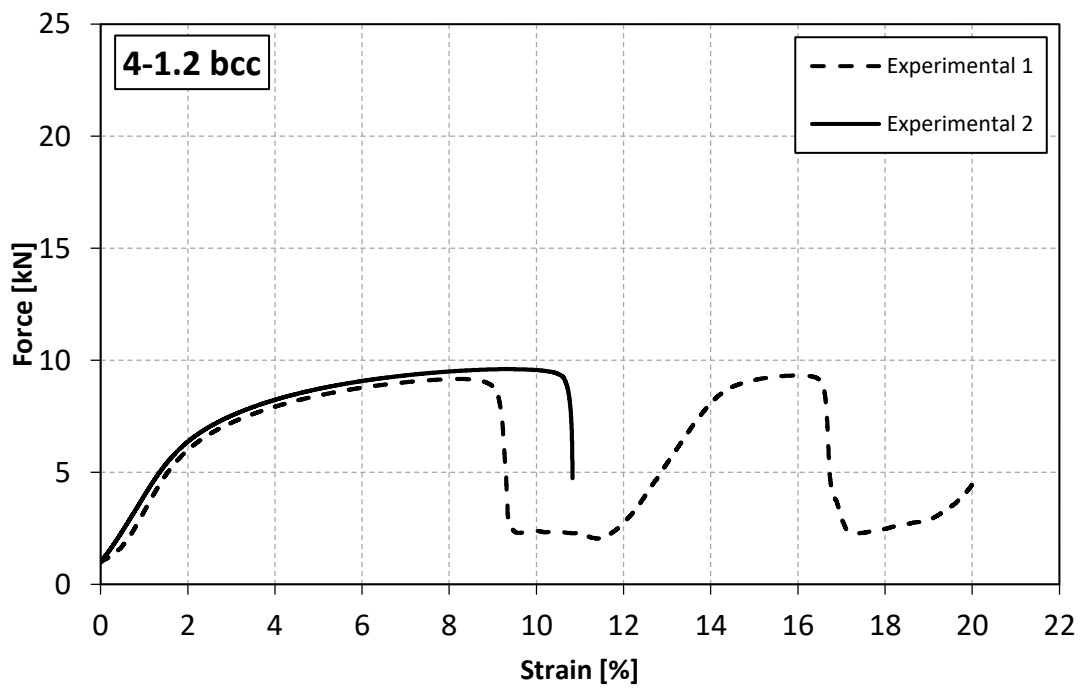


Figure 4.8. Experimental results for 4_1.2_NA samples

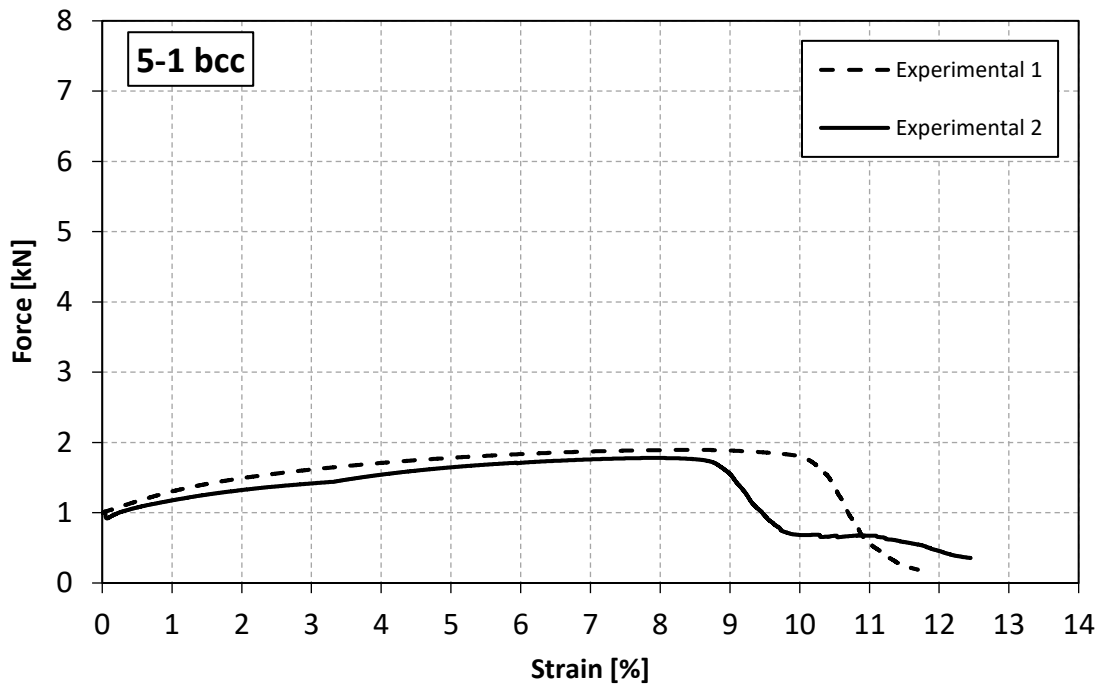


Figure 4.9. Experimental results for 5_1_NA samples

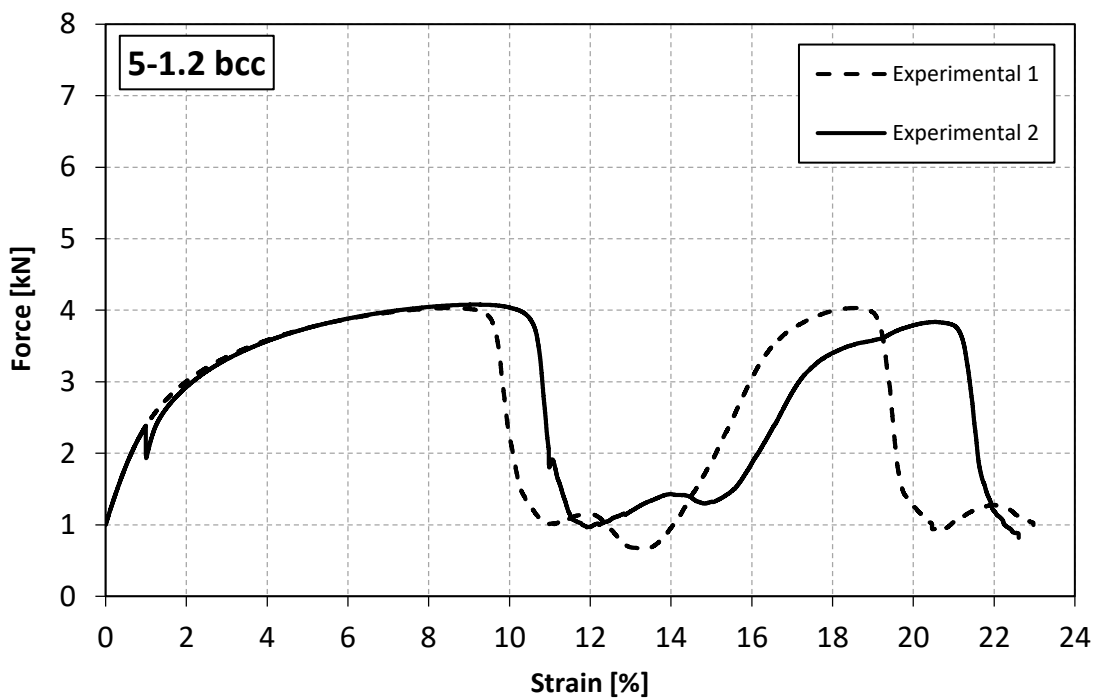


Figure 4.10. Experimental results for 5_1.2_NA samples

Bcc-z specimens have some beams along the load which work by stretching. This causes instability: the resulting failure happens by buckling and is fragile. The first struts

to fail are situated by one of the lateral faces at a height equal to a half of the total one. Immediately after, the failure propagates along the beams belonging to a plane inclined by 45° in respect to the horizontal one (Fig. 4.11), because the cells are cubic.

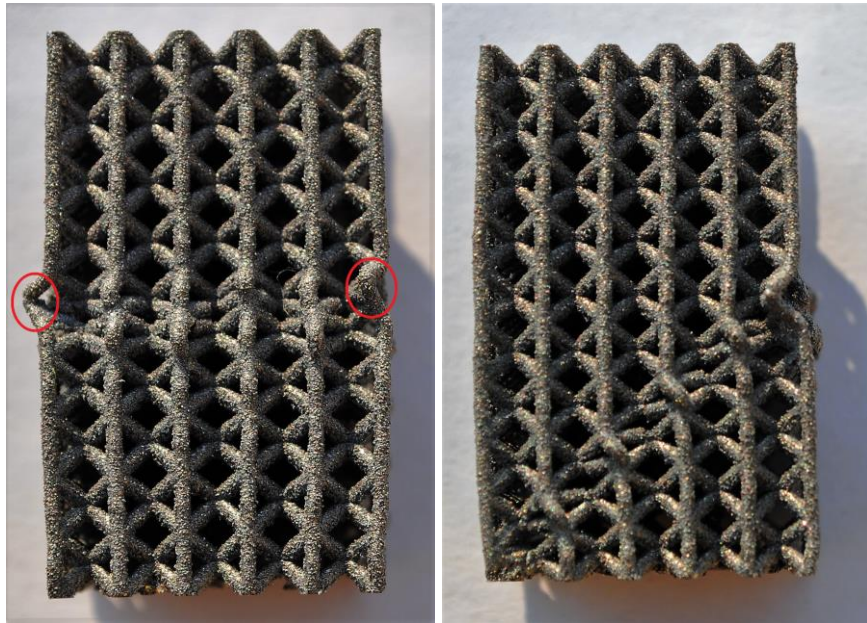


Figure 4.11. Failure modality seen by two directions for a 4_1_AV sample [15, 16]

During this phase, the load on the sample decreases because of these failures. Only when a denser plane is created the load restarts to increase. Now, depending on the diameter of the beams, two cases have been observed. If the diameter is equal to 1 mm, the sample breaks along a new plane that is symmetric to the first failure plane and very close to it; while if the diameter is equal to 1.2 mm, the new failure plane is perpendicular to the first one (Fig. 4.12).

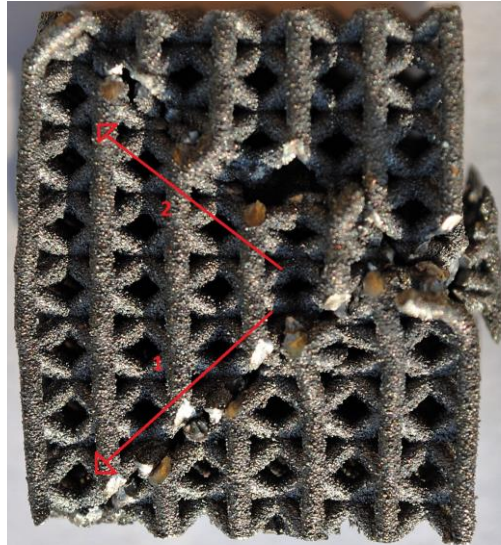


Figure 4.12. Failure modality for a 4_1.2_AV sample [15, 16]

Buckling does not exist in case of bcc cell type, that works by bending. The first beams to fail belong another time to a lateral face and are the ones by the middle height of the sample. The fracture propagates always along a plane inclined by 45° in respect to the horizontal one. Even for bcc specimens, the load restarts to increase because of the new denser plane, but, as soon as the load is sufficient, the sample breaks into two pieces along that plane, by the nodes of the struts (Fig. 4.13).

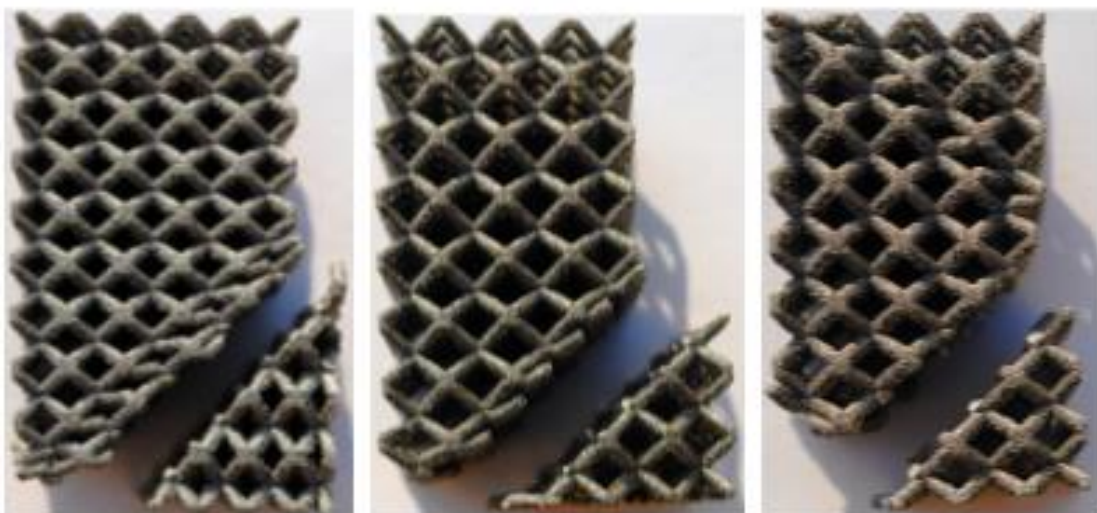


Figure 4.13. Failure modality for three bcc samples (4_1_NA, 5_1_NA and 5_1.2_NA) [15, 16]

As expected bcc-z samples are stronger than bcc ones. However, another aspect has been underlined by these compression tests. The failure is catastrophic for bcc specimens because it implies the division into two pieces of the lattice. This does not happen for bcc-z frames, that remain compact even after the second failure [15, 16].

For the greatest part of the specimens there is a very good repeatability in the linear behavior. A pre-existing Matlab code [16], uses a linear regression to evaluate the apparent Young's modulus of the lattice starting from the raw data coming from the compression test. The geometrical values used for the computations are the nominal ones. Even the stiffness, the apparent yield stress and the apparent maximum stress have been evaluated in the same way.

Table 4.1, which collects all these outcomes, shows that there is a quasi-perfect repeatability about the maximum apparent stress (this parameter is the most characterizing). The deviation from the average values are higher for the apparent yield stress and much higher for the apparent Young's modulus/stiffness. Because of this aspect, much attention will be paid on the fitting of the apparent maximum stress between experimental and numerical results.

A previous thesis' work [15] had noticed that the geometry of the cell is the most influencing feature for the mechanical properties. This conclusion has been obtained from experimental tests performed over only one series of eight different specimens. It can be noticed also that, for each kind of topology, the stiffness increases if the number of cells and/or the struts size increases. This can be explained knowing the foam's theory [30, 31], for which, given a certain topology, the mechanical properties are always proportional to the relative density of the sample.

Table 4.1. Experimental results

Specimen		Experimental apparent Young's modulus [MPa]	Experimental stiffness [N/mm]	Experimental apparent yield stress [MPa]	Experimental apparent maximum stress (first peak) [MPa]
4_1_AV	Series 1	1224	13495	18	28
	Series 2	1054	11620	20	29
	Average	1139	12557	19	29
	Deviation	7%	7%	5%	0%
4_1.2_AV	Series 1	1976	21785	34	54
	Series 2	1465	16152	37	54
	Average	1721	18974	36	54
	Deviation	15%	15%	3%	0%
5_1_AV	Series 1	874	9636	10	15
	Series 2	565	6229	13	15
	Average	720	7938	12	15
	Deviation	22%	22%	8%	0%
5_1.2_AV	Series 1	1359	14983	19	28
	Series 2	933	10286	22	29
	Average	1146	12635	21	29
	Deviation	19%	19%	5%	0%
4_1_NA	Series 1	366	3660	8	11
	Series 2	216	2160	10	11
	Average	291	2910	9	11
	Deviation	26%	26%	11%	0%
4_1.2_NA	Series 1	857	8570	17	23
	Series 2	717	7170	19	24
	Average	787	7870	18	24
	Deviation	9%	9%	6%	0%
5_1_NA	Series 1	74	740	5	5
	Series 2	63	630	4	4
	Average	69	690	4	5
	Deviation	9%	9%	0%	0%
5_1.2_NA	Series 1	376	3760	8	10
	Series 2	253	2530	9	10
	Average	314	3140	8	10
	Deviation	19%	19%	13%	0%

Chapter 5

Numerical modeling

The numerical model is obtained using a commercial FEM software, i.e. HyperWorks (Optistruct) by Altair. Since the struts are not slender enough to be considered beams, a 3D numerical model has been elaborated.

5.1. Linear numerical model

A linear static approach has been adopted to compute the stiffness of each specimen. A mesh analysis has been carried out by changing the following parameters:

- type of elements
- ideal mesh size
- upper limit of the mesh size
- lower limit of the mesh size
- order of the shape functions

The optimal mesh characteristics are reported in Table 5.1.

Table 5.1. Mesh characteristics for the numerical model

Type of elements	tetrahedral
Ideal mesh size	0.235
Upper limit of the mesh size	0.3
Lower limit of the mesh size	0.164
Order of the shape functions	first

The mesh is composed by tetra elements (4 nodes and 6 degrees of freedom per node). It is not so fine to avoid too much long simulation times. The distortion of the elements is controlled through a mesh quality check. The load is defined as an imposed displacement on the upper plane's nodes (kinematic load).

Bottom plane nodes are constrained along the load direction. Only one node is completely constrained to make the structure isostatic. The analysis is linear static. Figs. 5.1 and 5.2 reports two examples of this kind of model with a detailed view to show the mesh.

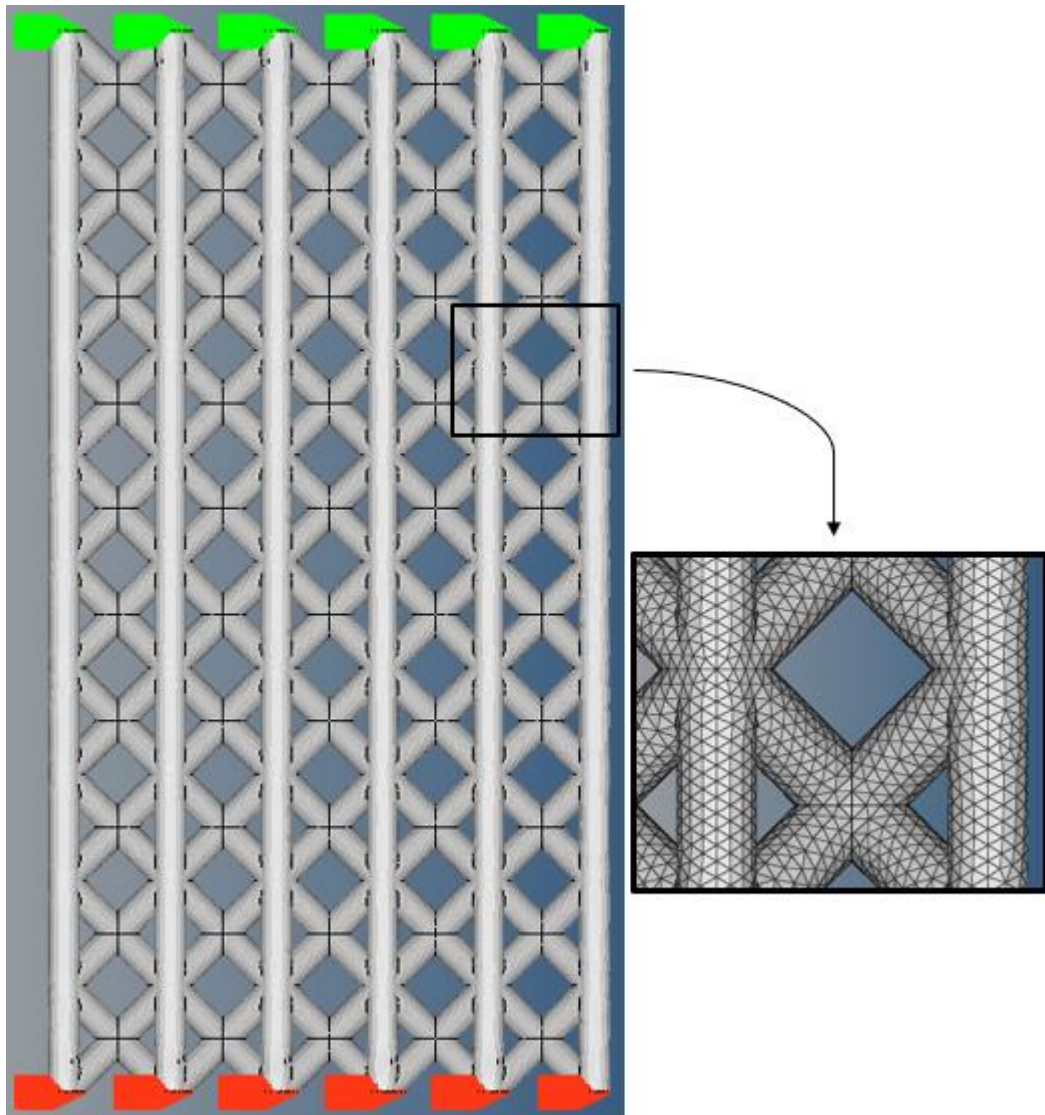


Figure 5.1. Numerical model of 4_1.2_AV samples with detailed view of the mesh

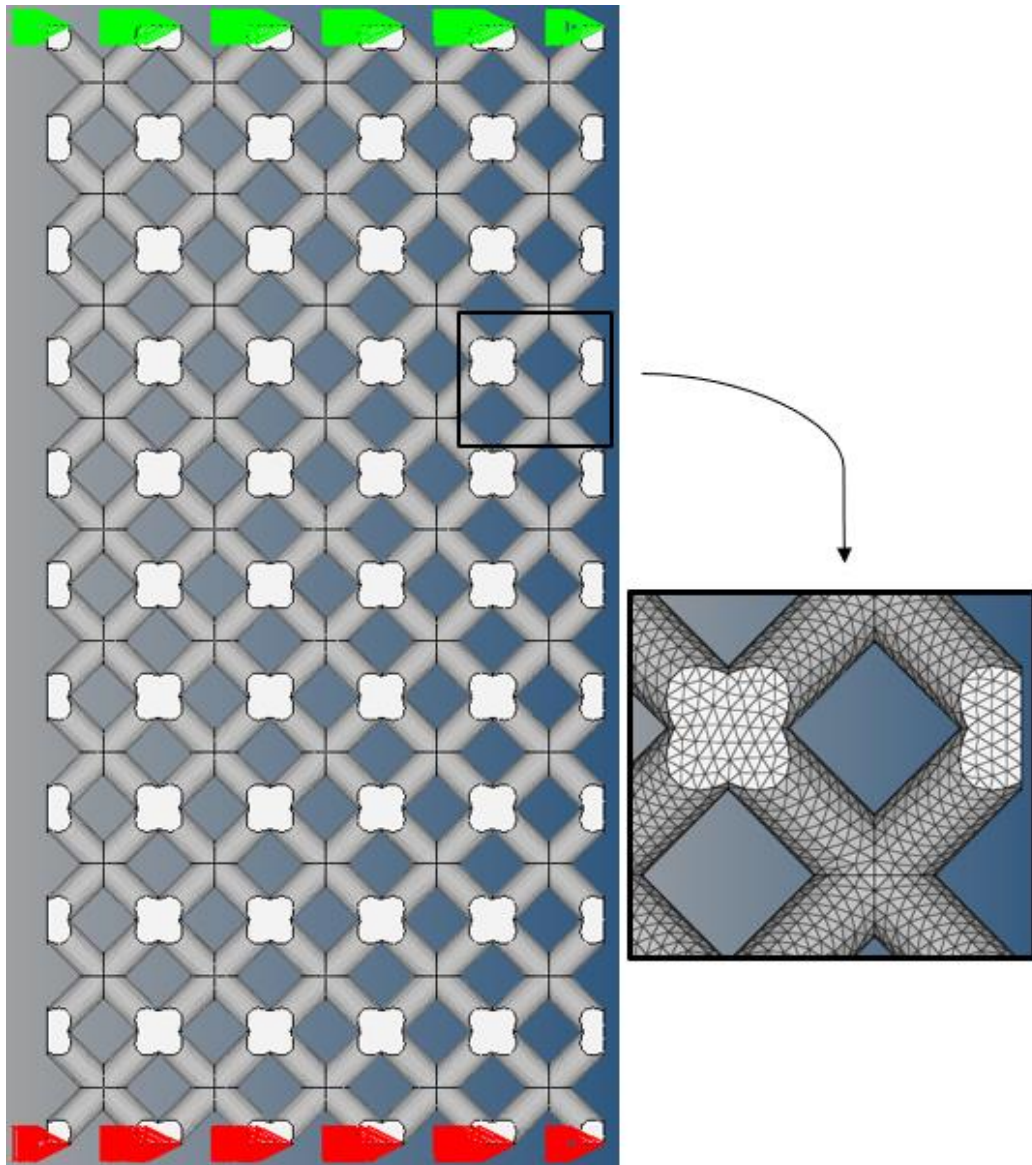


Figure 5.2. Numerical model of 4_1.2_NA samples with detailed view of the mesh

5.1.1. Linear numerical vs experimental results

Fig. 5.3 reports the relative errors in stiffness when a linear 3D numerical model is used. It can be noticed that this technique gives too much high results.

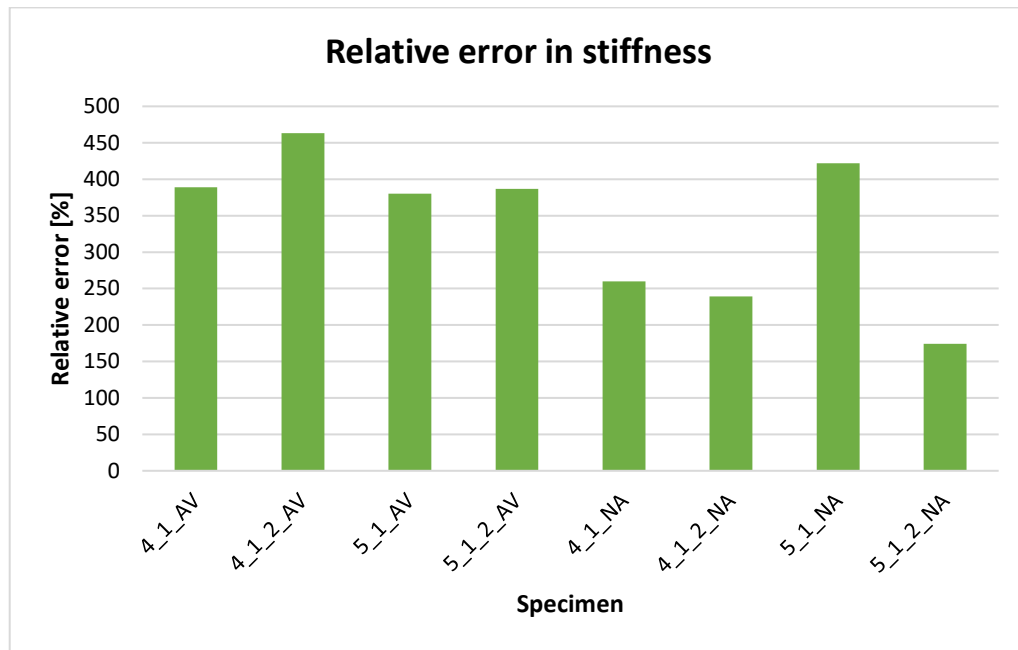


Figure 5.3. Relative errors in stiffness between linear numerical and experimental results

The linear approach is not reliable because the structure does not work only in the linear static field. It can be proved, even numerically, that the lattice does not plasticize suddenly, but progressively, starting from the nodes, because of the notch effect.

In fact, the equivalent tension (Von Mises), plotted on the 3D numerical model, exceeds the yield stress of the material (230 MPa) very soon. This localized plasticization increases by increasing the load and it makes the linear static approach non-applicable. In Fig. 5.4, an example of this aspect is reported: the 4_1.2_NA specimen, under just 4000 N (about 9200 N is the maximum experimental peak) feels a maximum stress equal to 498 MPa, much higher than yield tension of the material. Moreover, it can be noticed that the first points of the structure to exceed the yield stress of the material are the nodes, the most critical zones for a bcc sample.

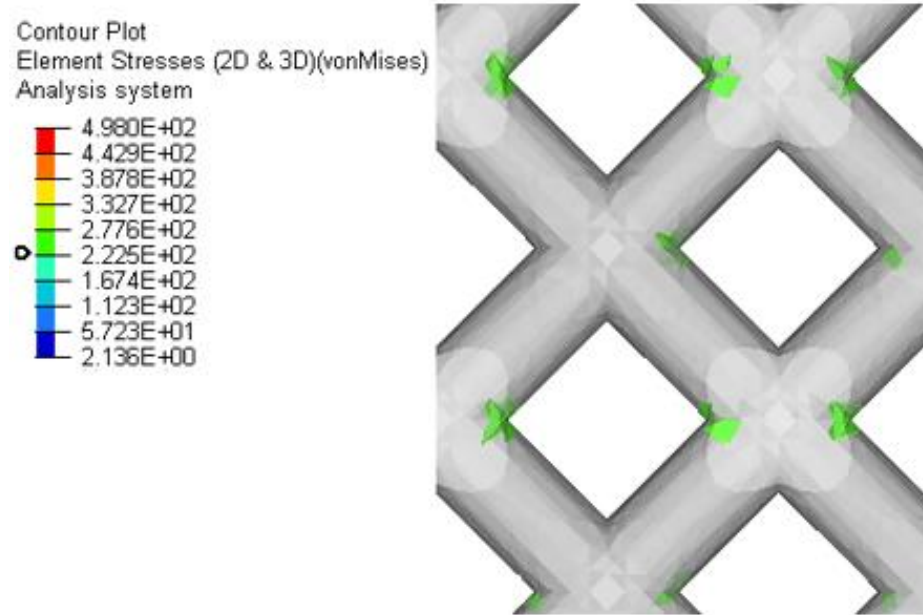


Figure 5.4. Tension exceeding the yield stress just under 4000 N of compressive load in the linear numerical model of 4_1.2_NA samples

For this reason, it is necessary to change the kind of analysis. Instead of a linear static approach, a non-linear quasi-static one will be used. This allows to consider the plasticization of the material and to compare directly the experimental curves with the numerical ones. In this way, not only the stiffness, but also the apparent yield stress and the apparent maximum stress can be compared with the experimental results.

5.2. Bi-linear numerical model

This kind of model is equal to the 3D linear one. The difference is the presence of the non-linearity relative to the material. Moreover, the simulation is no more static, but quasi-static.

As input data, not only the elastic modulus ($E = 60000 \text{ MPa}$) must be specified, but also the yield stress ($\sigma_y = 230 \text{ MPa}$) and the strength coefficient H , that represents the slope of the stress-strain curve of the material after the yield. Since the solutions are

influenced now by many parameters, it is important to understand the effect of each of them through a sensitivity's analysis. In this way, a careful calibration of the model is possible.

5.2.1 Sensitivity's analysis

Sensitivity's analysis is useful to understand the influence of some parameters over the numerical model's results. This study has been performed only on 4_1_AV sample. Initially only a perfectly plastic material has been considered:

$$H = 0 \text{ MPa}$$

The following three parameters have been taken in account (one is relative to the geometry, the others to the material):

- diameter of the struts;
- Young's modulus of the material;
- yield stress of the material.

The nominal values of these parameters are:

- $d = 1 \text{ mm}$
- $E = 60000 \text{ MPa}$
- $\sigma_y = 230 \text{ MPa}$

The two plots reported in Figs. 5.5 and 5.6 show the stress-strain curves of the material (perfectly plastic) obtained by varying one of the two material's parameters (E and σ_y).

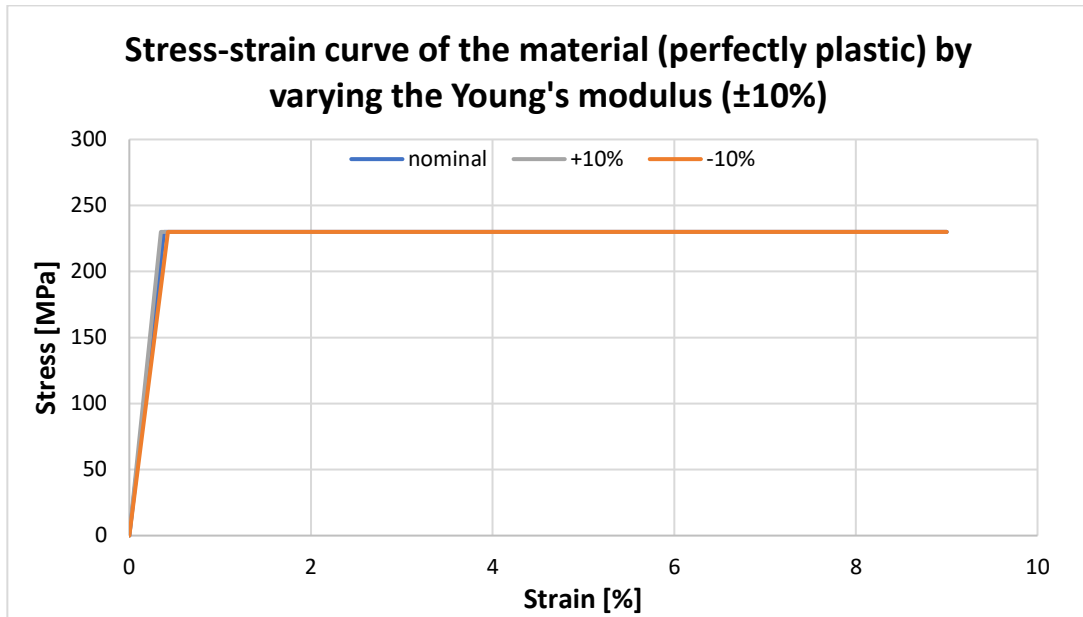


Figure 5.5. Stress-strain curves of the material (perfectly plastic) obtained by varying E

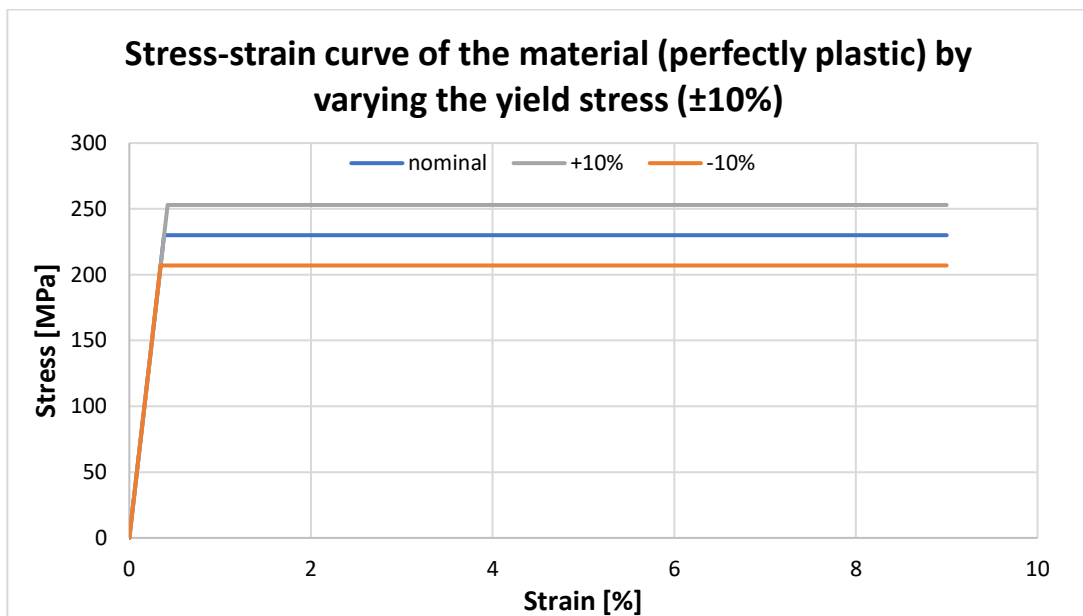


Figure 5.6. Stress-strain curves of the material (perfectly plastic) obtained by varying σ_y

It should be noticed that a variance of 10% over the yield stress exceeds its tolerance, that is lower than 7% [26].

The graphs reported in Figs. 5.7-5.9 show the differences between the results of the model with the nominal parameters and those of the model with one of the parameters increased or decreased by 10%.

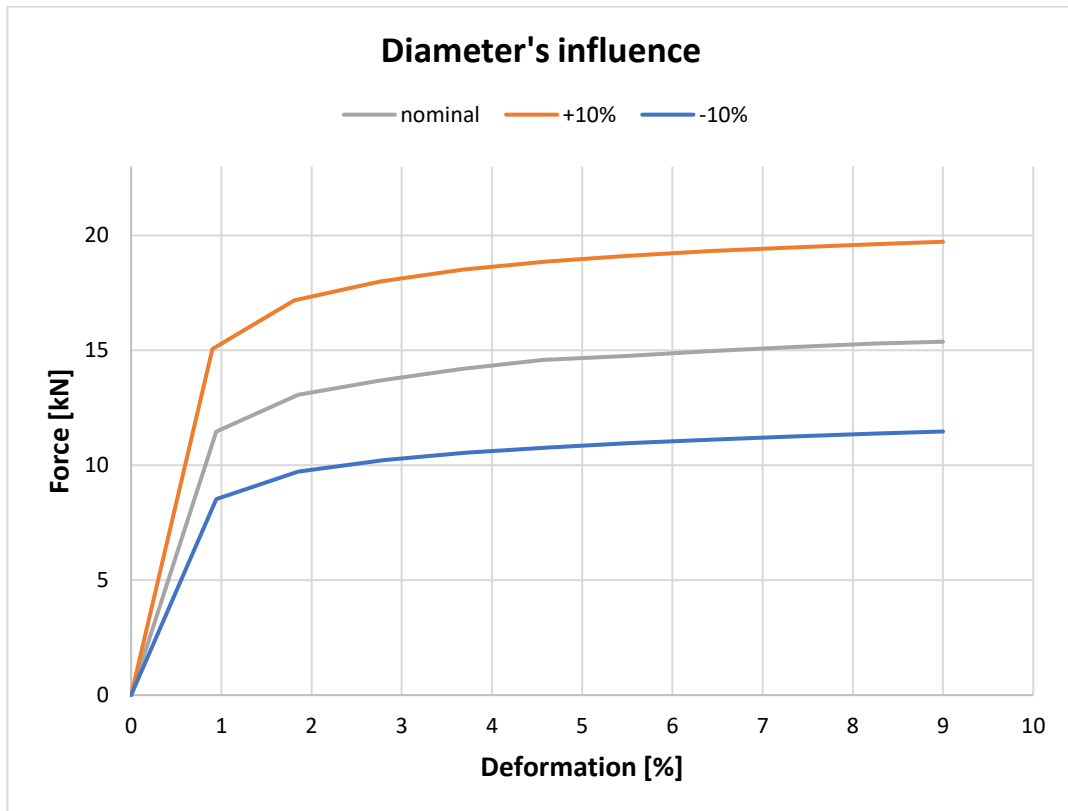


Figure 5.7. Differences between the results of the bi-linear numerical model with the nominal parameters and with the diameter of the struts increased or decreased by 10%

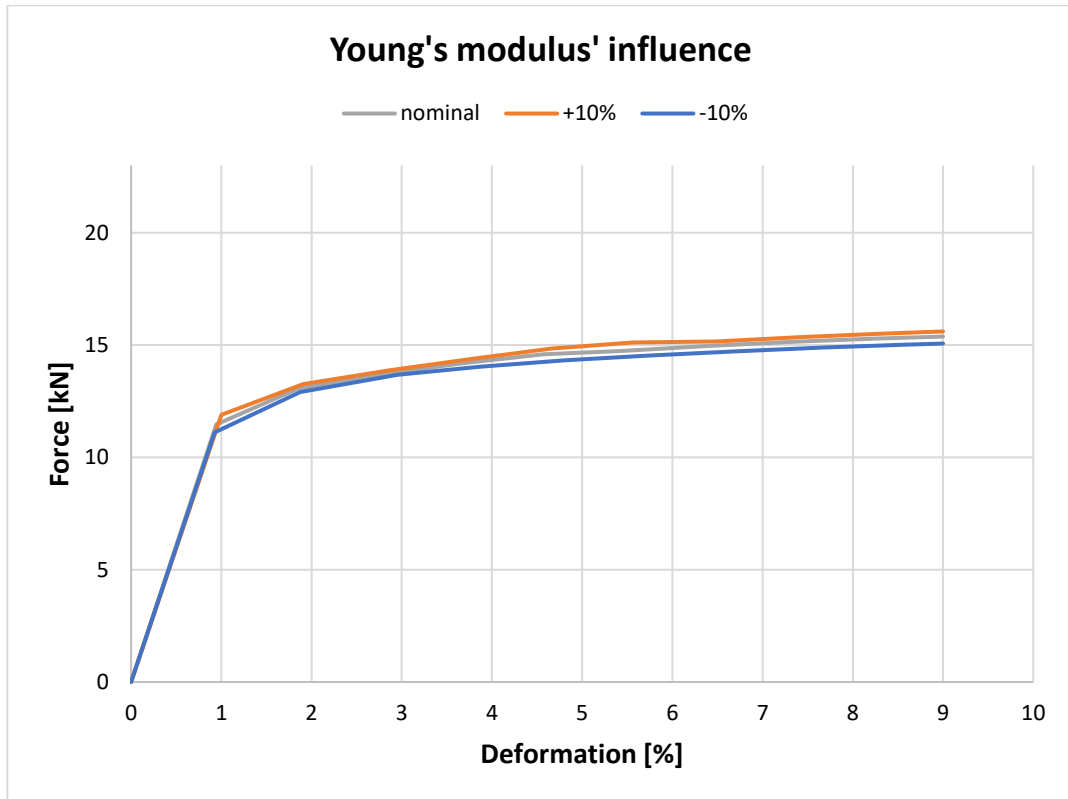


Figure 5.8. Differences between the results of the bi-linear numerical model with the nominal parameters and with the Young's modulus increased or decreased by 10%

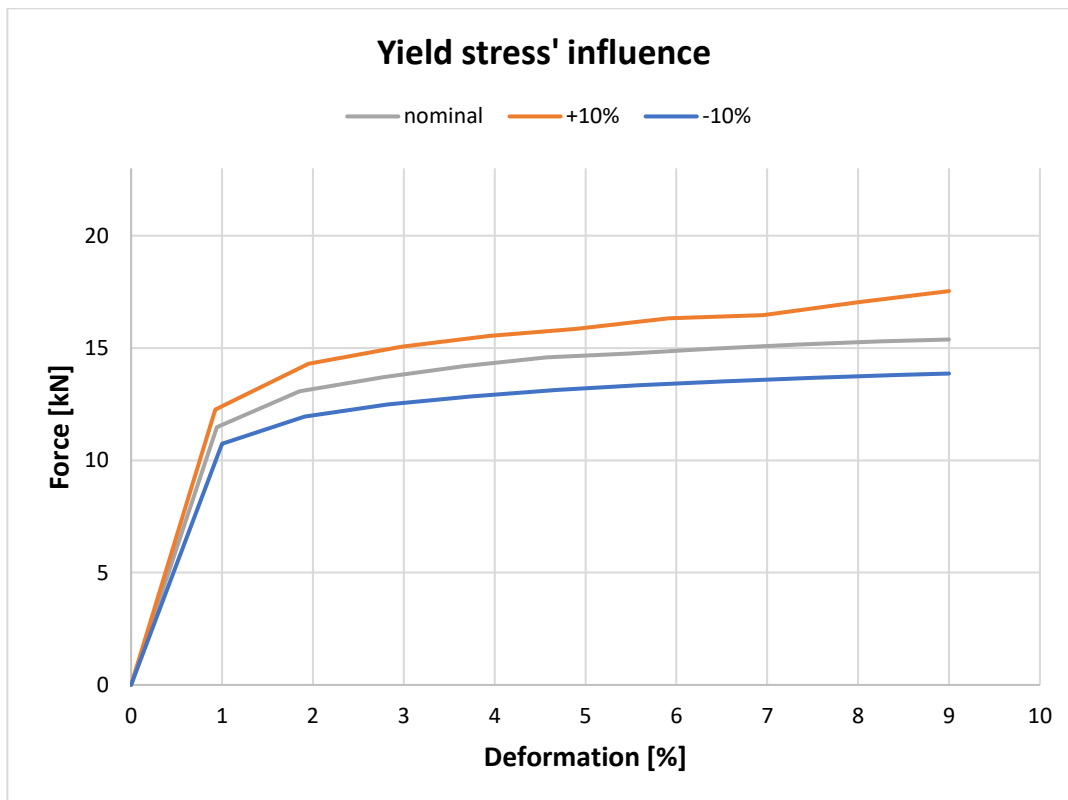


Figure 5.9. Differences between the results of the bi-linear numerical model with the nominal parameters and with the yield stress increased or decreased by 10%

It is evident that the most influencing parameter is the diameter. This is true for the initial part of the graph ("ramp"), but also for the second one ("plateau"). The Young's modulus of the material is not so important. The yield stress has a higher impact, especially on the plateau. It obviously influences also the ramp because some points of the lattice yield already along it.

The great importance of the struts' size could explain the bad results obtained considering the nominal diameters. In fact, as demonstrated by the optical analysis described in paragraph 3.3 [14], the struts are full of size and geometrical imperfections. Even a great surface rugosity has been observed. All these defects are more evident by the nodes of the lattice, that are the most significant points of the entire frame (here the fractures nucleate).

In Fig. 5.10 there are the experimental results in comparison to the numerical response obtained with nominal and lowered parameters only, since they are the most realistic.

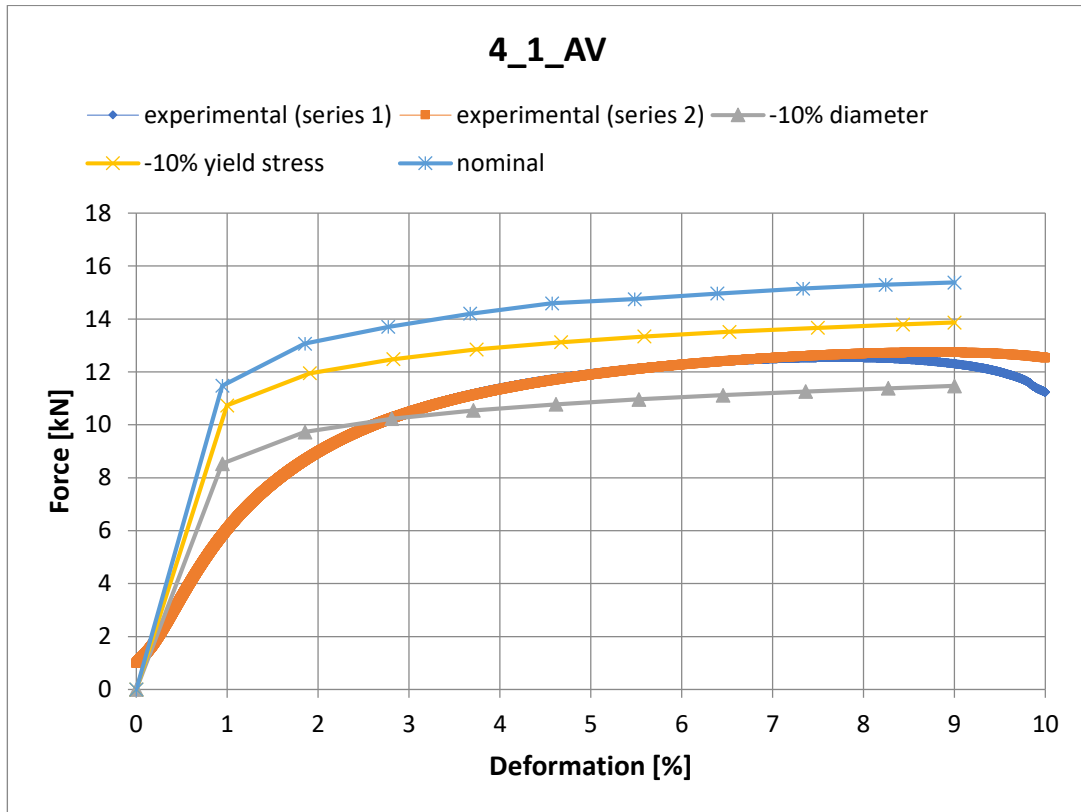


Figure 5.10. Experimental results in comparison to the bi-linear numerical response obtained with nominal and lowered parameters

It can be noticed that the ramp of the numerical models is always too much high and long. Moreover, the plateau is flatter than the experimental ones.

For these reasons, it is important to calibrate the model firstly decreasing the diameter of the beams, especially by the nodes. After this procedure, since a perfectly plastic material has been used, the plateau will be lower, as well as flatter, in respect to the experimental ones. So, it will be necessary to consider always a bilinear material but with a slope different from zero in the plastic part of the stress-strain curve to fit the results also in the plateau.

This second step will change the ramp, because some points of the lattice yield already along it and they feel any variation of the material's characteristics. However, H

has a very low influence on the ramp: in Fig. 5.11, its effects are represented increasing it to 690 MPa (typical value for a heat-treated aluminum alloy).

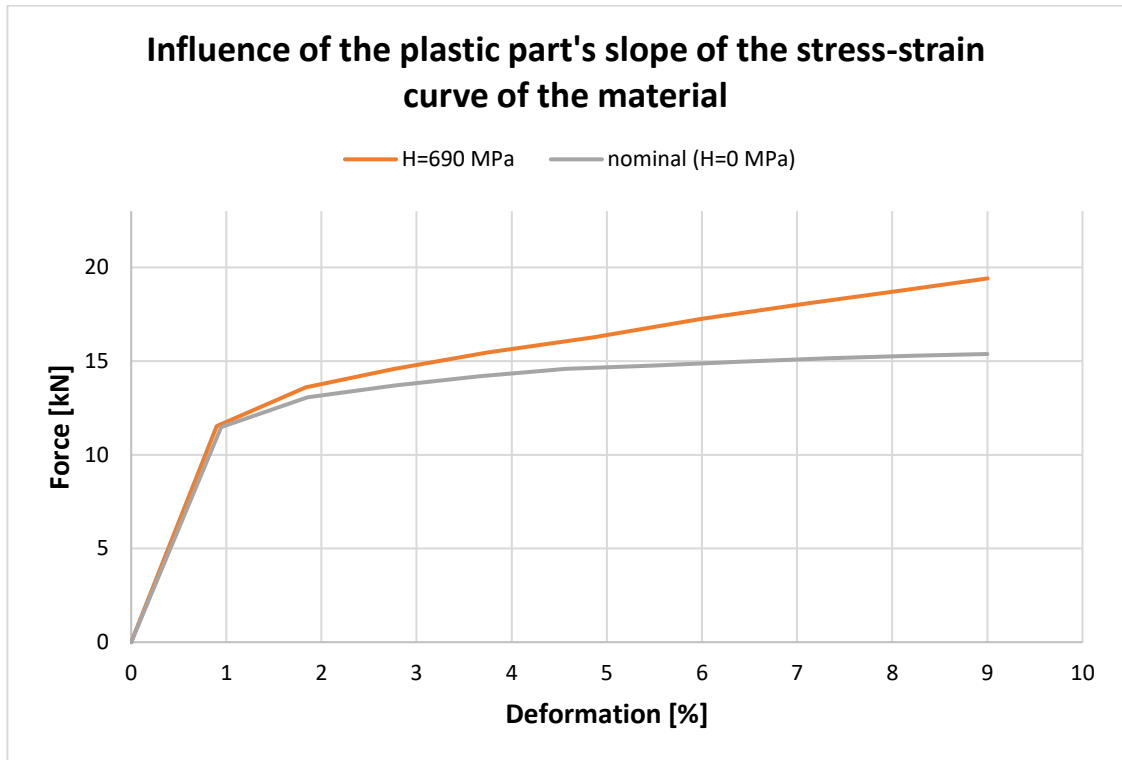


Figure 5.11. Influence of the strength coefficient H

So, since the influence of H is very low along the ramp, especially in comparison to the yield stress' effect, it is possible to consider this fourth parameter in a second phase of the calibration, the one to fit the plateau.

5.2.2 Calibration of the model

To fit experimental and numerical curves, some variations on the input data have been necessary. The same calibration is efficient for all the specimens. The only parameter of the material that has been confirmed is the strength coefficient. The others have been modified respecting the tolerances imposed by the material data sheet [26]:

the elastic modulus has been lowered to its minimum, while the yield stress has been increased to its maximum. So, the following input data have been used:

- $E = 50000 \text{ MPa}$
- $\sigma_y = 245 \text{ MPa}$
- $H = 690 \text{ MPa}$

Even the geometry has been modified to consider the geometrical and size defects of the lattices. The diameters have been decreased by 5% of their nominal value and chamfers have been used to simulate the lack of material by the nodes of the lattice (Fig. 5.12).

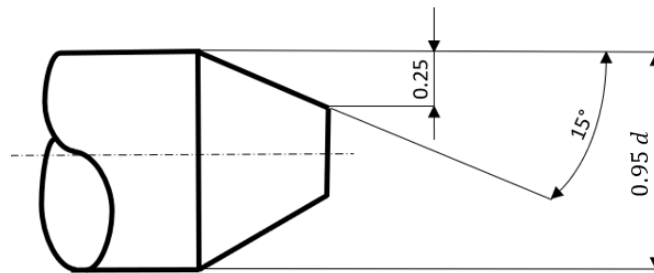


Figure 5.12. Calibrated geometry of the struts

Figs. 5.13 and 5.14 depict the appearance of the lattices modelled after the calibration with boundary conditions and an enlarged view to show the nodes' geometry and the mesh, whose parameters are reported in Table 5.1.

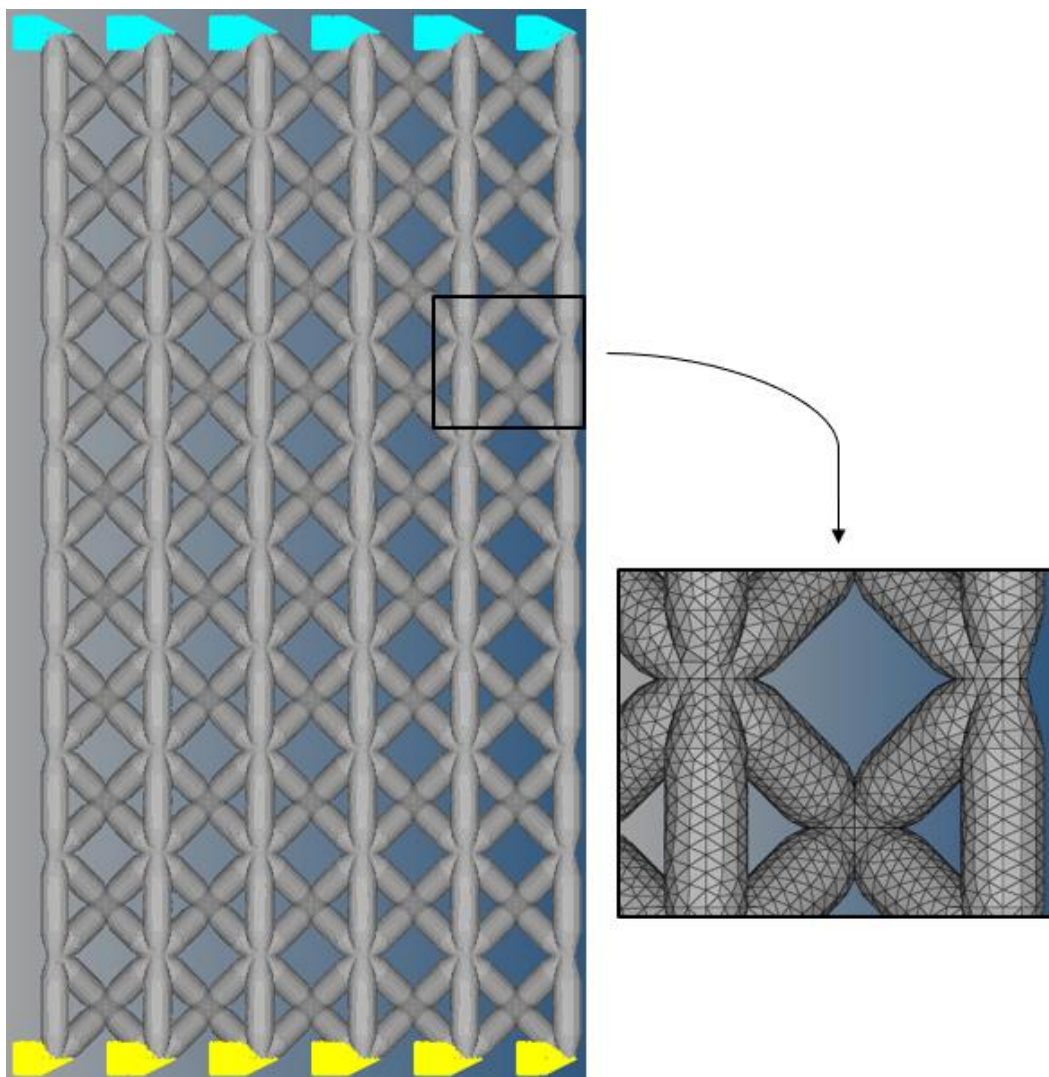


Figure 5.13. Calibrated numerical model of 4_1.2_AV samples with detailed view of the mesh

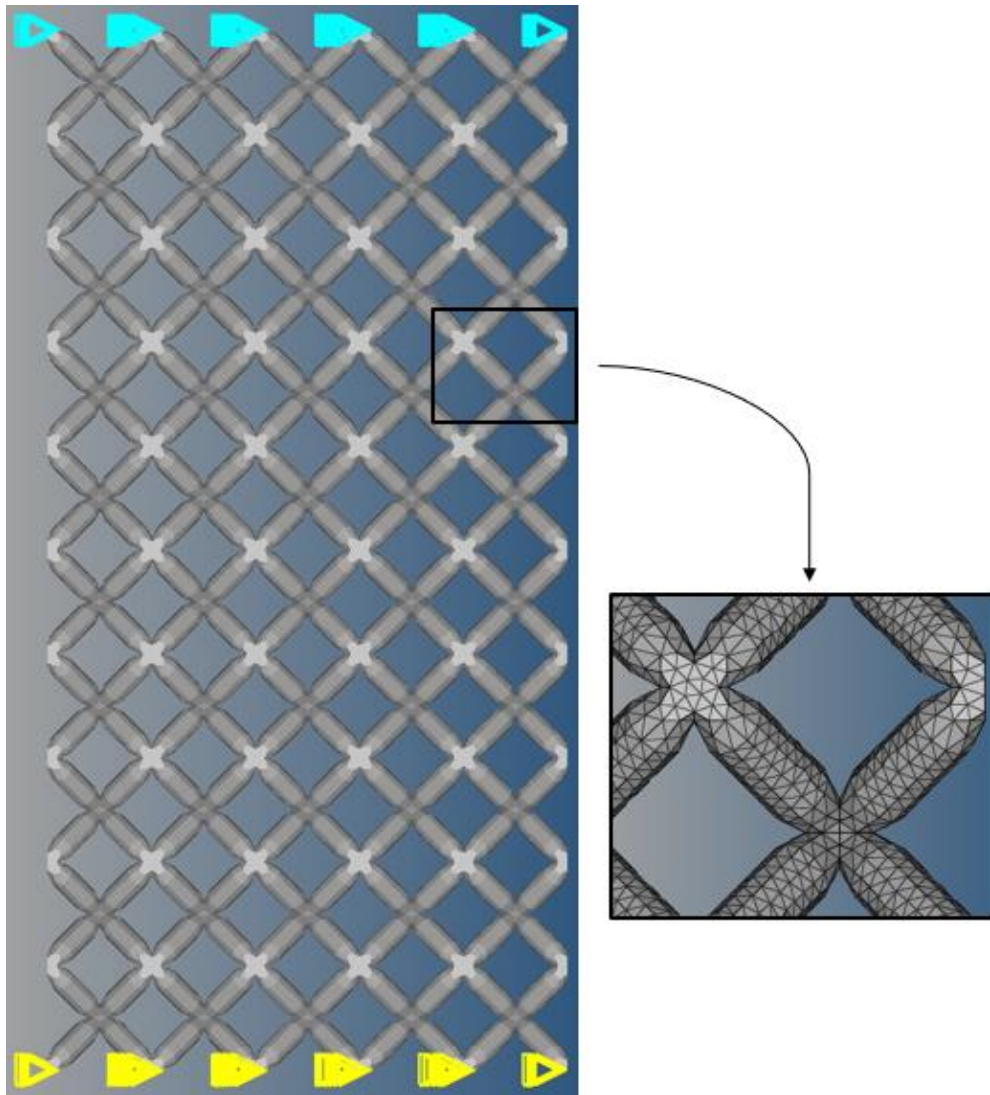


Figure 5.14. Calibrated numerical model of 4_1.2_NA samples with detailed view of the mesh

5.2.3. Bi-linear numerical vs experimental results

The results are satisfactory. Figs. 5.15-5.22 report the comparison between experimental and numerical curves. The numerical results are stopped at the deformation equal to the average between the two deformations corresponding to the two experimental tension peaks.

The preload (equal to 1 kN) has been turned out to be excessive for 4_1_NA and 5_1_NA samples. In fact, it has absorbed all the elastic deformation (5_1_NA) or great part of it (4_1_NA).

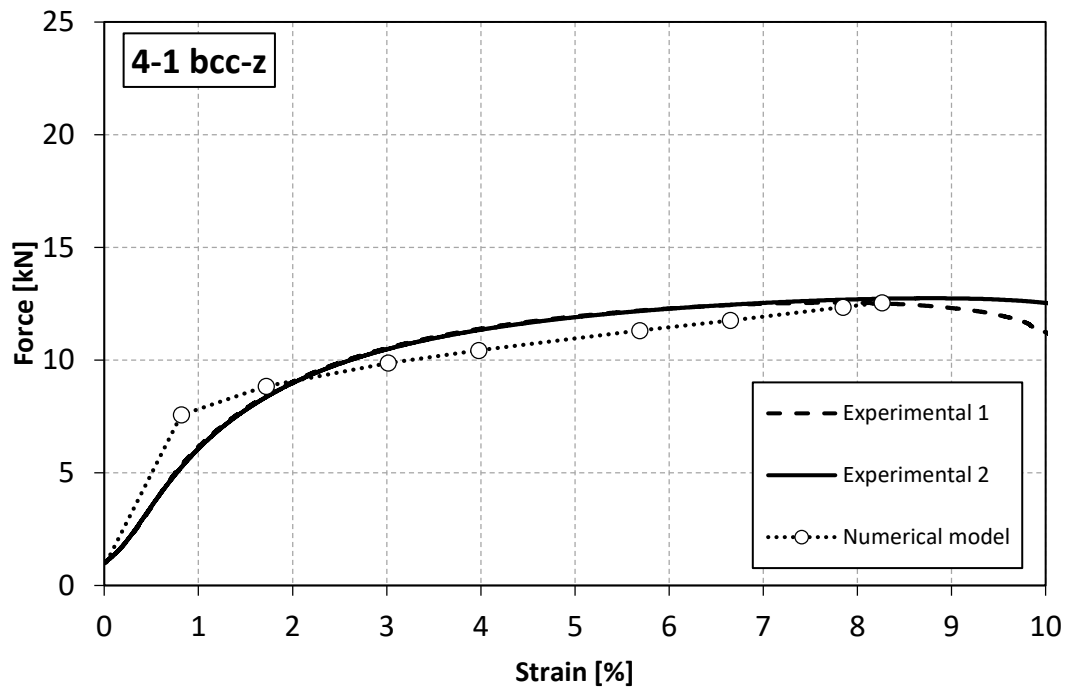


Figure 5.15. Comparison between experimental and calibrated bi-linear numerical model's results of 4_1_AV samples

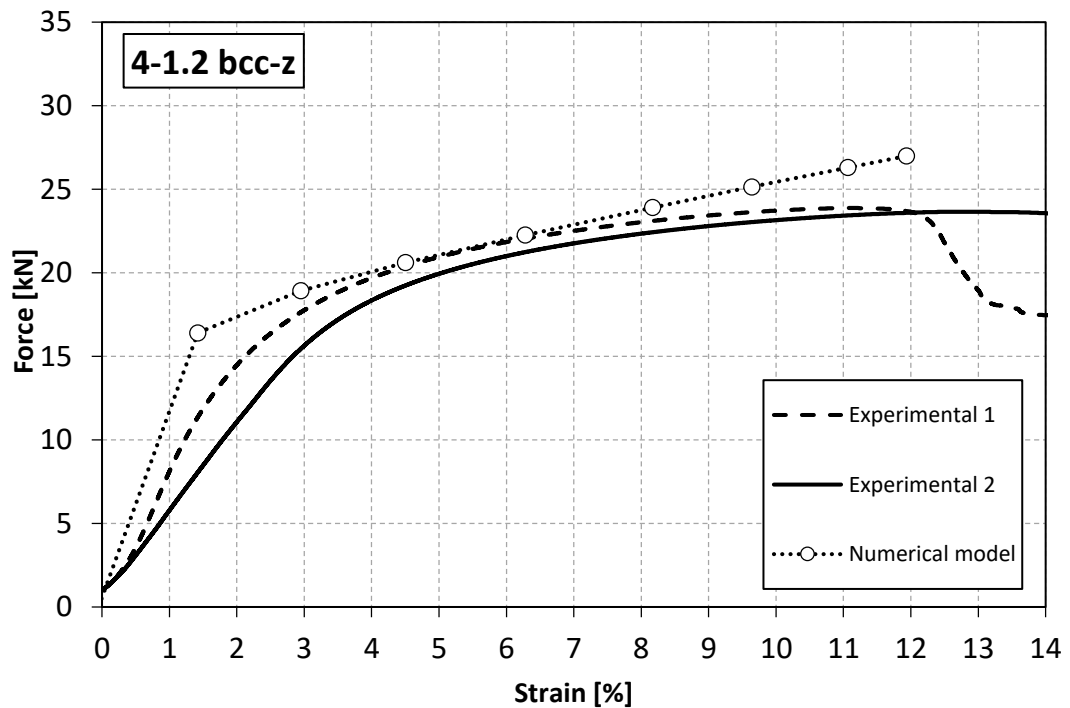


Figure 5.16. Comparison between experimental and calibrated bi-linear numerical model's results of 4_1.2_AV samples

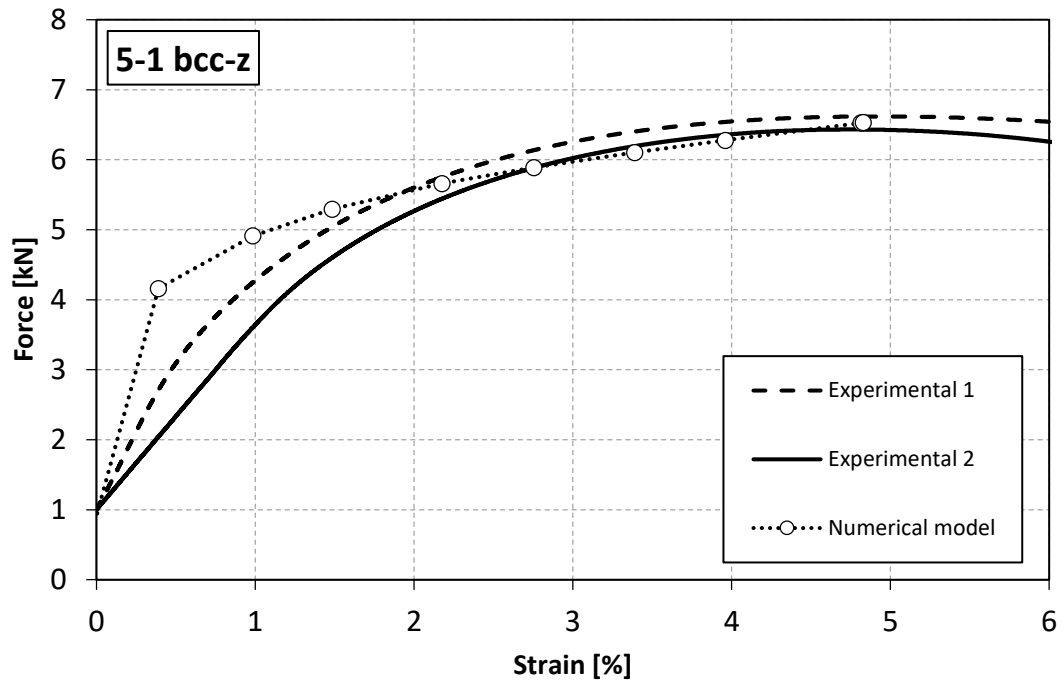


Figure 5.17. Comparison between experimental and calibrated bi-linear numerical model's results of 5_1_AV samples

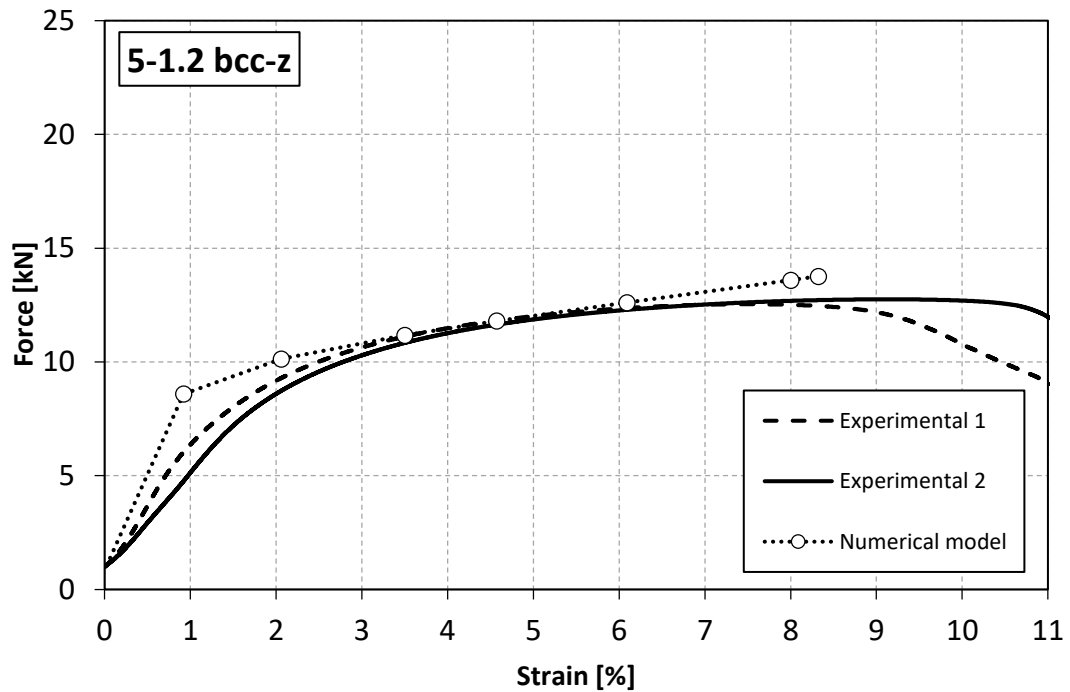


Figure 5.18. Comparison between experimental and calibrated bi-linear numerical model's results of 5_1.2_AV samples

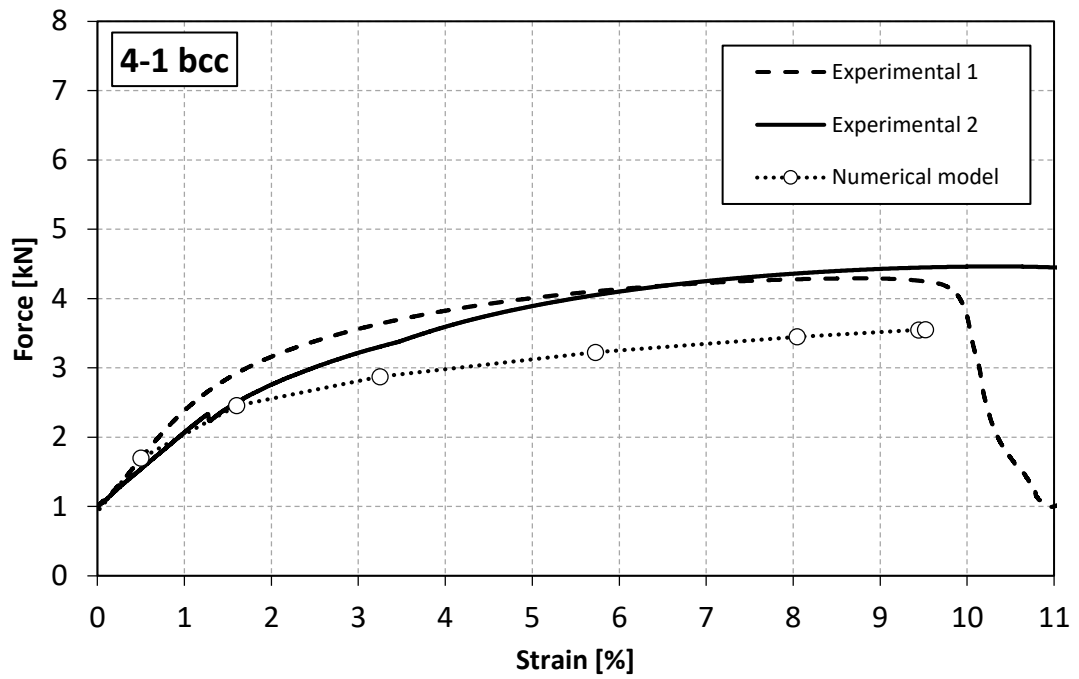


Figure 5.19. Comparison between experimental and calibrated bi-linear numerical model's results of 4_1_NA samples

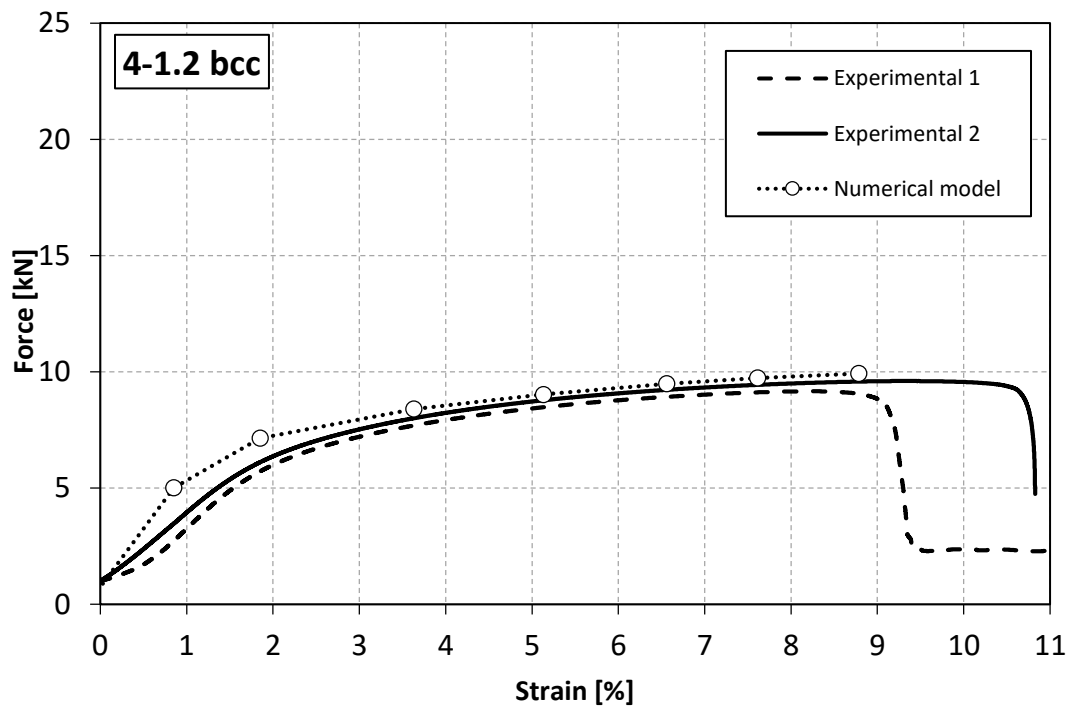


Figure 5.20. Comparison between experimental and calibrated bi-linear numerical model's results of 4_1.2_NA samples

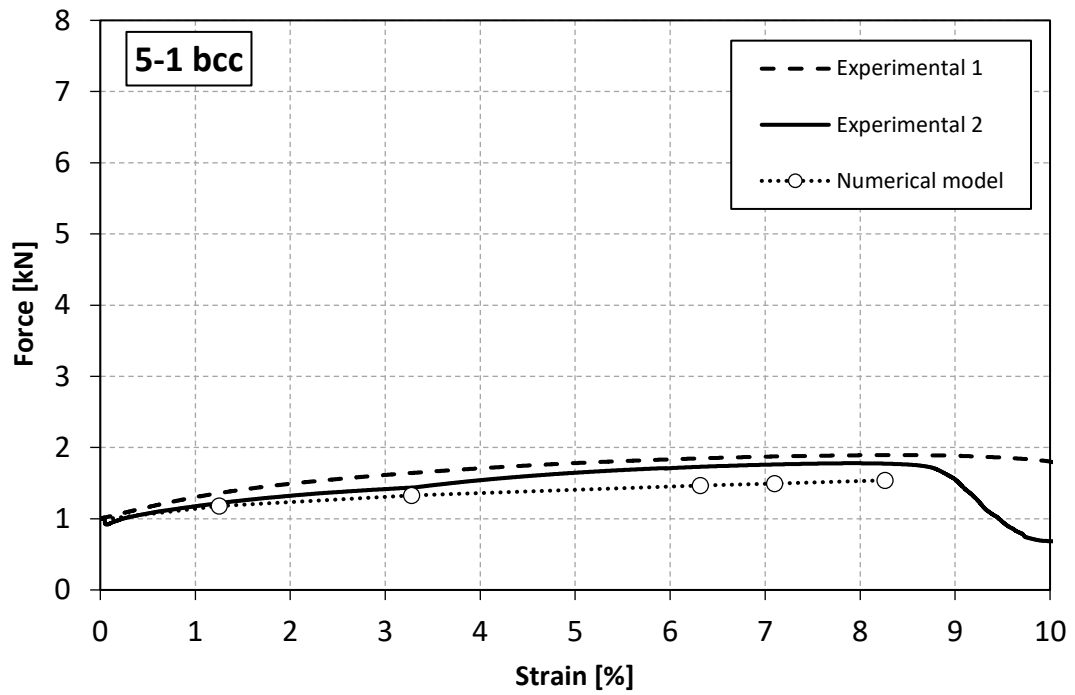


Figure 5.21. Comparison between experimental and calibrated bi-linear numerical model's results of 5_1_NA samples

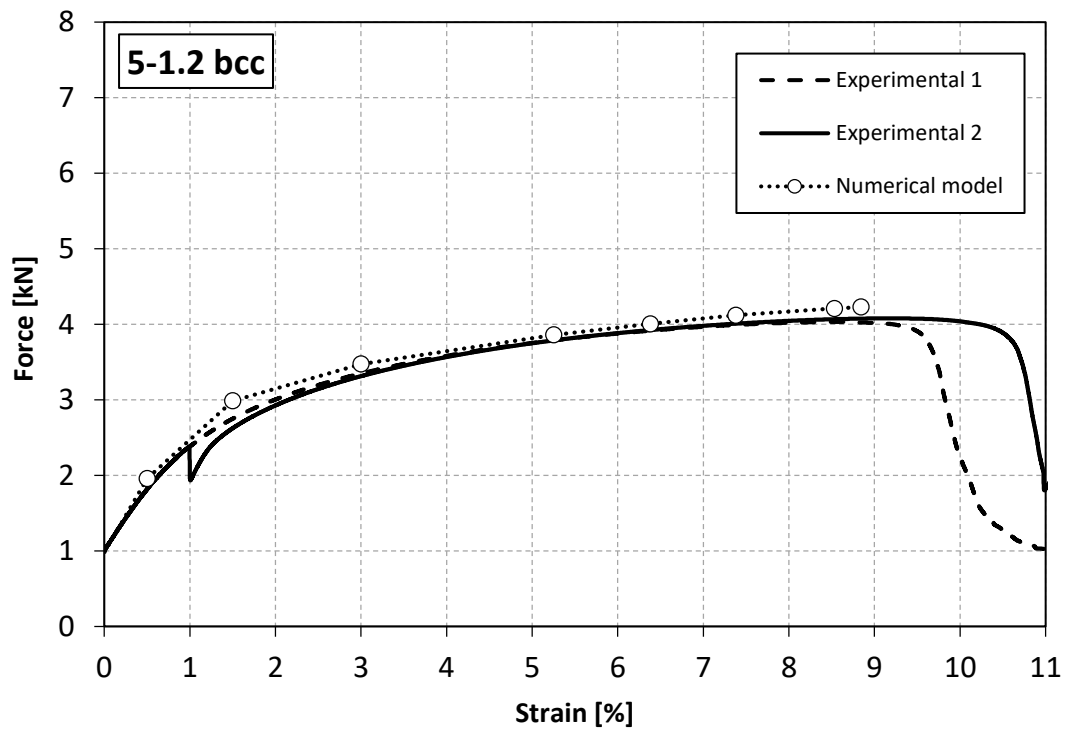


Figure 5.22. Comparison between experimental and calibrated bi-linear numerical model's results of 5_1.2_NA samples

Figs. 5.23-5.30 show the displacements and tension contour plots at the end of the numerical simulations.

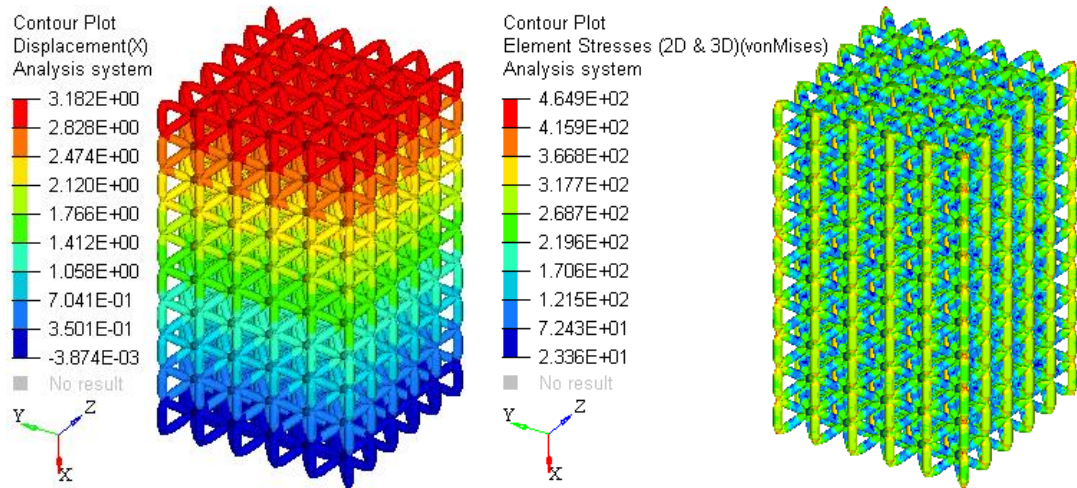


Figure 5.23. Displacements [mm] and Von Mises tension [MPa] obtained with the calibrated bi-linear numerical model for 4_1_AV samples

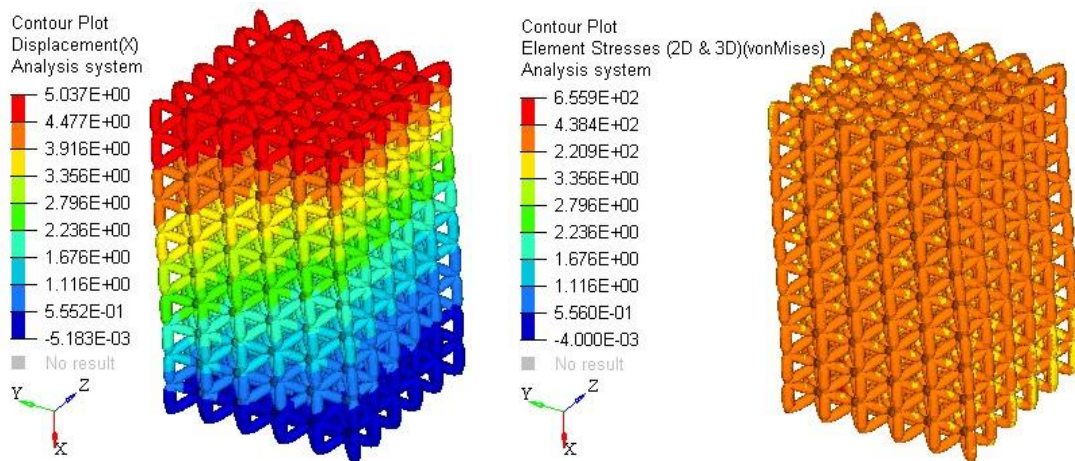


Figure 5.24. Displacements [mm] and Von Mises tension [MPa] obtained with the calibrated bi-linear numerical model for 4_1.2_AV samples

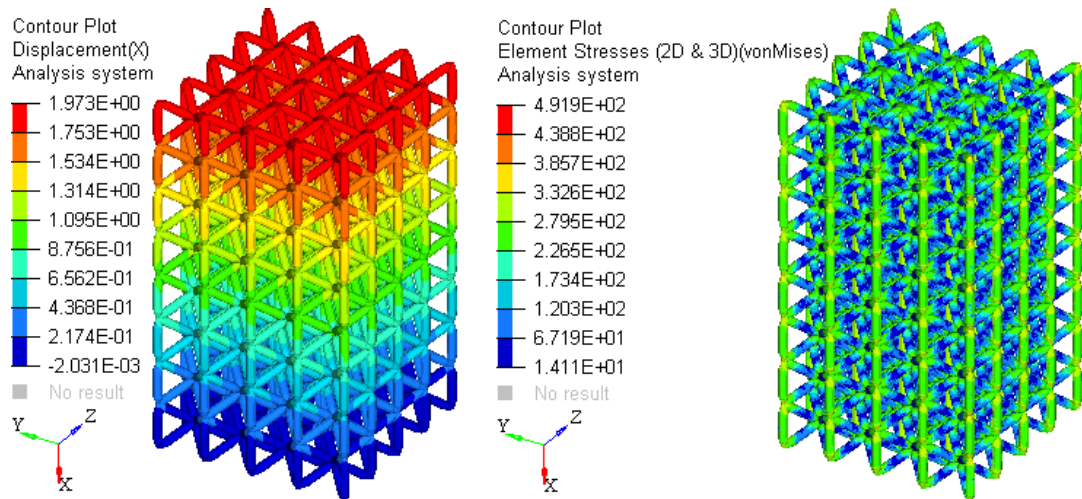


Figure 5.25. Displacements [mm] and Von Mises tension [MPa] obtained with the calibrated bi-linear numerical model for 5_1_AV samples

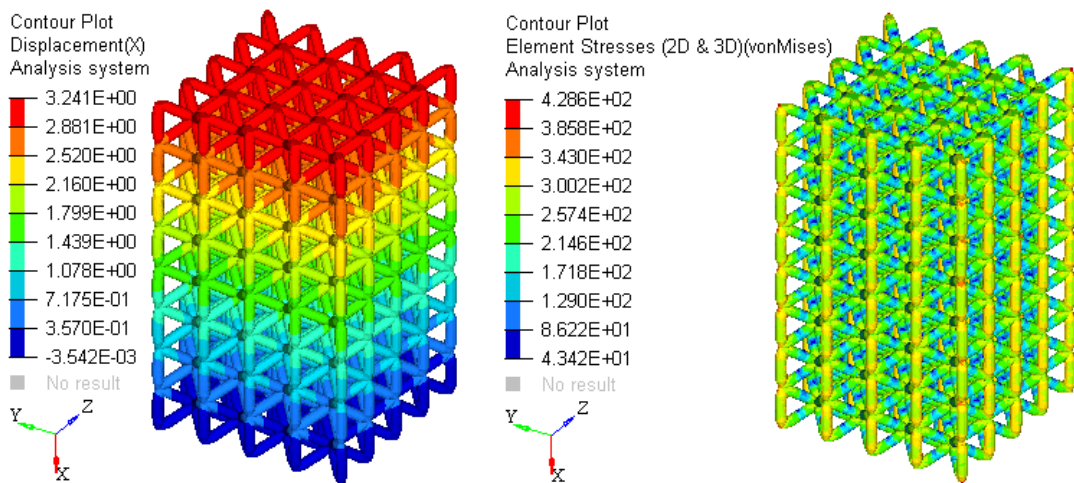


Figure 5.26. Displacements [mm] and Von Mises tension [MPa] obtained with the calibrated bi-linear numerical model for 5_1.2_AV samples

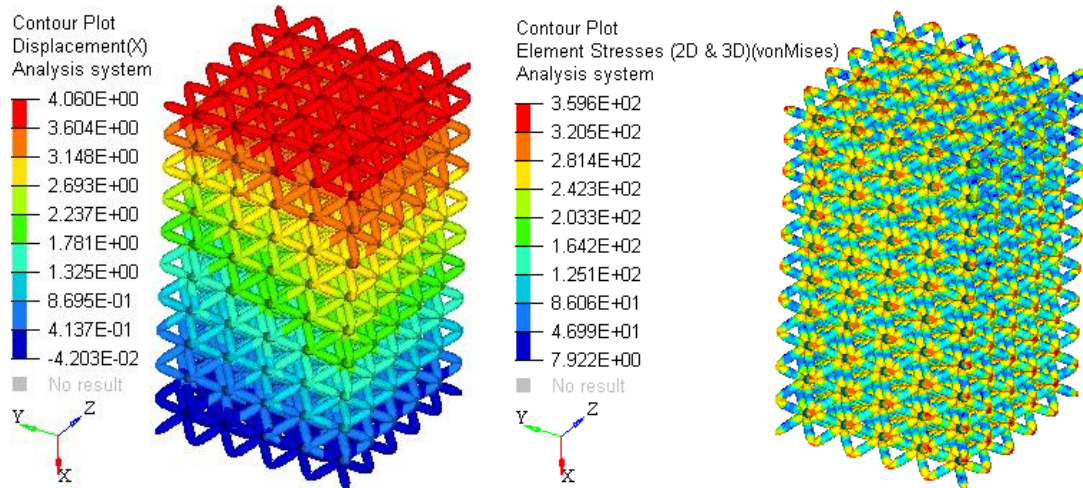


Figure 5.27. Displacements [mm] and Von Mises tension [MPa] obtained with the calibrated bi-linear numerical model for 4_1_NA samples

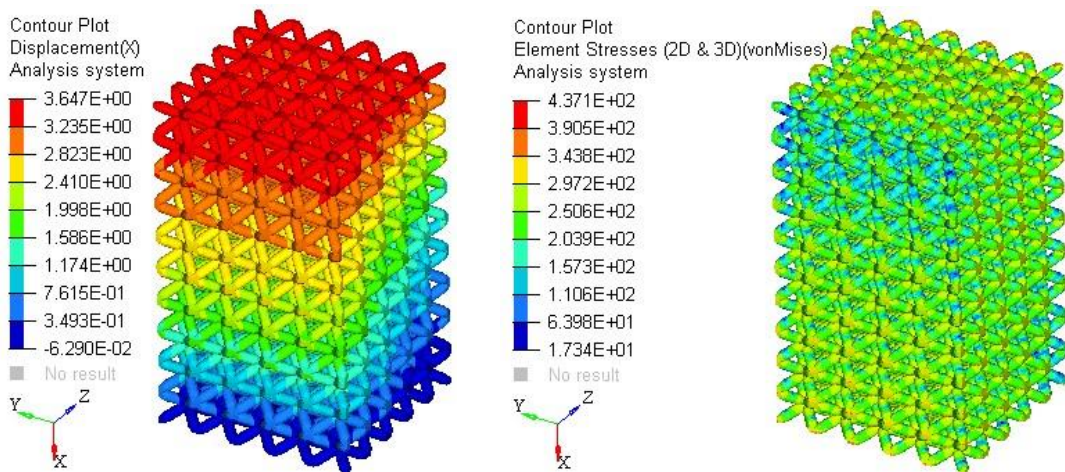


Figure 5.28. Displacements [mm] and Von Mises tension [MPa] obtained with the calibrated bi-linear numerical model for 4_1.2_NA samples

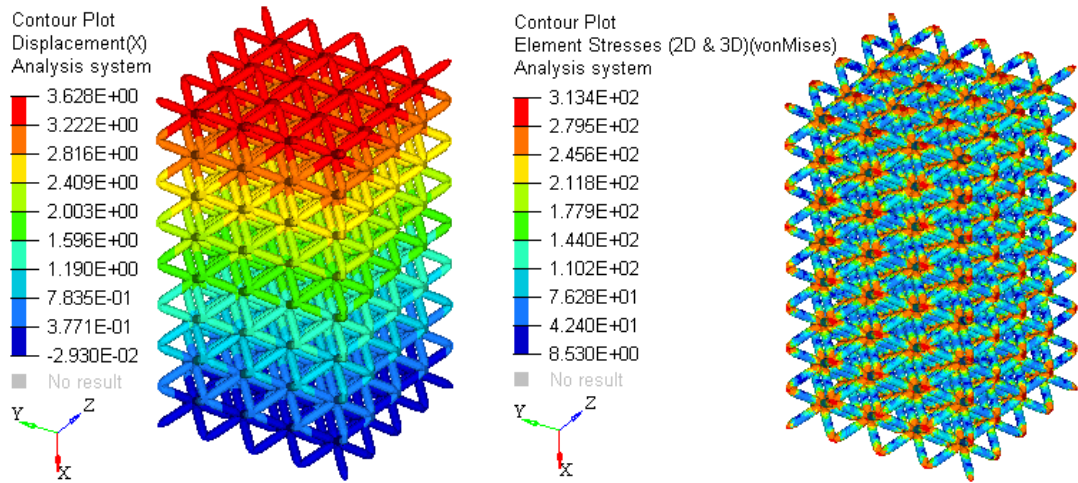


Figure 5.29. Displacements [mm] and Von Mises tension [MPa] obtained with the calibrated bi-linear numerical model for 5_1_NA samples

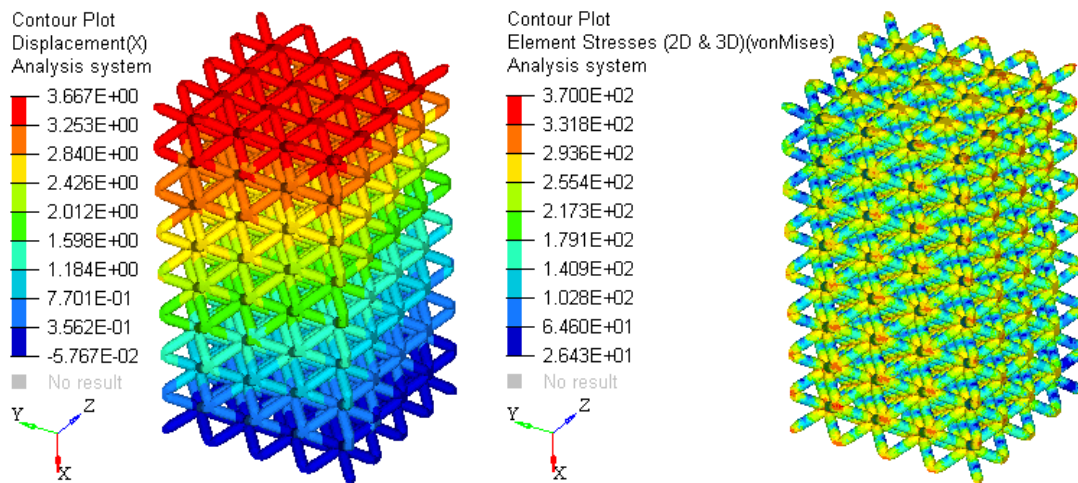


Figure 5.30. Displacements [mm] and Von Mises tension [MPa] obtained with the calibrated bi-linear numerical model for 5_1.2_NA samples

Chapter 6

Energetic analysis

The deformation energy in the load direction is proportional to the area subtended by the stress-strain plot. This last one is piecewise linear for numerical plots as well as for experimental ones. In fact, the numerical model is implicit non-linear (each sub-step of the simulation gives a partial result), while the raw data coming from the experiments, even if very numerous, are discrete too. So, the computation of the deformation energy in the load direction is very easy. To obtain the "total" deformation energy \mathcal{E} , it is sufficient to multiply it by the volume V of the sample, as shown in Eq. (6.1):

$$\mathcal{E} = \left(\int_0^{\varepsilon_{peak}} \sigma d\varepsilon \right) V \cong \sum_{i=1}^{i_{peak}} (\varepsilon_i - \varepsilon_{i-1}) \frac{(\sigma_i + \sigma_{i-1})}{2} V \quad (6.1)$$

The subscript " i " indicates the i^{th} partial result coming from the numerical/experimental test; while "peak" refers to the first tension peak. Since there are two experimental tests for each sample, there are two different deformations corresponding to the tension peaks: for the numerical case ε_{peak} assumes a value equal to the average of the two experimental ε_{peak} (in Figs. 5.15-5.22 the numerical curve is stopped at this value).

Table 6.1 shows a comparison between the values computed on experimental and numerical plots. Considering the very limited number of experimental tests, the results

are good for all the samples, except for 4_1_NA and 5_1_NA. The explanation to this problem is linked to the preload. In fact, 1 kN is too much high for these two samples: it absorbs all the elastic deformation (5_1_NA) or great part of it (4_1_NA).

Table 6.1. Comparison between experimental and numerical deformation energies

Specimen	\mathcal{E} [mJ]		Deviation between experimental series 1 and 2 [%]	\mathcal{E} [mJ]		Relative error between experimental average and numerical [%]
	Experimental (series 1)	Experimental (series 2)		Experimental (average)	Numerical	
4_1_AV	31130	36188	8	33659	32823	-2
4_1.2_AV	83802	94734	6	89268	99052	+11
5_1_AV	10544	9427	6	9986	10513	+5
5_1.2_AV	29999	37600	11	33800	36276	+7
4_1_NA	12507	14687	8	13597	11120	-18
4_1.2_NA	23234	28484	10	25859	28170	+9
5_1_NA	5625	4782	8	5204	4425	-15
5_1.2_NA	11407	12496	5	11952	12366	+3

The outcomes are plotted in Fig. 6.1.

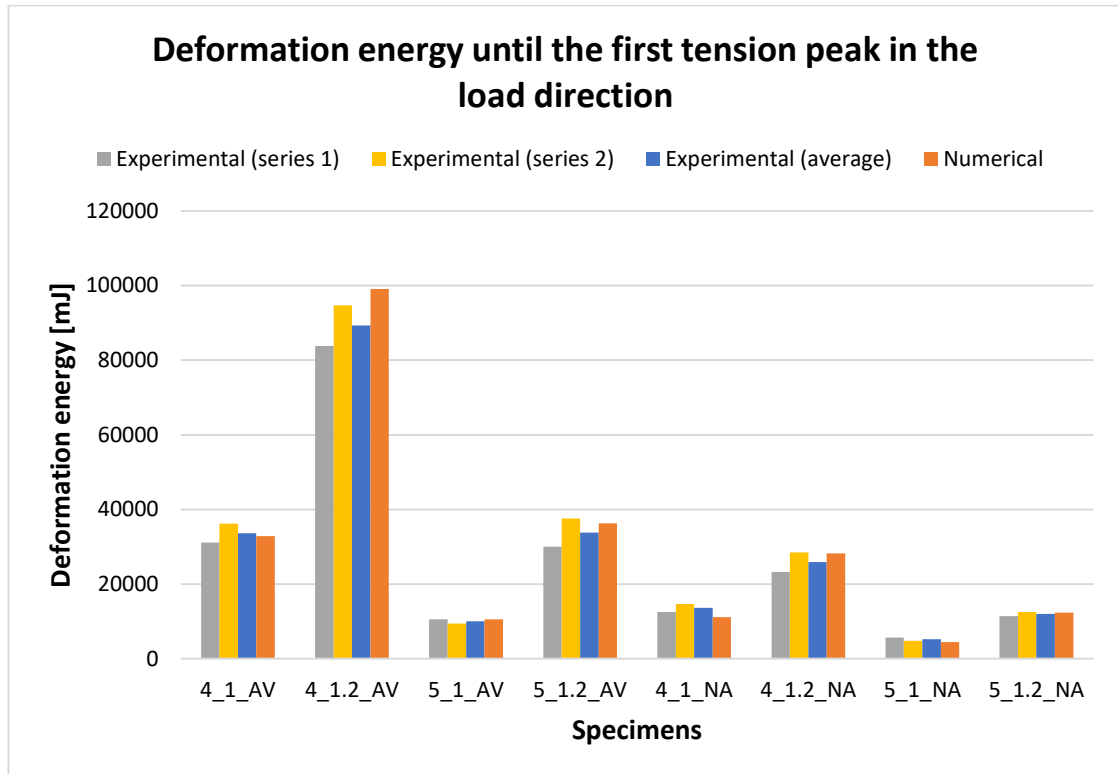


Figure 6.1. Comparison between experimental and numerical deformation energy until the first tension peak in the load direction

Obviously, the deformation energy, as well as the stiffness, is proportional to the relative density of the specimen [30, 31]. In fact, generally, bcc-z topology ensures higher values of \mathcal{E} and the higher is the number of cells, the higher is \mathcal{E} . Especially the 4_1.2_AV sample dissipates a great amount of energy.

Even if these results are obtained from static tests, some useful considerations can be useful for a possible future impact analysis. In fact, 4_1.2_AV sample, could be considered the best shock absorber among the analyzed specimens, even because, as described in paragraph 4.1, bcc-z lattices have not a catastrophic failure.

Conclusions

This work has analyzed analytically, experimentally and numerically the structural behavior of some lattice specimens under a compression load.

After a description of the problem relative to ice formation on aircrafts and wind turbines, a panoramic view of the today's anti-icing and de-icing systems has been proposed. The new patent by Politecnico di Torino, based on a sandwich panel with a lattice core, has been presented.

A general analytical model has been created to compute the stiffness of lattices composed by bcc-z, bcc, bcp-z or bcp cells. It could be useful for any applications which respect its applicability's limits.

The design and the production process of the specimens for the analysis of the lattice core of the new system patented by Politecnico di Torino, as well as the compression tests, have been described. These experiments have been useful to characterize the samples in terms of stiffness, apparent yield stress, apparent maximum stress and absorbed deformation energy. The results obtained have been collected in tables and graphs. Obviously, a sample with a higher relative density, has higher mechanical properties. Even the fracture modalities have been analyzed. These are catastrophic only for bcc samples.

A 3D non-linear quasi-static numerical model has been elaborated through a commercial FEM software (Optistruct by Altair) to foresee the experimental outcomes.

Very good results have been reached after a uniform calibration over all the specimens.

This model should be efficient to simulate the whole component too.

An energetic analysis has revealed that bcc-z topology is the most adapt for the absorption of energy. Moreover, the results, even if obtained by static tests, give useful information for a possible future impact analysis. The 4_1.2_AV sample could be considered the best shock absorber among the analyzed specimens. These reflections are usable also for other applications which involve lattice structures, even built with other materials. It could be the case of modern bumpers.

Besides the impact analysis, also other studies could be interesting, such as the ones relative to fatigue and thermal behavior. Currently other theses deal with this last topic. Moreover, new topologies and materials could be analyzed. Even new production technologies and special treatments could be explored. Hot isostatic pressure (hipping), for example, could enhance the mechanical properties of the lattices by limiting the micro-voids inside the struts and decreasing their surface rugosity.

All these passages are necessary to design the entire system in its optimal version, before creating and testing it.

References

- [1] F. Vitti, P. Maggiore, C. G. Ferro, S. Varetti, "An aircraft equipped with a structurally integrated de-icing system", Italy patent IT 102016000098196, 2016.
- [2] A. Tagliaferri, "Progettazione di solidi cellulari per strutture biomimetiche", Bachelor's thesis in mechanical engineering, 2016.
- [3] Federal Aviation Administration, Aviation Maintenance Technician Handbook Air-frame. Volume 2, 2012.
- [4] O. Parent, A. Ilinca, "Anti-icing and de-icing techniques for wind turbines: Critical review", Cold Regions Science and Technology, n. 65, pp. 88-96, 2011.
- [5] N. Dalili, A. Edrisy, R. Carriveau, "A review of surface engineering issues critical to wind turbine performance", Renewable and Sustainable Energy Reviews, n. 13, pp. 428-438, 2009.
- [6] Y. Wang, Y. Xu, Q. Huang, "Progress on ultrasonic guided waves de-icing techniques in improving aviation energy efficiency", Renewable and Sustainable Energy Reviews, n. 79, pp. 638-645, 2017.
- [7] H. Habibi, L. Cheng, H. Zheng, V. Kappatos, C. Selcuk, T. Gan, "A dual de-icing system for wind turbine blades combining high-power ultrasonic guided waves and low-frequency forced vibrations", Renewable Energy, n. 83, pp. 859-870, 2015.

- [8] Z. Wang, "Recent progress on ultrasonic de-icing technique used for wind power generation, high-voltage transmission line and aircraft", *Energy and Buildings*, n. 140, pp. 42-49, 2017.
- [9] J. Zeng, B. Song, "Research on experiment and numerical simulation of ultrasonic de-icing for wind turbine blades", *Renewable Energy*, n. 113, pp. 706-712, 2017.
- [10] Z. Goray, "An overview of the deicing and antiicing technologies with prospects for the future", XXIV International congress of the aeronautical sciences (ICAS), Yokohama, Japan, 2004.
- [11] S. Venna, Y. Lin, G. Botura, "Piezoelectric transducer actuated leading edge deicing with simultaneous shear and impulse forces", *Journal of Aircraft*, n. 44, pp. 509-515, 2007
- [12] C. G. Ferro, S. Varetti, F. Vitti, P. Maggiore, M. Lombardi, S. Biamino, D. Manfredi, F. Calignano, "A robust multifunctional sandwich panel design with trabecular structures by the use of additive manufacturing technology for a new de-icing system", *Technologies*, n. 5, 2017.
- [13] M. Bici, S. Brischetto, F. Campana, C. G. Ferro, C. Secli, S. Varetti, P. Maggiore, A. Mazza, "Development of a multifunctional panel for aerospace use through SLM additive manufacturing", XI CIRP Conference on Intelligent Computation in Manufacturing Engineering (CIRP ICME), Gulf of Naples, Italy, 2017.
- [14] C. G. Ferro, S. Varetti, P. Maggiore, M. Lombardi, S. Biamino, D. Manfredi, F. Calignano, "Design and characterization of trabecular structures for an anti-icing sandwich panel produced by additive manufacturing", *Journal of Sandwich Structures and Materials*, pp. 1-21, 2018.

- [15] S. Varetti, "Design and characterization of trabecular structures of aluminium alloy produced by DMLM (Direct Metal Laser Melting) for aeronautical sandwich panels.", Master of science thesis in materials engineering, 2016.
- [16] F. Vitti, "Experimental validation and structural analysis of a metal micro-lattice component", Master of science thesis in aerospace engineering, 2016.
- [17] Available on-line: <https://it.wikipedia.org>
- [18] Available on-line: <https://www.planeandpilotmag.com>
- [19] Available on-line: <https://aviaturkey.com>
- [20] Available on-line: <https://www.newscientist.com>
- [21] Available on-line: <http://www.aerospacemx.com>
- [22] Available on-line: <https://www.windpowerengineering.com>
- [23] Available on-line: <https://www.kriwan.com>
- [24] Available on-line: <http://helitecnics.com>
- [25] H. Chen, Q. Zheng, L. Zhao, Y. Zhang, H. Fan, "Mechanical property of lattice truss material in sandwich panel including strut flexural deformation", *Composite Structures*, n. 94, pp. 3448-3456, 2012.
- [26] Available on-line: <https://www.eos.info>
- [27] Available on-line: <http://cmmrl.berkeley.edu>
- [28] Available on-line: <http://www.leica-microsystems.com>
- [29] Available on-line: <https://www.zwick.com>
- [30] L. J. Gibson, M. F. Ashby, "Cellular Solids: Structure and Properties", Cambridge University Press, New York, 1997.
- [31] M.F. Ashby, A.G. Evans, N.A. Fleck, L.J. Gibson, J.W. Hutchinson, H.N.G. Wadley, "Metal Foams: A Design Guide", Butterworth-Heinemann, 2000.

- [32] S. L. Sing, F. E. Wiria, W. Y. Yeong, "Selective laser melting of lattice structures: a statistical approach to manufacturability and mechanical behaviour", *Robotics and computer-integrated manufacturing*, n. 49, pp. 170-180, 2018.
- [33] M. Leary, M. Mazur, J. Elambasseril, M. McMillan, T. Chirent, Y. Sun, M. Qian, M. Easton, M. Brandt, "Selective Laser Melting (SLM) of AlSi12Mg lattice structures", *Materials and Design*, n. 98, pp. 344-357, 2016.
- [34] G. De Pasquale, F. Luceri, M. Riccio, "Experimental evaluation of selective laser melting process for optimized lattice structures", *Proceedings of the Institution of Mechanical Engineers, Part E: Journal of Process Mechanical Engineering*, 2018.
- [35] G. De Pasquale, F. Luceri, M. Riccio, "Experimental validation of Ti6Al4V bio-inspired cellular structures from additive manufacturing processes", In: 1st International Conference on Materials, Mimicking, Manufacturing from and for Bio Application (BioM&M), Milano, Italy, 2018.
- [36] G. De Pasquale, M. Montemurro, A. Catapano, "Cellular structures from additive processes: design, homogenization and experimental validation", *Procedia Struct Integrity*, n. 8, pp. 75-82, 2018.
- [37] M. Montemurro, G. De Pasquale, G. Bertolino, "Multi-scale optimization of lattice structures for biomechanical components", In: ICMAMS, Torino, Italy, 2018.
- [38] G. De Pasquale, F. Luceri, M. Romeo, "SLM-EBM processes optimization for metal lattice structures fabrication", In: ICMAMS, Torino, Italy, 2018.